

InP microdisks for optical signal processing and data transmission

Citation for published version (APA):

Hofrichter, J. (2013). *InP microdisks for optical signal processing and data transmission*. [Phd Thesis 1 (Research TU/e / Graduation TU/e), Electrical Engineering]. Technische Universiteit Eindhoven. <https://doi.org/10.6100/IR750668>

DOI:

[10.6100/IR750668](https://doi.org/10.6100/IR750668)

Document status and date:

Published: 01/01/2013

Document Version:

Publisher's PDF, also known as Version of Record (includes final page, issue and volume numbers)

Please check the document version of this publication:

- A submitted manuscript is the version of the article upon submission and before peer-review. There can be important differences between the submitted version and the official published version of record. People interested in the research are advised to contact the author for the final version of the publication, or visit the DOI to the publisher's website.
- The final author version and the galley proof are versions of the publication after peer review.
- The final published version features the final layout of the paper including the volume, issue and page numbers.

[Link to publication](#)

General rights

Copyright and moral rights for the publications made accessible in the public portal are retained by the authors and/or other copyright owners and it is a condition of accessing publications that users recognise and abide by the legal requirements associated with these rights.

- Users may download and print one copy of any publication from the public portal for the purpose of private study or research.
- You may not further distribute the material or use it for any profit-making activity or commercial gain
- You may freely distribute the URL identifying the publication in the public portal.

If the publication is distributed under the terms of Article 25fa of the Dutch Copyright Act, indicated by the "Taverne" license above, please follow below link for the End User Agreement:

www.tue.nl/taverne

Take down policy

If you believe that this document breaches copyright please contact us at:

openaccess@tue.nl

providing details and we will investigate your claim.

InP Microdisks for Optical Signal Processing and Data Transmission

PROEFSCHRIFT

ter verkrijging van de graad van doctor aan de
Technische Universiteit Eindhoven, op gezag van de
rector magnificus, prof.dr.ir. C.J. van Duijn, voor een
commissie aangewezen door het College voor
Promoties in het openbaar te verdedigen
op donderdag, 14 februari 2013 om 16.00 uur

door

Jens Hofrichter

geboren te Dresden, Duitsland

Dit proefschrift is goedgekeurd door de promotoren:

prof.dr.ir. H.J.S. Dorren,

Co-promotor:

dr.ir. B.J. Offrein,

The research presented in this thesis was carried out at IBM Research - Zurich and at the Electro-optical Communications Group, department of Electrical Engineering of the Eindhoven University of Technology, The Netherlands. This work was financially supported by the European Commission (EC) funded 7th framework programme under the project *HISTORIC*, contract number 223876.

Bibliografische Information der Deutschen Nationalbibliothek
Die Deutsche Nationalbibliothek verzeichnet diese Publikation in der Deutschen Nationalbibliografie; detaillierte bibliografische Daten sind im Internet über <<http://dnb.ddb.de>> abrufbar.

ISBN: 978-3-86387-258-8

Zugl.: Eindhoven, Techn.-Univ., Diss., 2012

Dissertation, Technische Universität Eindhoven

This document is protected by copyright law.

No part of this document may be reproduced in any form by any means without prior written authorization of the publisher.

Alle Rechte vorbehalten | all rights reserved

© Mensch und Buch Verlag 2012

Choriner Str. 85 - 10119 Berlin

verlag@menschundbuch.de – www.menschundbuch.de

”Scientists investigate that which already *is*;
Engineers *create* that which has never been.”
Albert Einstein

This Ph.D. thesis has been approved by a committee with the following members:

Prof. Dr. Meint K. Smit, Eindhoven University of Technology

Prof. Dr. Jürg Leuthold, Karlsruhe Institute of Technology, Germany

Newly affiliated with ETH Zürich, Switzerland as of March 1, 2013

Prof. Dr. Geert Morthier, Ghent University - IMEC, Belgium

A catalogue record is available from the Eindhoven University of Technology Library

InP Microdisks for Optical Signal Processing and Data Transmission

by Jens Hofrichter

Eindhoven: Technische Universiteit Eindhoven, 2012.

Proefschrift. - ISBN 978-3-86387-258-8

NUR 959

Trefwoorden: microdisk lasers / semiconductor lasers / III-V / heterogeneous integration / optical signal processing / wavelength conversion / electroabsorption modulators / silicon photonics / grating couplers / microring lasers

Summary

InP Microdisks for Optical Signal Processing and Data Transmission

The performance increase in telecommunication and computing systems demands an ever increasing input-output (IO) bandwidth and IO density, which can be met by integrated photonics. Using photonic integration, much higher densities of optical components can be achieved allowing for short-range optical communication systems in, e.g., high performance computers. The key functionalities required for these optical communication systems are light generation, light modulation and light detection. In addition to this other functionalities are also desirable, such as wavelength conversion.

This thesis highlights the design and fabrication of indium phosphide (InP) microdisks heterogeneously integrated on silicon-on-insulator substrates. The fabrication of the microdisks in a laboratory clean-room environment is described. These devices can fulfil the above-mentioned functions required in optical communication.

Experiments are then performed on the fabricated devices dealing with these various functionalities that are required for optical communication. The lasing properties of the devices are shown and simulated with a spatially-dependent rate equation model accurately predicting the device behaviour. A detailed speed analysis is given, including a parameter extraction of the devices. The operation of the devices as detectors is highlighted.

Furthermore the PhD thesis provides a deep analysis of the use of InP microdisks as modulators. Besides the forward-biased operation principle using the free-carrier plasma-dispersion effect, also a high-speed reversely biased operation mode is proposed and demonstrated experimentally.

The thesis also describes various approaches on how to improve the performance of the devices, in particular when using them as lasers. Ways how to increase the output power and how to enhance the operation speed

are discussed. Because the device is strongly dependent on the coupling between the resonant InP cavity and the silicon waveguide, an extensive analysis of the coupling and the influence of certain process steps on the device performance are given.

The PhD thesis concludes the work carried out on InP microdisks and gives an outlook about improving the device performance with respect to specific applications and how to further improve the manufacturability of the devices. Finally, for the InP microdisk-based devices an outlook is given about suitable applications, such as on-chip optical links for instance.

Contents

| | |
|--|-------------|
| Summary | i |
| Table of Contents | iii |
| List of Figures | vi |
| List of Tables | xiii |
| List of Acronyms | xv |
| 1 Introduction | 1 |
| 1.1 Optical communication systems | 1 |
| 1.2 Towards photonic integration | 4 |
| 1.3 Unsolved challenges of optical communication systems . . . | 7 |
| 1.4 Contributions of this thesis | 13 |
| 1.5 Outline of this thesis | 15 |
| 2 Photonic Integration Technology | 16 |
| 2.1 Introduction | 16 |
| 2.2 State-of-the-art in photonic integration | 17 |
| 2.3 Design flow used in this thesis | 22 |
| 2.4 SOI waveguide circuitry | 23 |
| 2.5 Laser material | 26 |
| 2.6 InP microdisk fabrication | 27 |
| 2.7 Discussion | 36 |
| 3 InP Microdisk Lasers | 37 |
| 3.1 Laser integration approaches for silicon photonics | 37 |
| 3.2 Modelling InP microdisk lasers | 40 |
| 3.2.1 A 1D radially dependent single-mode microdisk laser model | 40 |
| 3.2.2 A 1D radially dependent multi-mode microdisk laser model | 47 |
| 3.3 Measurements of InP microdisk lasers | 50 |
| 3.3.1 Static characteristics | 51 |
| 3.3.2 Dynamic characteristics | 55 |
| 3.4 Discussion | 60 |

| | | |
|----------|--|------------|
| 4 | InP Microdisk Flip-Flops for All-Optical Logic | 61 |
| 4.1 | Introduction | 61 |
| 4.2 | Switching properties of all-optical InP microdisk flip-flops . | 61 |
| 4.3 | Requirements for all-optical logic and digital systems | 66 |
| 4.4 | Discussion | 71 |
| 5 | InP Microdisk Wavelength Converters | 72 |
| 5.1 | Introduction | 72 |
| 5.2 | Principle of mode switching | 73 |
| 5.3 | Static characteristics | 74 |
| 5.4 | Dynamic characteristics | 75 |
| 5.5 | Improving the speed of wavelength conversion by seeding . | 77 |
| 5.6 | Discussion | 79 |
| 6 | InP Microdisk Detectors | 81 |
| 6.1 | Introduction | 81 |
| 6.2 | Static characteristics | 81 |
| 6.3 | Dynamic characteristics | 83 |
| 6.4 | Discussion | 84 |
| 7 | InP Microdisk Modulators | 87 |
| 7.1 | Introduction | 87 |
| 7.2 | Fabrication | 88 |
| 7.3 | Forward biased InP microdisk modulators | 89 |
| 7.3.1 | Static characteristics | 89 |
| 7.3.2 | Dynamic characteristics | 91 |
| 7.4 | Negatively biased InP microdisk modulators | 92 |
| 7.4.1 | Static characteristics | 92 |
| 7.4.2 | Dynamic characteristics | 93 |
| 7.4.3 | Energy consumption | 98 |
| 7.5 | Discussion | 99 |
| 8 | Improving the Performance of InP Microdisk Lasers | 102 |
| 8.1 | Output power and coupling | 102 |
| 8.2 | Influence of top via on Q-factor | 105 |
| 8.3 | Side-mode suppression ratio | 106 |
| 8.4 | Enhancing the device speed by reduction of electrical parasitics | 107 |
| 8.5 | Epitaxial material | 111 |

| | | |
|----------|----------------------------------|------------|
| 8.6 | Grating couplers | 113 |
| 8.7 | Discussion | 120 |
| 9 | Conclusion and Outlook | 122 |
| 9.1 | Summary and conclusion | 122 |
| 9.2 | Outlook | 125 |
| | References | 146 |
| | List of Publications | 147 |
| | Acknowledgements | 150 |
| | Curriculum Vitae | 152 |

List of Figures

| | | |
|-----|--|----|
| 1.1 | State-of-the-art in tele-communication systems at different points in time: a) 1837 - the telegraph presented by Samuel F.B. Morse and Joseph Henry [1]. b) 2012 - Cisco's carrier routing system CRS-3 [2]. | 2 |
| 1.2 | View from the top of IBM's <i>SuperMUC</i> supercomputer installed at Leibnitz Rechenzentrum (LRZ) in Munich, Germany in 2012. Image is a courtesy of IBM Research - Zurich. The orange wiring on the top are active optical cables linking compute nodes and storage servers [3]. | 4 |
| 1.3 | State-of-the-art in optical interconnect technology. a) Optical printed circuit board using 850 nm multi-mode technology [4]. The insets at the bottom illustrate the data transmission from transmitter 1 (TRX1) to TRX 2 and backwards. b) Optical transceiver technology with direct carrier connections [5]. | 5 |
| 1.4 | Generic scheme of a transmitter and receiver chip using wavelength division multiplexing (WDM). From left to right: The transmitter comprises several lasers, which are then individually modulated. Then, the signals are multiplexed into one single waveguide, which is then coupled to a fibre and transmitted to the receiver chip. Here, the signal is de-multiplexed and detected by an array of photodiodes. The generated photocurrents may then be amplified by a trans-impedance amplifier (TIA). | 6 |
| 2.1 | State of the art in photonic integration. a) Monolithic InP integration - as an example Infinera's packaged 5×114 Gb/s transmitter PIC is shown [6]. b) Silicon photonics - Photograph of IBM's SNIPER chip integrating both optical and electrical functions on the same die [7]. | 19 |
| 2.2 | a) Cross-section of an optical device fabricated with hybrid integration [8]. b) Cross-section of an optical device fabricated using heterogeneous integration [9]. Note that the optical mode is mainly located in the III-V in contrast to the optical mode in a). | 21 |
| 2.3 | Wafer and die layout of the silicon-on-insulator (SOI) multi project wafer (MPW) wafer run. | 23 |

| | | |
|-----|---|----|
| 2.4 | Layout of the SOI die with the bonded InP die on top. The InP microdisks, which are structured later, are shown to indicate their later positioning with respect to the SOI waveguides. | 24 |
| 2.5 | Photoluminescence spectrum recorded on a sample having the epitaxial layer stack as stated in Tab. 2.1. The photoluminescence (PL) spectrum is a courtesy of P. Regreny (INL Lyon). | 25 |
| 2.6 | Approximated spectral gain response according to J. Pikrek - Optoelectronic Devices: Advanced Simulation and Analysis, Chapter 5 [10]. | 25 |
| 2.7 | After bonding the InP die with quantum well on a silicon photonics chip. a) Photograph is a courtesy of S. Keyvaninia (Ghent University). b) Schematic view at this fabrication stage. The full layer stack including the InP substrate, the etch stop layer and the epitaxial layer stack bonded onto the SOI chip is visible. | 27 |
| 2.8 | InP substrate removal and fabrication issues. a) Photograph of the epitaxial layer stack, which remains on the silicon substrate after bonding, and removing the InP substrate and the etch stop layer. The image is a courtesy of S. Keyvaninia (Ghent University). b) Schematic view at this fabrication stage. The remaining epitaxial layer stack including the quantum well is visible. c) Residual particles after substrate removal using chemical-mechanical polishing (CMP). d) Delamination and compromised photoresist wetting properties of a manually bonded sample. Image is a courtesy of O. Raz (TU Eindhoven). | 29 |
| 2.9 | a) Optical microscope image after structuring a microdisk with 5 μm diameter. b) Schematic view at this fabrication stage. c) scanning electron microscope (SEM) image of a microdisk with 10 μm diameter. c) Close-up view on the smooth sidewall of the InP cavity underneath the silicon nitride hardmask. SEM images are a courtesy of T. De Vries (TU Eindhoven). | 30 |

| | | |
|------|---|----|
| 2.10 | The footprint of the InP microdisk device becomes apparent after the island definition. a) Optical microscope image. b) Schematic view at this stage of fabrication. | 31 |
| 2.11 | a) The bottom metal is formed to minimise the resistance of the devices. A clearance around the InP microdisk was maintained to not introduce absorption as shown in this microscope image. b) Schematic view at this stage of fabrication. | 32 |
| 2.12 | a) Optical microscope image after opening the top contact via. b) Schematic view after completing this fabrication step. c) SEM image of the slanted silicon dioxide sidewall, which is required for metallization using evaporation. d) SEM image of an silicon dioxide via with $3.5 \mu\text{m}$ diameter. | 33 |
| 2.13 | a) Optical microscope image after top contact metallization. b) Schematic view after completing this fabrication step. . . | 34 |
| 2.14 | a) Optical microscope image after pad metallization. b) Schematic view after completing this fabrication step. . . . | 35 |
| 3.1 | Cross-section through an InP microdisk laser heterogeneously integrated on a SOI waveguide. Note that on resonance the optical mode is entirely coupled from the silicon waveguide to the InP microdisk. | 39 |
| 3.2 | a) Lasing wavelengths of the fundamental lasing mode in an InP microdisk laser with $7.5 \mu\text{m}$ diameter. b) Cross-section and field distribution simulated by 2D finite-difference time-domain (FDTD). | 41 |
| 3.3 | Different radial optical modes in a microdisk laser. | 43 |
| 3.4 | Temporal response of the electron density in a microdisk laser when applying a current step of 2.5 mA at $t=0$. The relaxation oscillations as temporal fluctuations of the electron density are visible. | 45 |
| 3.5 | Internal quantities of an InP microdisk laser: charge carrier density, material gain and modal intensity (from top to bottom). | 46 |
| 3.6 | Photographs of the wafer-scale measurement apparatus used throughout the work. a) Overview and b) close-up view of the measurement apparatus. | 51 |

| | | |
|------|--|----|
| 3.7 | Static performance characteristics of an InP microdisk lasers. Left axis: Fibre-coupled output power; and right axis: Bias voltage vs. electrical bias current. | 52 |
| 3.8 | a) Lasing spectrum of a free-running microdisk laser. b) Lasing linewidth of the lasing mode around 1590 nm at 3.53 mA bias. | 53 |
| 3.9 | Threshold current extraction. a) Logarithmic plot of the output power vs. current for different temperatures. b) T_0 extraction: threshold current vs. temperature. | 54 |
| 3.10 | Small-signal bandwidth extraction: the transfer parameter S_{21} . The extracted bandwidth is 12 GHz. The S_{21} measurement data are a courtesy of O. Raz (TU Eindhoven). | 55 |
| 3.11 | Small-signal equivalent circuit of an InP microdisk laser. The model is equivalent to small-signal equivalent circuit (SSEC) used to model vertical cavity surface-emitting lasers (VCSELs) [11]. | 56 |
| 3.12 | Small-signal measurements of InP microdisks. Real and imaginary part of the small-signal scattering parameter S_{11} , and the fit to the small-signal equivalent circuit given in Fig. 3.11. | 57 |
| 3.13 | Small-signal measurements of the pads. Real and imaginary part of the small-signal scattering parameter S_{11} , and the fit to the small-signal equivalent circuit given in Fig. 3.14. | 58 |
| 3.14 | Parameter extraction of the pad parasitics. Top left: Microscope image of the truncated pads by focused ion beam (FIB) cut. The FIB cuts have been performed by A. Fuhrer (IBM Research - Zurich). Top right: Extracted small-signal equivalent circuit. The dominating pad-to-ground capacitance is $C_1 = 59$ fF. Bottom: Small-signal equivalent circuit of the pads. | 59 |
| 4.1 | Switching of a microdisk laser (MDL)-based flip-flop. a) Falling edge and b) rising edge of the optical flip-flop. Note that the injected pulse reflected by the grating couplers screens the rising edge in the experiments. The measurement traces are a courtesy of L. Liu (Ghent University) | 63 |
| 4.2 | Temporal response of the electron density when switching, i.e., reverting the state of operation of the MDL-based optical flip-flop every 500 ps. | 63 |

| | | |
|-----|---|----|
| 4.3 | Simulations to investigate the ultimate switching performance of InP MDL-based optical flip-flop. a) Injection of an optical pulse with varying pulse energies (black curves) from 0.6 to 1.0 fJ. The emitted power of the central lasing mode of the device is shown in red. The device reverts its operation state for pulse energies as low as 0.7 fJ. b) Injection of an optical pulse with varying pulse widths from 15 to 35 ps. The device reverts operation for pulsed as short as 20 ps. | 64 |
| 4.4 | Illustration for cascading. | 66 |
| 4.5 | a) Illustration for fanout. b) Simulated fan-out. | 67 |
| 4.6 | a) Illustration for signal refreshing including signal re-amplification, signal re-shaping and signal re-timing. b) Simulated signal re-generation properties of a MDL-based all-optical flip-flop. | 68 |
| 4.7 | Illustration for optical isolation. | 69 |
| 5.1 | Device structure of an MDL heterogeneously integrated on a silicon-on-insulator waveguide. The InP cavity is mounted on top of a pre-structured silicon nanophotonic waveguide using divinylsiloxane-bis-benzocyclobutene (BCB) as adhesive material and electrically connected using platinum-gold metal pads. | 73 |
| 5.2 | Operation of a disk laser as a wavelength converter. (a) Free-running (FR) lasing with predominant λ_{FR} . (b) Light is injected into the suppressed side-mode (λ_{INJ}) to injection-lock the laser, resulting in suppression of λ_{FR} . (c) If the injected light is modulated, the laser is wavelength converting the signal at λ_{INJ} to λ_{FR} | 74 |
| 5.3 | a) Top: Lasing spectrum for $I_{LO} = 2.72$ mA with and without external injection. Bottom: Lasing spectrum for $I_{HI} = 3.53$ mA with and without external injection. b) Eye diagrams for dynamic operation at 2.5 Gb/s. Top: With bias current $I_{LO} = 2.72$ mA. Bottom: with bias current $I_{HI} = 3.53$ mA | 75 |
| 5.4 | Measurement setup for the dynamic wavelength conversion experiments | 76 |
| 5.5 | Bit-error rate measurements of the MDL and the back-to-back (B2B) system at a 2.5 Gb/s. The bias current is $I_{HI} = 3.53$ mA. | 77 |

| | | |
|-----|---|----|
| 5.6 | Simulted eye diagrams for wavelength conversion with 50 μW external injection. a) Without seeding at 10 Gb/s and b) Without seeding at 20 Gb/s. | 78 |
| 5.7 | Eye diagrams for wavelength conversion with 50 μW external injection: a) with seeding with a power of 2 μW at 10 Gb/s and b) with seeding with a power of 5 μW at 20 Gb/s. c) Measured eye diagram at 10 Gb/s with seeding. d) Measured eye diagram at 20 Gb/s with seeding. The measured eye diagrams are a courtesy of Dr. Oded Raz, TU Eindhoven. | 79 |
| 6.1 | Photo-current generated in the InP microdisk photo detector as a function of bias and wavelength. | 82 |
| 6.2 | Responsivity of the InP microdisk used as a photo detector as a function of bias and wavelength. | 83 |
| 6.3 | Small signal response of the InP microdisk used as a photo detector. The black broken line indicates a commercial 43 Gb/s photoreceiver. | 84 |
| 6.4 | Bit error-rate measurements of the InP microdisk used as a photo detector at 2.5, 5.0 and 10 Gb/s and a pseudo-random binary sequence (PRBS) length of $2^{31}-1$ | 85 |
| 7.1 | Device structure of an InP microdisk modulator heterogeneously integrated on a SOI waveguide. a) Schematic view of the final device including the final metalization. b) Optical microscope image of the InP microdisk modulator before the final pad metallization. | 88 |
| 7.2 | a) Static electrical I-V-characteristics of more than 30 microdisk modulators on same chip. Device investigated is highlighted b) Static optical transmission curves of measured device highlighted in 7.2 a) for positive bias voltages. | 90 |
| 7.3 | Dynamic measurements of the forward-biased InP microdisk modulator a) Bit error rate measurements at 1.0 Gb/s for inverting and non-inverting operation, and at 2.5 Gb/s for inverting operation. b) Eye diagram for inverting operation at 1.0 Gb/s. c) Eye diagram for non-inverting operation at 1.0 Gb/s. | 91 |

| | | |
|-----|---|-----|
| 7.4 | a) Static electrical characteristics of the negatively-biased InP microdisk modulator with and without light in the waveguide. The image also displays the dark IV-curves for more than 30 devices on the same chip. b) Static optical characteristics of the InP microdisk modulator. Transmission characteristics of one device for several negative bias voltages. | 93 |
| 7.5 | Measurement apparatus for high-speed measurements (eye diagrams and bit-error rate (BER) test). | 94 |
| 7.6 | Electro-optical small signal bandwidth S_{21} of the negatively-biased microdisk modulator. The broken black lines are reference measured with a commercial 40 Gb/s LiNbO ₃ modulator. | 95 |
| 7.7 | Optical eye diagrams of the negatively-biased InP microdisk modulator: a) at a bit rate of 2.5 Gb/s, b) at a bit rate of 5.0 Gb/s. c) at a bit rate of 10 Gb/s, and d) electrical eye at a bit rate of 10 Gb/s and using an ac-coupled photo receiver. | 96 |
| 7.8 | a) Bit-error rate measurements of the negatively-biased InP microdisk modulator and a commercial modulator with bit rates of 2.5, 5.0 and 10.0 Gb/s. Eye diagrams for operation at 10 Gb/s and b) a PRBS length of 2^7-1 c) a PRBS length of $2^{31}-1$. | 97 |
| 8.1 | Optical output power of an InP MDL for different coupling coefficients α_c under continuous electrical bias. | 103 |
| 8.2 | Effects on optical properties of via opening: a) SEM image of a FIB-cross section of an InP microdisk with a via that is too close to the edge, or too large. b) Influence of metal absorption on the quality factor Q of the fundamental mode. The distance of the metal of the left image is indicated. | 105 |
| 8.3 | An InP microdisk with improved coupling. The coupling length of the waveguide is increased by meandering the waveguide around the disk cavity. | 107 |
| 8.4 | Lasing spectrum of an InP microdisk with improved coupling by meandering the waveguide around the disk cavity. The bias current was 2.5 mA resulting in a lasing power -26 dBm of the central mode at 1559 nm. The side-mode suppression ratio (SMSR) was determined to 36 dB. | 108 |

| | | |
|------|--|-----|
| 8.5 | Parameter variation analysis of an InP microdisk laser with 15 μm diameter. The parasitic pad- and wiring-capacitance C_p and the series resistance of the device R_s were varied with respect to the original extracted values $C_{p,0}$ and $R_{s,0}$ presented in section 3.3.2. | 110 |
| 8.6 | Parameter variation analysis of an InP microdisk laser with 15 μm diameter. The active region capacitance C_a and resistance of the active region of the device R_a were varied with respect to the original extracted values $C_{a,0}$ and $R_{a,0}$ presented in section 3.3.2. | 110 |
| 8.7 | Parameter variation analysis of an InP microdisk laser with 7.5 μm diameter. The parasitic pad- and wiring-capacitance C_p and the series resistance of the device R_s were varied with respect to the original extracted values $C_{p,0}$ and $R_{s,0}$ | 112 |
| 8.8 | Parameter variation analysis of an InP microdisk laser with 7.5 μm diameter. The active region capacitance C_a and resistance of the active region of the device R_a were varied with respect to the original extracted values $C_{a,0}$ and $R_{a,0}$ | 112 |
| 8.9 | Cross-section of the investigated partially etched grating couplers. a) Cross section after structuring the front-end-of-line (FEOL) by partially etching to form the grating teeth and fully etching for form the waveguides. b) Cross-section after cladding the grating couplers capped with a silicon nitride layer and subsequent first metal oxide (M1) planarized oxide. c) Cross-section of the layer stack after completing all process steps. Note that only layers influencing the optical performance of the grating couplers are shown for sake of clarity. | 115 |
| 8.10 | Partially etched grating couplers for wafer-scale testing throughout the fabrication of a complementary metal oxide semiconductor (CMOS) process. | 116 |
| 8.11 | Focusing partially etched grating couplers: layout and spectral response. | 118 |
| 8.12 | Spectral response of the improved grating couplers when using an index-matching liquid. | 119 |
| 9.1 | Schematic view of a potential implementation of an InP microdisk-based optical transceiver chip. | 127 |

List of Tables

| | | |
|-----|--|----|
| 2.1 | Epitaxial layer stack of the lasing material used in this work. The epitaxial stack comprises three InAsP quantum wells and a tunnel junction to enable a single metallization step [12]. The total thickness of the layer stack is 583 nm [13]. | 26 |
| 3.1 | Parameters used in the radially depended microdisk laser models. The values are taken from literature [9, 14], measured [15] or based on the device geometry. | 44 |
| 4.1 | Parameter used in the 1D radially depended microdisk laser model. | 71 |
| 7.1 | Comparison of the present work with state-of-the-art modulators in terms of drive voltage, area, speed, static extinction ratio and energy consumption per bit [16]. | 98 |

List of Acronyms

| | |
|--------|---|
| ac | alternating current |
| APD | avalanche photo-diode |
| ASE | amplified spontaneous emission |
| ASIC | application-specific integrated circuit |
| AWG | arrayed waveguide grating |
| BCB | divinylsiloxane-bis-benzocyclobutene |
| BEOL | back-end-of-the-line |
| BER | bit-error rate |
| BiCMOS | bipolar complementary metal oxide semiconductor |
| BR | bit rate |
| CAD | computer-aided design |
| CCW | counter-clock-wise |
| CMOS | complementary metal oxide semiconductor |
| CMP | chemical-mechanical polishing |
| CNC | computerized numerical control |
| CPU | central processing unit |
| CW | clock-wise |
| dc | direct-current |
| DFB | distributed feed-back |
| DOS | density of states |
| DRC | design rule check |
| EDFA | erbium-doped fibre amplifier |
| FCA | free-carrier absorption |
| FDTD | finite-difference time-domain |

| | |
|---------|--|
| FEC | forward error correction |
| FEOL | front-end-of-line |
| FIB | focused ion beam |
| FSR | free-spectral range |
| GDSII | graphic data system II |
| Ge | germanium |
| HCl | hydrochloric acid |
| ICP | inductively-coupled plasma |
| InAsP | indium arsenide phosphide |
| InGaAs | indium gallium arsenide |
| InGaAsP | indium gallium arsenide phosphide |
| InP | indium phosphide |
| IO | input-output |
| LVS | layout versus schematic |
| MDL | microdisk laser |
| Meep | MIT electromagnetic equation propagation |
| MPB | MIT photonic bands |
| MPW | multi project wafer |
| MQW | multiple quantum well |
| NRZ | non-return-to-zero |
| OOK | on-off keying |
| OSA | optical spectrum analyzer |
| OSNR | optical signal-to-noise ratio |
| PC | polarization controller |
| PD | photo diode |
| PECVD | plasma-enhanced chemical vapour deposition |
| PIC | photonic integrated circuit |
| PIN | positive intrinsic negative |

| | |
|-------|---|
| PL | photoluminescence |
| PLC | planar lightwave circuit |
| PPG | pulse pattern generator |
| PRBS | pseudo-random binary sequence |
| QCSE | quantum confined Stark effect |
| RF | radio-frequency |
| RIE | reactive ion etching |
| SEM | scanning electron microscope |
| SiGe | silicon-germanium |
| SLED | super-luminescence light-emitting-diode |
| SMSR | side-mode suppression ratio |
| SOA | semiconductor optical amplifier |
| SOI | silicon-on-insulator |
| SSEC | small-signal equivalent circuit |
| TEC | thermo-electric cooler |
| TIA | trans-impedance amplifier |
| Tx | transmitter |
| VCSEL | vertical cavity surface-emitting laser |
| VLSI | very large-scale integration |
| VNA | vector network analyzer |
| VOA | variable optical attenuator |
| WDM | wavelength division multiplexing |

1 Introduction

The present chapter introduces and motivates the work described in this thesis. First, an introduction to tele-communication and data-communication systems is given. It is then discussed how photonic integration enables the convergence of optical systems for tele-communication applications and optics for computing. The unsolved challenges in the field of photonic integration are described, which are addressed by this work. Moreover, the major scientific and technological contributions of this thesis are discussed. The open challenges in the field are described and the outline of this thesis is presented.

1.1 Optical communication systems

Tele-communication systems The invention of the electromagnetic telegraph by Samuel F.B. Morse and Joseph Henry in 1837 was the initial spark for tele-communication enabling the electromagnetic transport of information over large distances [1]. From that day on a huge development in electrical communication systems initiated the creation of an enormous infrastructure for tele-communication using radio waves as the information carrier. In the first communication systems operators had to manually encode or decode the signal into so-called *Morse code* using an apparatus as shown in Fig. 1.1 a), resulting in a performance of several thousand bytes per working day. Today's tele-communication systems enable the transmission of several billions of bytes per second. The tremendous progress made in tele-communication enabled today's information society. The tele-communication network spans a dense grid over the globe ranging from long-haul undersea cables, over metro networks until fibre-to-the-home solutions challenging electronic solutions even in access networks. Bandwidth is available everywhere and at any time, enabling hand-held devices that were formerly meant for telephony to stream videos in full high-definition quality. These recent developments were only made possible by the development of long-haul optical communication links that allow the transmission of data over large distances. Fig. 1.1 b) shows as an example of state-of-the-art in tele-communication equipment Cisco's carrier routing system CRS-3, which can be scaled to an impressive total bandwidth of 322 Tbps [2].

Electronic solutions using radio waves have been replaced by optical

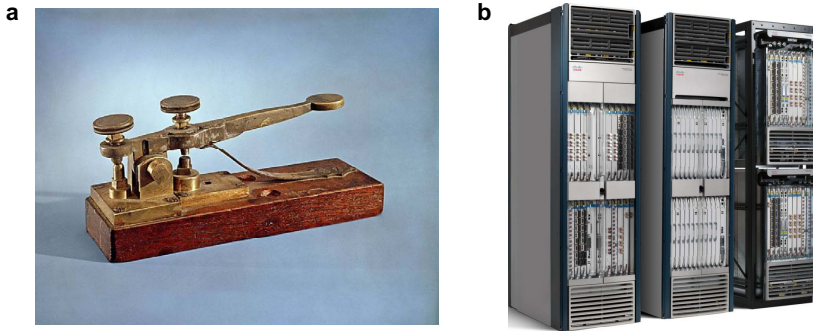


Figure 1.1: State-of-the-art in tele-communication systems at different points in time: a) 1837 - the telegraph presented by Samuel F.B. Morse and Joseph Henry [1]. b) 2012 - Cisco's carrier routing system CRS-3 [2].

communication since the invention of the erbium-doped fibre amplifier (EDFA) and the low-loss optical fibre. The invention of the EDFA by Charles J. Koester and Elias Snitzer [17] in 1964 enabled the amplification of signals in the optical domain without the need to convert the signal from the optical to the electrical domain, electrical amplification, and re-conversion to the optical domain. The low-loss optical fibre invented by Charles Kuen Kao in 1966 [18] allowed to transmit information in the optical domain over large distances, e.g., across the Atlantic ocean connecting Europe with North America. Only optical technologies using fibres enabled these high-speed long-haul transmission links, where electronic solutions were not feasible in terms of bandwidth limitations, power consumption and cost. The fibres used for tele-communication are commonly single mode fibres with dispersion minimum around 1300 nm and propagation loss minimum at 1550 nm supporting multiple wavelength such that the bandwidth per fibre can be increased by using WDM [19]. Also, each wavelength can be encoded using on-off keying (OOK), or higher order modulation formats to improve the spectral efficiency of the fibre to carry more information per unit spectral bandwidth.

Data-communication systems The initial work that paved the way towards the computing era was the demonstration of a programmable machine by Konrad Zuse in 1943, which was based on relays that could perform computations [20]. After the invention of the semiconductor transistor by

John Bardeen, Walter H. Brattain and William B. Shockley in 1947 [21] and the capability to integrate several of these devices to form integrated circuits based on the inventions of J. Kilby and R. Noyce in 1959 [22, 23] the reliability, complexity and power consumption of these computing machines could be substantially improved. Already in 1965 Gordon Moore predicted that the number of devices per integrated circuit would double every year [24], which turns out to be true still today, though at a slightly larger time interval of about 2 years.

After about 50 years of research and development, today's fastest supercomputers and data centres are capable of performing several hundreds of thousands of operations per nanosecond. These machines do not only have very high computing performance, but also a power consumption of several megawatts [25], which is going to increase further over the next years. Unless new technologies for high-performance computing systems are developed, exa-scale supercomputers will break the 200-MW-limit by 2018 [26]. Already today, the carbon dioxide footprint of data centres and supercomputers has exceeded that of worldwide aviation. Improving the efficiency of the communication systems in these machines plays an important role in reducing overall power consumption. The use of optical communication technologies are a viable path towards low-power high-speed interconnects.

The size of supercomputers and data centres is going to increase even further, requiring very large bandwidth at large distance, where electronic solutions are running out of steam [27]. Optical solutions are the only feasible approach to transport the processed data from computing elements to storage elements and back, and to enable continuous performance scaling with the same pace as in the past.

In today's machines the internal bandwidth of supercomputers is still largely supplied by electronic chip-level and board-level communication. For larger distances, however, such as rack-to-rack and card-to-card communication, the bandwidth is increasingly supplied by optics. One common implementation for rack-to-rack communication are multi-mode active optical cables [3]. Fig. 1.2 shows a photograph of the fastest European supercomputer by the end of 2012. In this image, the optical cables routed on top of the compute nodes are clearly visible. Given the amount of fibres and connectors, which all have to be installed manually, this approach is costly and becomes increasingly difficult to handle as the number of the optical connectors is further increased. This installation method is time



Figure 1.2: View from the top of IBM’s *SuperMUC* supercomputer installed at Leibniz Rechenzentrum (LRZ) in Munich, Germany in 2012. Image is a courtesy of IBM Research - Zurich. The orange wiring on the top are active optical cables linking compute nodes and storage servers [3].

consuming and is expected to impair system reliability and failure rates for larger systems.

To enable easier wiring of the optical fibres, and also to enable optical communication not only from rack-to-rack, but also within a rack from drawer-to-drawer at a higher density, optical IO link technology has become of large interest. Demonstrators based on polymer waveguide technology are for example electro-optical backplanes [28], flexible optical multi-lane links [29] and board-level optical interconnects [4, 30] as shown in Fig. 1.3 a). Even the direct optical interconnection to the (processor) package has been presented recently [5] as shown in Fig. 1.3 b).

All the recent above-mentioned advances in the field of optical link technology employ multi-mode fibres and VCSEL-based electro-optical transceivers operating at around 850 nm. With this technology only relatively simple coding schemes, such as OOK or multi-level amplitude modulation, can be employed at a single wavelength, which implies that only one data signal can be guided per fibre.

1.2 Towards photonic integration

In tele-communication systems there is a clear trend towards the integration of photonic components on one single die to increase the performance of the systems. In addition, photonic integration enables to integrate more

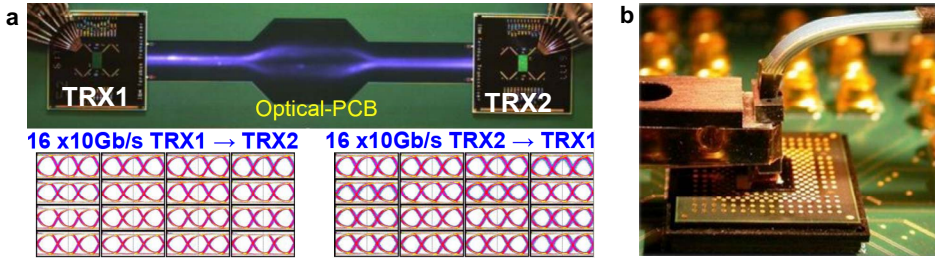


Figure 1.3: State-of-the-art in optical interconnect technology. a) Optical printed circuit board using 850 nm multi-mode technology [4]. The insets at the bottom illustrate the data transmission from transmitter 1 (TRX1) to TRX 2 and back-wards. b) Optical transceiver technology with direct carrier connections [5].

functionalities on a single chip enabling more complex systems. Beyond this, also the advantages associated with integration known from electronics play an important role. The integration density can be improved, which increases the component count per unit area and thus reduces the cost. The reduction of the component size also reduced the parasitics of the components boosting device performance. Because of the large-scale integration of photonic components they can be more standardized compared to bulk optical technology. Also, in analogy to electronics, the yield and reliability of these standardized components has the potential to exceed that of bulk optical technology.

In optical data-communication systems one of the main drivers towards photonic integration is the number of optical IO interfaces per chip or die, which in analogy to the electrical pin-count, can be regarded as an *optical pin-count*. Today's supercomputers employ multi-mode transceiver technology as it still offers cost benefits over single-mode transceiver technology. Multi-core fibre solutions are a viable option for the near future as they enable to route several optical signals per fibre. However, the further scaling of such technology is difficult and requires an alternative path for reducing the optical pin-count. It is expected that exa-scale computing systems based on single-core multi-mode transceivers will break the 100-Mio.-fibre-limit. This enormous optical cabling overhead would result in severe installation and reliability challenges and would account for a substantial cost fraction of the system and is thus to be avoided.

Therefore, it is becoming more and more attractive to use photonic

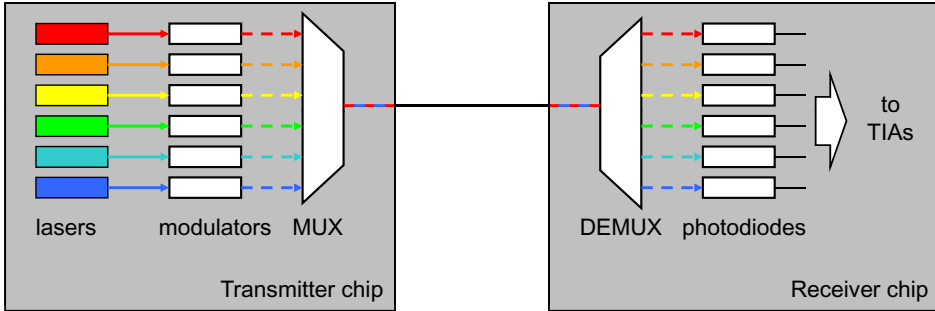


Figure 1.4: Generic scheme of a transmitter and receiver chip using WDM. From left to right: The transmitter comprises several lasers, which are then individually modulated. Then, the signals are multiplexed into one single waveguide, which is then coupled to a fibre and transmitted to the receiver chip. Here, the signal is de-multiplexed and detected by an array of photodiodes. The generated photocurrents may then be amplified by a TIA.

integration also for computing applications, as this technology offers to integrate optical components at a higher density than VCSEL technology. One example of such technology is silicon photonics, which makes use of the fact that silicon is transparent in the near-infrared, enabling to form single-mode waveguides supporting wavelengths in the 1300 nm and 1550 nm range. Also, optical signals may be amplified using semiconductor optical amplifiers (SOAs) or EDFAs.

Convergence of tele- and data-communication Photonic integration enables the further scaling of system complexity and functionality - both for optical data-communication and optical tele-communication. More complex functions can be integrated at reduced cost. Photonic integration enables data-communication systems to transport more bandwidth per fibre by employing WDM similar to long-haul tele-communication systems. Furthermore, in computing applications the optical communication systems would also benefit from reduced packaging and installation cost, as less connections (i.e., optical pin-count) are needed if multiple wavelengths are guided in one optical fibre. Secondly, for computing applications the power consumption is a critical aspect, where the lowest power consumption per bandwidth in terms of mW/(Gb/s) is highly demanded. A reduction of the power consumption can be achieved by short metal in-

terconnection lengths and small devices enabled by photonic integration. Thirdly, the cost for the optical links and electro-optical transceiver modules per optical bandwidth in terms of $\$/(\text{Gb/s})$ is to be reduced compared to single-mode long-haul tele-communication technology, where the price per module is shared by multiple users, and also the economical life-time for each technology is longer than for computing applications. The cost reduction can be achieved by implementing a large number of components on a single substrate. Potentially, also the fabrication processes may be shared between several customers sharing the fabrication costs on larger substrates [31]. Another advantage of photonic integration is that it enables the fabrication of low-cost optical single-mode devices. Single-mode technology enables larger link distances than multi-mode technology, making this technology attractive for systems with a larger foot-print, or where a spatial separation between, e.g., compute nodes and storage capacity is required. Single-mode technology is also required to route multiple wavelengths in one single waveguide or fibre. This so-called wavelength-division multiplexing (WDM) allows to transport more bandwidth per waveguide or fibre and can substantially increase the aggregate bandwidth of photonic circuits or chips. A schematic of such a transmitter and receiver chip is shown in Fig. 1.4.

The above mentioned aspects lead to a growing interest in employing photonic integration to enable also WDM approaches and possibly also higher-order modulation formats for computing applications. In conclusion, both tele-communication and computing applications strive for an increase in bandwidth enabled by photonic integration. Both applications require tighter integration to achieve an increase in speed and functionality. The main motivation for tele-communication systems is improved performance, in terms of spectral efficiency or line rate. For computing applications power consumption per bandwidth, cost per bandwidth and reduction of optical pin-count are the main drivers for optical integration. Yet, in the field of optical integration several challenges are unsolved, which are described below.

1.3 Unsolved challenges of optical communication systems

Design methodology Electronics has made a tremendous progress over the last decades mainly based on very-large scale integration concepts, such as CMOS technology. However, also the corresponding design methodology

plays a significant role in the progress in the field of electronics. The key feature of electronics, in particular digital electronics, is that the design can be de-coupled from the fabrication by accurately modelling the device behaviour and physics in so-called compact models allowing the designer to precisely predict device performance of transistors and to accurately simulate subsystems, and even more complex circuits. This approach enabled the creation of wide-spread computer-aided design (CAD) tools allowing for rapid design of electronic components. During the design phase the implementations are restricted to geometries that can be fabricated reliably. To check if the design will be able to be fabricated it has to pass the design rule check (DRC). Besides this, the design also has to pass layout versus schematic (LVS) check. This routine investigates whether the electronic circuit schematic matches the transistor layout. All these aforementioned measures, if applied correctly, allow for working silicon after the first design iteration and fabrication run.

In contrast to electronics, the design of photonic components is less advanced because different applications require different optical components, which in turn are less standardized and typically application-specific. In a photonic design flow typically the physical properties of optical components are simulated using *ab-initio* methods, such a FDTD simulators solving Maxwell's Equations in the time-domain requiring large computational power. Several geometries and devices concepts are simulated in the physical domain and are then implemented in a layout without undergoing an intermediate level of abstraction using compact models. By simulating optical devices in the physical domain the device behaviour may be simulated very accurately, however the lack of abstraction limits the simulation of larger photonic circuits.

It is therefore imperative to eventually implement compact models similar to electronics enabling true large-scale integration of photonic circuits. Also, the co-design of electronic and optic functions would benefit from a seamless design methodology enabling large-scale high-performance optoelectronic systems. Furthermore, by adhering to electronic design methodology including DRC and LVS also working optical components will be guaranteed in the first fabrication run saving costly iterations before yielding fully functional photonic integrated circuits.

Packaging Packaging of optics is one of the grand challenges for today's and future optical communication systems, in particular for the application in high-performance computing systems. Whereas today's optical components are based on active alignment causing a substantial cost fraction of the optical modules, e.g., active optical cables, future electro-optical transceivers need to rely on passive alignment strategies to enable cost-efficient packaging solutions for a large number of optical connectors. The alignment tolerances of optical fibres with respect to optical components are related to the modal field diameter. The larger the mode field diameter is, the larger is the alignment tolerance. The current trend towards photonic integration reducing the foot-print of optical components implying a reduction of the mode field diameter is in stark contrast to this. Even more precise alignment strategies are required, e.g., for single mode nanophotonic waveguides on silicon, which have a large index contrast with respect to the surrounding materials. In these waveguides the mode field diameter is less than one micrometre in diameter requiring alignment precision in the order of a few tens of nanometres to sustain coupling losses smaller than 1 dB. This challenge may be partially relaxed by introducing polymer tapers [32] or vertical grating couplers [33], which are both based on expanding the mode field diameter of the waveguides. Both approaches have significant draw-backs. Whereas the former approach requires to guide the optical signal to the edge of the die resulting in increased real-estate overhead and typically additional non-CMOS-compatible processing steps, the latter approach results in a reduced efficiency and a limited wavelength operation range.

In order to support the further scaling of photonic components, regardless of the technology they are based on, it is required to develop a low-loss coupling scheme allowing for passive alignment of a large number of optical chip interfaces to optical fibres or waveguides. Approaches based on photonic wire-bonds have been developed recently, which fulfil some of the requirements, but are currently serial and thus not yet well-suited for large optical pin-counts [34]. Ideally, the assembly should also make use of electronic packaging infrastructure using solder-based attachment concepts and positioning schemes resorting to pick-and-place machines. The passive alignment strategies should be compatible with the alignment tolerances associated with these assembly methods.

Large-scale co-integration of electronics and optics Partially hampered by the aforementioned different design methodology of optics and electronics, there has not yet been a seamless technology demonstration comprising both electronic and optical circuits on a single chip of wafer. Although a co-integration of electronics and optics on a single-component level was demonstrated [35], the co-integration of photonic integrated circuits with a large number of components remains to be demonstrated. Typically the optical and electronic functions are realized on individual dies that are then hybrid assembled and wire-bonded on a common substrate [6]. One aspect that retarded the integration of optics together with electronics is the variety of optical applications that hinder standardization and the variety of optical materials that hamper integration into an electronics environment. A truly seamless integration technology would combine both electronic and optical functions on a single substrate or die, and ideally sharing the same material in the same device layer such that electronic and optical components share the same processing steps resulting in high yield and low cost.

Whereas approaches have been presented in which optical components were formed in the device layer of SOI structures [31, 36, 37], so far no co-integration with electronics was presented. Recently, first demonstrators based on silicon photonics were presented in which the co-integration approach of combining electronic and optic functions in a single device layer was shown to be technologically feasible [38, 39] and eventually suitable to fabricate high-speed optical receiver modules [40] paving the way towards the co-integration of electronic and optics. Whereas the presented results are promising for, e.g., electro-optical transceivers [40], large-scale photonic integrated circuits with a high component count driven by CMOS electronics fully leveraging the potential of very large-scale integration (VLSI) CMOS technology remain to be demonstrated.

Low-power wavelength converters with high conversion efficiency

Today's tele-communication networks employ WDM to transport more data per fibre compared with a single wavelength. The number of independently supported wavelengths is usually large enough to transport the desired aggregate bandwidth, but is smaller than the number of addressed nodes. This implies that optical switching functions are required to route data to the appropriate receiver node. This may be implemented by, e.g.,

wavelength interchanging cross-connects [41], which rely on the dynamic re-arrangement of wavelengths. Also, when several signals compete for one node, wavelength conversion may be employed for contention resolution [42].

For these applications fast and also low-power wavelength converters are required. These converters should have a high conversion efficiency alleviating the need for post-amplification after the conversion process. Furthermore, if WDM schemes may be employed for future computing systems, small footprint and low-power consumption will become even more important.

State-of-the-art wavelength conversion systems are usually based on four-wave mixing [43, 44] or cross gain modulation of single-pass devices [45, 46] and thus power hungry. It is therefore required to improve these wavelength conversion systems to enable fast, low-power wavelength converters with a high conversion efficiency.

Compact, high-speed, low insertion-loss integrated modulators

Modulators are used to encode data signals onto continuous-wave light. Although these devices are extensively explored and widely used in optical communication systems, they still offer a large potential for improvements. In particular integrated modulator concepts used for silicon photonics are designed under the boundary conditions of the absorption and/or phase shift properties of silicon [47]. These silicon-based modulators are designed to offer the ideal trade-off between insertion loss, operation speed, extinction ratio and size for a given application. Whereas forward-biased modulators offer a large extinction ratio and thus can be fabricated with short lengths, they suffer from limited device speed [48]. In contrast, negatively-biased modulators benefit from high operation speed [49], but suffer from the larger interaction lengths, high drive voltages and limited extinction ratios, resulting in large millimetre-scale structures. Therefore further research is required on integrated modulators compatible with silicon photonics, which combine small foot-print, low drive voltage with high extinction ratio and small insertion loss.

Light source for silicon photonics Out of the large pool of optical integration technologies that are discussed in Chapter 2 in detail, silicon photonics is one of the most promising technology platforms. The advantage

of this technology compared to the competing approaches is the possibility to tightly integrate electronics and optics as mentioned above. The most important advantage of silicon photonic is that the well-established VLSI CMOS fabrication process can be used, allowing for very high control over the devices, unparalleled yield and unsurpassed reliability.

The major challenge in silicon photonic research is the lack of a light source because of silicon's indirect bandgap, which prevents silicon from emitting light efficiently at room temperature. Several approaches to achieve a light source for silicon photonics have been pursued, which are discussed in chapter 2. Out of these approaches heterogeneous integration of InP microdisk lasers is a viable route towards on-chip lasers as described in section 2.2.

In-line wafer-level testing of photonic components The large scale integration technology of electronics makes use of in-line process monitoring, in which the performance figures of test structures are monitored during the fabrication to ensure working devices after the fabrication, and to track potential process deviations. Test structures are therefore required that enable to access the devices during the fabrication. Also, these test structures need to be accessible from the surface enabling vertical probing in a parallel manner.

Although wafer-scale testing is applied for, e.g., VCSELs, performance and yield of optical components are typically monitored on a single component level after the fabrication, which is time consuming and costly. Furthermore, deviations from the ideal fabrication process are difficult to be identified and to be monitored. The main reason for this testing strategy is that optical components typically rely on lateral coupling schemes and coupling can only be performed after cleaving of the optical die.

For testing optical components it is therefore attractive to implement testing schemes, which enable vertical coupling [33]. Although vertical testing schemes based on grating couplers have been widely investigated, mainly for coupling purposes, so far the integration of vertical coupling schemes enabling wafer-scale testing capabilities to monitor the performance of optical components throughout the entire fabrication process of optical components remains to be demonstrated.

Unsolved challenges addressed by this thesis Out of the numerous unsolved challenges mentioned above in section 1.3, this thesis addresses in particular the missing **light source for silicon photonics**, which is investigated in the form of InP microdisk lasers.

This thesis investigates these electrically driven InP microdisks not only as lasers, but also for other applications, for which these devices may be used, such as **high-speed all-optical wavelength converters**. Although the forward-biased operation mode of the devices has been explored [9, 50, 51], the negative bias regime caught less attention. Under this bias condition the microdisks can be operated as a **low-power high-speed modulators**, and also as resonant photodetectors as will be shown in the course of the manuscript.

In due course of the work carried out in this thesis it was found that the measurements were partially limited by the performance of the grating couplers masking the actual device performance. Therefore, grating couplers were investigated with the focus of a large bandwidth and low optical response distortion in order to characterize on-chip optical devices, such as InP microdisks or WDM components [52]. These grating couplers may be used for the characterization of the final fabricated optical components, but may also be used as **optical probe-pads for in-line performance monitoring of photonic components**, as will be shown in this thesis.

1.4 Contributions of this thesis

The objective of this thesis is to address some of the yet unsolved challenges described in section 1.3 above. Also, further functionalities beyond lasing applications that InP microdisks offer have been investigated. The major contributions of this work are stated below.

A spatially dependent multi-modal time-domain model for microdisk lasers Rate equation models are employed describing the physics of lasers. A rate equation model for microdisk lasers presented in [9] has been expanded for multiple modes. Furthermore, the equation system was solved in the time domain and successfully employed for modelling bi-stable mode switching in optical flip-flops [53] and wavelength conversion [54].

Dual wavelength conversion using InP microdisks Wavelength conversion is an important functionality for WDM networks [41] and is particu-

larly interesting for, e.g., contention resolution in optical switching systems. Wavelength conversion in disk lasers by exploiting the modal dynamics is well-known [55], although a study on the dynamic characteristics and speed limitations remained to be carried out. Furthermore, wavelength conversion towards either larger or shorter wavelengths has been presented. Also, some applications require the capability to perform wavelength conversions towards larger and shorter wavelengths using the same device. For the first time, it was shown that a single InP microdisk can be used for wavelength up- and down-conversion [56, 57].

InP microdisk detectors InP microdisks can be used as photodetectors under negative bias [58]. Within this thesis the spectral response of the photocurrent and responsivity was reported, also the temporal behaviour of this operation mode was studied and operation up to 10 Gb/s was demonstrated [59]. This result is very promising as it clearly demonstrates that the same device can be used for light emission and detection enabling half-duplex optical links.

InP microdisk modulators Although the concept of using InP microdisks as modulators using carrier-injection has been presented [50], no detailed study on the temporal behaviour of the conversion process was performed yet. In addition, within this work a study on inverting and non-inverting operation under forward bias conditions was carried out. For the first time also negative-biased InP microdisk modulators suitable for high-speed operation up to 10 Gb/s were presented [60, 61].

In-line optical probe pads in CMOS process Grating couplers have been used in this work to couple light in and out of the chip. These grating couplers have a bandwidth that is too small for some applications or experiments. Therefore detailed investigations on how to improve grating couplers have been performed. In the context of this thesis, for the first time it was shown that grating couplers can be used as optical probe pads in analogy to their electrical counterparts to characterize silicon photonic devices throughout the entire CMOS fabrication flow [62].

1.5 Outline of this thesis

The thesis is organized as follows: Chapter 2 presents the state-of-the-art in optical integration technology and describes which technology is used in this thesis, and why. In Chapter 3 the application of an InP microdisk as a laser is explained. Also the device is modelled and a parameter extraction scheme is presented. Static and dynamic performance figures are presented and discussed. Chapter 4 discusses the requirements of all-optical optical systems and whether InP microdisk laser-based all-optical flip-flops can be used as logic elements. The model presented in Chapter 3 is used to investigate the ultimate switching behaviour of these all-optical flip-flops. Chapter 5 contains a detailed study on microdisk-based all-optical wavelength converters. The underlying switching mechanism is explained before static and dynamic characteristics are presented. The performance limitations of the wavelengths conversion process are analysed by employing the multimodal laser model presented in Chapter 3. Chapter 6 covers the use of InP microdisks as photodetectors under reverse bias and external illumination. Chapter 7 highlights the application of InP microdisks as modulators, both under forward and negative bias. The static and dynamic performance under both bias conditions is presented, and speed limitations are discussed. Chapter 8 discusses several approaches how to improve the performance of the microdisk devices. Ways to improve the output power of microdisk lasers, and to improve the speed of the devices are discussed. Finally, the thesis is summarized in Chapter 9 and gives suggestions for future work in the field of InP microdisks for on-chip applications.

2 Photonic Integration Technology

The present chapter describes the photonic integration technology and fabrication methods used in this work. First, a general introduction to the state-of-the-art in optical integration is given. Then, the silicon photonics base technology and the associated design flow is presented. After highlighting the heterogeneous integration technology used within the thesis the fabrication scheme to achieve electrically contacted InP microdisks is described step-by-step.

2.1 Introduction

The field of electronics is highly standardized with CMOS technology being the workhorse and bipolar CMOS (BiCMOS) technology as a niche for applications requiring simultaneously high speed and high drive currents [63, 64]. In contrast, the field of optics is rather inhomogeneous with a variety of integration schemes. The variety is partially due to the different target applications, but also due to the relatively small market for optics compared with electronics, which hampered the standardization of optical components and the development of highly integrated photonic devices. The few most important and most promising approaches amongst the various optical integration technologies are highlighted below.

Optical integration technology evolved from the long-haul telecommunication market, where the initial target was to bridge long distances at high speed. Because the deployed infrastructure is shared by multiple users, cost is not the main driver for integration as the system cost is largely governed by fibre cost and the deployment overhead. Instead, integration is pursued to make optimum use of the installed optical infrastructure. The main research in telecommunication systems therefore focuses on improving the performance of components and sub-systems in terms of communication bandwidth, spectral efficiency and the bandwidth-span-length-product. This research and development approach is successfully pursued by some big players in the field such as Infinera focusing on high-end transceiver modules [6].

Today, optics is also required for short-reach applications in data centres and high-performance computing as described in section 1.1. This new application field also required optical integration, but partially with different figures of merit. Whereas for long-haul telecommunication performance

is the main driver and thermal stability, cost and power consumption are of less relevance, these figures become of high relevance for data communication applications. For computing applications the main driver for optical integration is the need for high bandwidth at low cost ($\$/(\text{Gb/s})$) and low power consumption per bandwidth ($\text{mW}/(\text{Gb/s})$), while spanning short to medium distances, where electronic solutions will not meet the performance requirements of future computing systems [27].

The following section describes the state-of-the-art in optical integration for both above-mentioned applications, which have partially different requirements. The optical integration technologies described below may serve both application fields and are seen as generic integration approaches.

2.2 State-of-the-art in photonic integration

This section gives an overview on the state-of-the-art in photonic integration. It is important to note that only integration schemes using a sole carrier or substrate are described forming devices that are truly integrated. In the literature also hybrid assembly schemes, in which photonic and electronic chips are assembled, wire-bonded and co-packaged in a single housing, are referred to as integrated. These approaches are not considered here as *integrated* and therefore omitted for sake of clarity. After describing the existing integration technologies the approach used in this thesis is highlighted and the advantages over the other integration approaches are discussed.

Planar lightwave circuits (PLCs) This technology refers to silicon oxo-nitride or silica-based photonic circuits integrated on a planar silicon carrier. It offers low-loss waveguides at the expense of relatively large bending radii in the order of a few hundreds of micrometers due to the low index contrast resulting in millimetre-scale PLCs. Very complex passive photonic devices have been demonstrated in this technology, such as arrayed waveguide gratings (AWGs) with up to 1000 channels, dispersion compensators for telecom applications, pulse waveform shapers, etc [65]. Recently, this technology attracted attention for optical buffering: The low-loss waveguides are interesting for integrated optical delay lines or buffers used in, e.g., optical packet switches [66].

PLCs suffer from the absence of an integrated light source, the absence of driver/receiver electronics and large bending radii. Because of this the

PLCs in this technology have a relatively large footprint, which hampers higher integration density and cost reduction.

Monolithic InP Technology This technology uses bulk InP wafers onto which epitaxial layers are grown and structured to form optical devices. By using re-growth steps this approach enables the integration of passive and also active optical functions on the same wafer or die, which is then called photonic integrated circuit (PIC). Benefits of this technology are the possibility of integrating laser sources along with passive waveguiding components and detectors, as well as a relatively high index contrast allowing for compact photonic integrated circuits. These PICs are normally fabricated with optical contact lithography resulting in micrometer-scale structures. Drawbacks of this technology are the absence of co-integrated electronics. Very complex photonic integrated circuits, such as integrated 10×100 Gb/s coherent receivers have been demonstrated [6]. Typically, this technology is used for ultra-high performance optical circuits for long-haul telecommunication applications. Fig. 2.1 a) shows a state-of-the-art 5×114 Gb/s transmitter from Infinera [67]. To achieve the required functionality several dies need to be hybridly assembled, such as the radio-frequency (RF) application-specific integrated circuit (ASIC), the mentioned InP transmitter (Tx) PIC, as well as a control ASIC. As shown in Fig. 2.1 a) the electrical connections have been realized by wire bonding resulting in more than 40 cm of wire bonds causing high fabrication cost. This together with the requirements on the package to be highly thermally conductive and to support fibre-coupling leads to unavoidably high packaging costs. Also, a further decrease in cost is hampered by the limited InP wafer size, which is typically between 50 mm to 100 mm (2 to 4 inch) in diameter to date. These wafer sizes are substantially smaller than, e.g., silicon technology, where wafer diameters up to 300 mm (12 inch) are used enabling substantially more dies per wafer.

Silicon Photonics The electronic manufacturing perfection to date allows producing billions of transistors on a single die with very high yield and limited cost due to large volume manufacturing in bulk and SOI CMOS processes. The integration of optics into this mature manufacturing technology is thus very attractive for low-cost high-yield optical devices with a large degree of complexity.

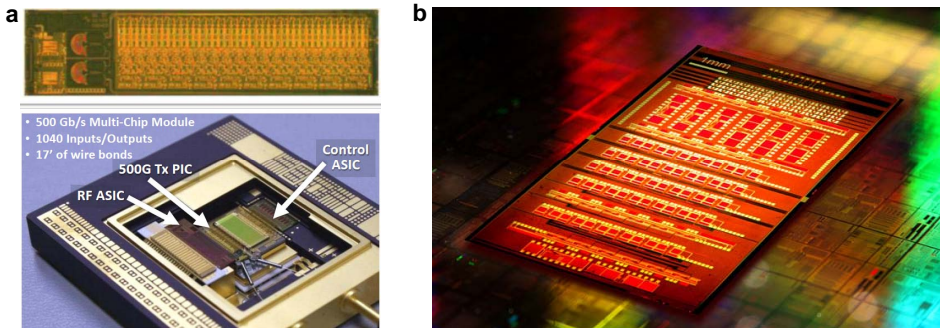


Figure 2.1: State of the art in photonic integration. a) Monolithic InP integration - as an example Infinera’s packaged 5×114 Gb/s transmitter PIC is shown [6]. b) Silicon photonics - Photograph of IBM’s SNIPER chip integrating both optical and electrical functions on the same die [7].

Silicon photonics integrates optical components in the device layer, i.e., the top silicon layer of a SOI wafer. Silicon is transparent in the near-infrared around 1300 nm and 1550 nm, lending this material to the formation of low-loss waveguides [32]. The wave-guiding effect is achieved by the high index contrast of the waveguide core formed in silicon and the low index cladding formed by the underlying buried oxide and the subsequently applied cladding layers having a lower index than the silicon waveguide.

Silicon photonics benefits from the high index contrast of the SOI material enabling very compact passive photonic devices, low loss waveguides, small bending radii and thus compact devices [32]. Various optical components with excellent performance, such as wavelength (de)multiplexers [52], grating couplers [33], etc., have been shown in this technology.

Besides passive waveguiding functions also active components may be fabricated by realising contacts and functionalized regions based on doping forming active electro-optical components, such as modulators [68]. By forming these implanted regions the waveguides are contacted and charge carriers may be injected and modulators based on the free-carrier plasma-dispersion effect may be created [48]. Electro-absorption modulators may be formed under negative bias in the carrier-depletion regime [16]. By monitoring the charge carriers generated by absorption photodiodes can be created, which can be further improved exploiting the avalanche effect between germanium and tungsten [69]. Recent demonstrations in silicon photonics include fully CMOS-integrated optical receivers operating at 40

Gb/s [40].

The possibility of integrating analog driver / receiver electronics and digital circuits together with photonics in the same silicon device layer is unique in this technology platform [7]. Except for the detectors, which require germanium (Ge) for improved responsivity, generally no additional materials or process changes are required to fabricate optical components in a SOI-CMOS fabrication process.

The major draw-back of this technology is the absence of an electrically pumped light source with sufficient efficiency and high yield. Despite recent efforts in fabricating monolithic light sources using germanium [70], silicon photonic has to resort to external laser sources, reducing the cost advantage over the other integration technologies. Viable approaches towards lasers for silicon photonics are described below.

Hybrid Optical Integration To extend the capabilities of silicon photonics two approaches are subject to extensive research, which address the issue of the missing on-chip light source: hybrid integration and heterogeneous optical integration. Both approaches start from a pre-structured passive SOI waveguide circuits onto which an active III-V based material exhibiting electrically pumped optical gain is integrated. First, hybrid optical integration is described.

In hybrid integration a III-V wafer with epitaxial layers on the surface is bonded face-down onto a silicon photonic chip using Van-der-Waals forces. Subsequently, the III-V is structured and electrically contacted to form active optical devices. The name hybrid integration originates from the fact that the light is guided as a hybrid optical mode within the silicon waveguide and the overlaying III-V material. Using hybrid integration [8], modulators [71], optical amplifiers and photodetectors [72] have been shown.

Fig. 2.2 a) shows the cross-sections of an optical device fabricated using hybrid integration. A III-V based material is bonded onto a silicon photonic waveguide, which defines the position of the optical mode by its high index contrast. On top of the waveguide the active III-V material is unstructured to relax the alignment tolerances of the active photonic components typically structured by contact lithography. The light is largely guided in the silicon waveguide and has only a small modal overlap with the active III-V material. Lasers or optical amplifiers formed with this technology exhibit a

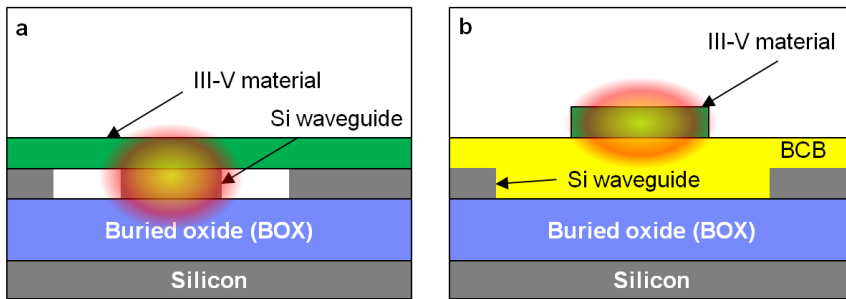


Figure 2.2: a) Cross-section of an optical device fabricated with hybrid integration [8]. b) Cross-section of an optical device fabricated using heterogeneous integration [9]. Note that the optical mode is mainly located in the III-V in contrast to the optical mode in a).

low modal gain despite the excellent material properties and high material gain of the active III-V material. Consequently, the lasers demonstrated in this technology suffer from high threshold currents [8].

Heterogeneous Optical Integration The heterogeneous integration approach was developed to obtain a light source for silicon photonics and also other, potentially improved functionalities, such as an increased responsivity of photodetectors, for silicon photonics. In this technology, active optical devices can be fabricated for the sake of light emission similar to hybrid integration. The difference compared to hybrid integration is the material in which the light is guided. Using heterogeneous integration the light may be guided entirely in the active III-V material as shown in Fig. 2.2 b) by using a bonding layer that enables to tune the coupling between the active III-V material and the passive silicon waveguide circuitry. Also here, a die comprising an epitaxial layer stack is bonded face-down on a pre-structured silicon photonics wafer or carrier, but on top of an intermediate bonding layer. Within the heterogeneous integration approach two different bonding approaches are known: The bonding can be either performed by using an organic adhesive such as BCB [73], or by molecular bonding by using the Van-der-Waals forces of a planarized silicon dioxide surface [13]. Although molecular bonding has superior thermal properties due to the higher thermal conductivity of silicon dioxide, this bonding approach requires very smooth surfaces prepared by CMP and is very sensitive to particles that can compromise yield. In contrast, adhesive bonding does

not require planarization and is therefore easier to process. A variety of devices, such as lasers [9], photo detectors [74], and modulators [50] have been shown using heterogeneous integration.

The silicon photonic waveguides are arranged such that the light is coupled into the III-V, where the active function is performed (e.g., lasing), and then subsequently coupled back into the waveguide by evanescent coupling. The additional degree of freedom to tailor the coupling in heterogeneous integration, however, comes at the expense of alignment issues during the fabrication of active III-V components. For a given coupling thickness, i.e. the thickness of the material between the silicon waveguide and the active III-V material, only a limited offset can be tolerated to achieve the desired coupling. This is in contrast to hybrid integration, where the silicon waveguide determines the position of the optical mode.

Optical integration technology used in this thesis The main advantage of heterogeneous integration over hybrid integration is that optical devices benefit from a large modal overlap with the active material as shown in Fig. 2.2b). This results in medium output power levels and low threshold currents for lasers [9] meeting the requirement for low-power on-chip light sources. This heterogeneous integration approach with adhesive bonding was used throughout the thesis because of these aforementioned advantages. The following sections describe the design flow, the passive SOI waveguide circuitry and the fabrication process used in this thesis.

2.3 Design flow used in this thesis

The photonic devices and circuits were designed using the Python-based freeware design toolkit IPKISS developed by Ghent University / IMEC [75]. The toolkit supports parametrized design of graphic data system II (GDSII) files with various GDSII layers. Both the passive silicon photonics circuitry as well as the active InP-based devices have been designed with the toolkit. The design of the passive silicon photonic waveguide circuitry and the active InP components was performed simultaneously to assure that a consistent design in which the III-V layers are accurately aligned to the silicon features. After DRC, the silicon layers were taped out for the silicon fabrication and the InP-layers were used to generate a photo lithography mask for further processing.

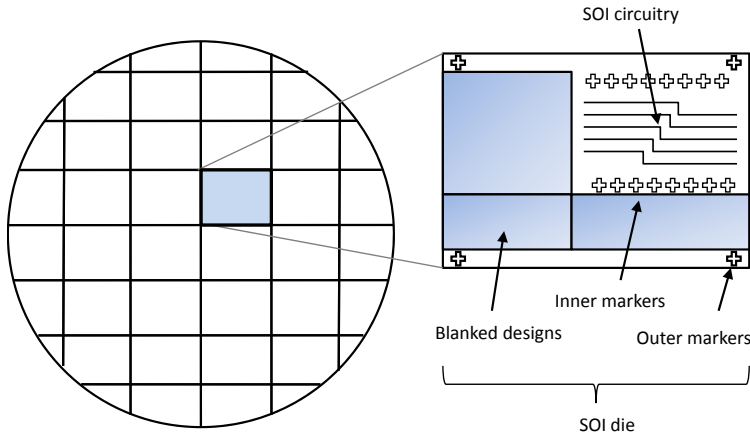


Figure 2.3: Wafer and die layout of the SOI MPW wafer run.

2.4 SOI waveguide circuitry

The processing of the SOI waveguides was carried out in the framework of the Epixfab [31], either at IMEC (Belgium) or LETI (France) in a 90 nm CMOS line adapted for the fabrication of optical components with low propagation by the absence of electronics requiring highly doped regions [31]. The process is based on 8 inch SOI wafers with a 220 nm thick top silicon device layer and a 2 μm thick buried silicon dioxide. Each fabrication run was carried out as a MPW shuttle run where designs from several industrial and academic partners are composed and processed at once. After fully processing the wafers, the die areas of the other partners were blanked by laser ablation and were sent out to the individual partners for measurement, or further processing by the partners as in this case.

Fig. 2.3 displays the layout of an 8 inch MPW with a schematic of the die. Each die has a size of about $12 \times 15 \text{ mm}^2$ (varying from run to run) with about $5 \times 6 \text{ mm}^2$ user area. Each die has metrology sections on the outer sides for measuring optical performance figures (waveguide loss, etc.) and alignment markers. These *outer* markers were used during the SOI fabrication to align the masks for full and partial etching of the top silicon with respect to each other, and were then re-used during the fabrication of the active InP devices as will be discussed in detail in the fabrication section 2.6.

Within the user area the silicon photonic waveguides and grating cou-

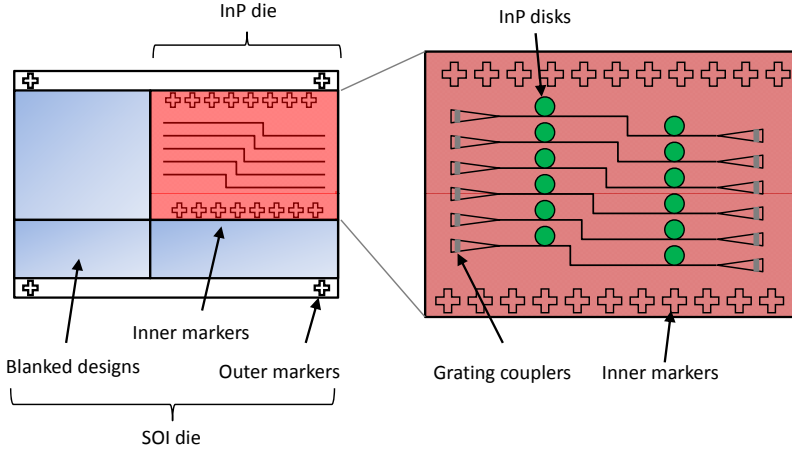


Figure 2.4: Layout of the SOI die with the bonded InP die on top. The InP microdisks, which are structured later, are shown to indicate their later positioning with respect to the SOI waveguides.

plers are located, into which light can be coupled in and out vertically. The user area also contains inner marker blocks, which are used to align the subsequent InP fabrication steps with respect to the first InP lithography step defining the position of the active disks and rings, respectively.

The grating couplers used in this work were the standard grating couplers enclosed in the design tutorial [33]. They consist of a partially etched grating coupler attached to a $250\ \mu\text{m}$ long parabolic taper that laterally converts the mode of the grating coupler with a width of approximately $10\ \mu\text{m}$ down to the silicon waveguide width of $500\ \text{nm}$. The silicon ridges were partially etched with an etch depth of $70\ \text{nm}$ and a period of $630\ \text{nm}$. The couplers were centred around $1550\ \text{nm}$ and were designed to operate at a coupling angle of 8° from the surface normal [33]. The peak efficiency of the grating couplers was found to be between -6 and $-8\ \text{dB}$, varying from SOI fabrication run to run. These grating couplers were used as standard means for the optical measurement performed throughout this thesis. In the work presented here, measurements were partially limited by the grating couplers because of their limited bandwidth, low efficiency, and large Fabry-Perot ripples caused by residual end-facet back-reflection. The performance of the grating couplers for evaluation of on-chip optical devices was improved as discussed in Chapter 8.

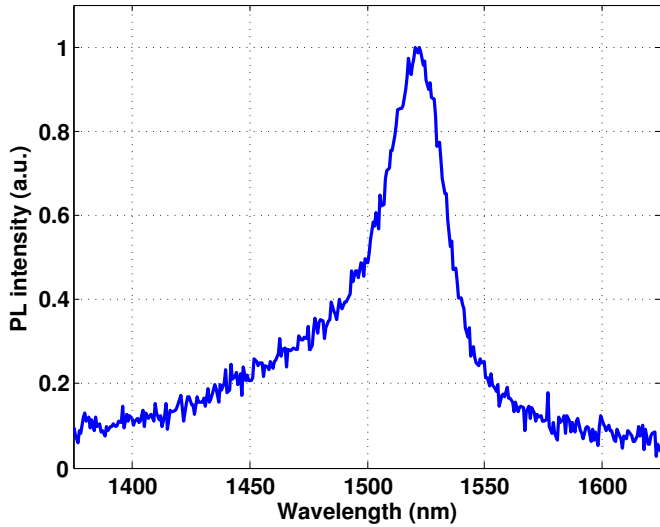


Figure 2.5: Photoluminescence spectrum recorded on a sample having the epitaxial layer stack as stated in Tab. 2.1. The PL spectrum is a courtesy of P. Regreny (INL Lyon).

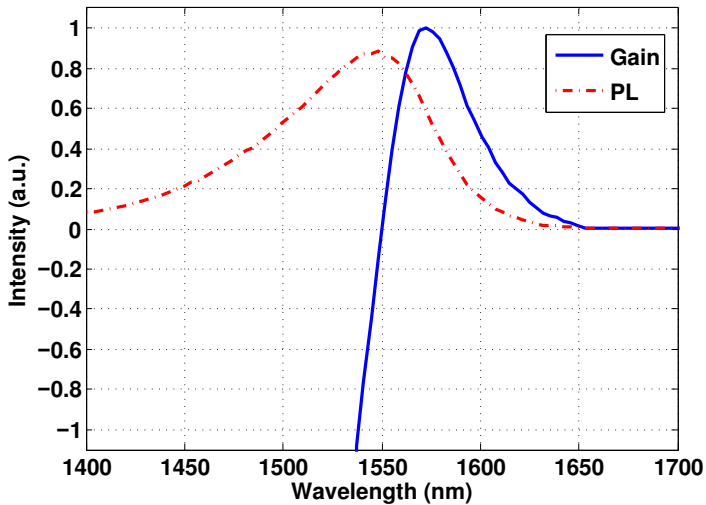


Figure 2.6: Approximated spectral gain response according to J. Pikrek - Optoelectronic Devices: Advanced Simulation and Analysis, Chapter 5 [10]

| Number | Layer | Material | Doping (cm^{-3}) | Thickness (nm) |
|--------|-----------------|----------------|---|-------------------|
| 1 | Top contact | InP | $n+, 1 \times 10^{18} - 5 \times 10^{18}$ | 80 |
| 2 | Tunnel junction | Q1.3 (InGaAsP) | $n++, 1 \times 10^{19}$ | 10 |
| 3 | Tunnel junction | Q1.3 (InGaAsP) | $p++, 2 \times 10^{19}$ | 10 |
| 4 | Doped barrier | InP | $p, 5 \times 10^{17} - 1 \times 10^{18}$ | 135 |
| 5 | Barrier | Q1.2 (InGaAsP) | nid | 25 |
| 6 | QW barrier | Q1.2 (InGaAsP) | nid | 15 ($\times 3$) |
| 7 | Quantum well | InAsP | nid | 6 ($\times 3$) |
| 8 | Barrier | Q1.2 (InGaAsP) | nid | 25 |
| 9 | Doped barrier | Q1.2 (InGaAsP) | $n, 1 \times 10^{18}$ | 120 |
| 10 | Bottom contact | InP | $n++, 5 \times 10^{18}$ | 95 |

Table 2.1: Epitaxial layer stack of the lasing material used in this work. The epitaxial stack comprises three InAsP quantum wells and a tunnel junction to enable a single metallization step [12]. The total thickness of the layer stack is 583 nm [13].

2.5 Laser material

The epitaxial material used for the active InP microdisk fabrication was obtained from the Ecole Centrale Lyon, L’Institut des Nanotechnologies de Lyon (INL) [13]. On an InP wafer a multiple quantum well (MQW) structure was grown by molecular beam epitaxy as shown in Table 2.1. The stack comprises three strained indium arsenide phosphide (InAsP) quantum wells embedded in a quaternary barrier with a band-gap of 1.2 eV. To prevent absorption of the highly-doped p-contact a tunnel junction with a total p-doped thickness of only 10 nm was included in the epitaxial layer stack [12]. The low absorption results from the small modal overlap of the lasing mode with the thin highly p-doped region. The working principle of a tunnel junction is that degenerately, i.e. highly, doped n and p-regions have an overlap of the Fermi-levels, which in combination with an abrupt interface with distances typically smaller than a few nanometers allows electrons from the n-side energetically located near the conduction band to directly tunnel into energy levels located near the valence band of the p-side [76]. This way low-resistance junctions can be formed enabling that a sole metallization step can be employed to contact both sides of the InP laser diode. The contact layers are made from highly n-doped InP as shown in Tab. 2.1.

The PL spectrum shown in Fig. 2.5 was measured at room-temperature and had a PL maximum at around 1520 nm lending the device to lasing operation at around 1550 nm. The shape of the gain can be computed by the convolution of the density of states (DOS) with the band structure

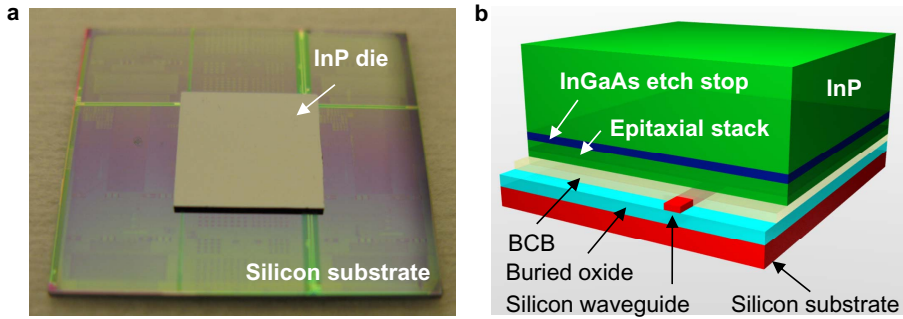


Figure 2.7: After bonding the InP die with quantum well on a silicon photonics chip. a) Photograph is a courtesy of S. Keyvaninia (Ghent University). b) Schematic view at this fabrication stage. The full layer stack including the InP substrate, the etch stop layer and the epitaxial layer stack bonded onto the SOI chip is visible.

[10]. Fig. 2.6 schematically show the calculated approximate gain from a PL spectrum centred around 1550 nm. The inherent red-shift of the modal gain is due to the bandgap shrinkage or bandgap renormalisation effect [77]. The bandgap of a semiconductor laser is reduced by Coulomb scattering of electrons and holes, and by the binding energy of the excitons formed in the semiconductor [77]. The effect may be partially compensated for high pumping currents [78]. For the given PL spectrum the gain has the maximum around 1570 nm corresponding to a red-shift of about 20 nm. This is in good agreement with the measured PL-to-lasing-emission shift of about 30 nm measured during the experiments discussed in Chapter 3.

2.6 InP microdisk fabrication

This section describes the fabrication of electrically contacted InP microdisks starting from a pre-fabricated SOI waveguide circuit and a 2 inch InP wafer with an epitaxial layer stack for an electrically driven MQW laser on top of it.

Bonding An InP die having about the same size as the SOI user area was cleaved out of the epitaxial wafer and was bonded on top of the SOI chip. Within this work, the bonding was performed by P. Mechet and S. Keyvaninia (Gent University / IMEC), who are gratefully acknowledged.

Adhesive bonding using BCB was performed to attach an InP die including the epitaxial layer stack to the silicon chip. First, both the SOI substrate and the III-V die cleaved out of an epitaxial InP wafer were cleaned. Then, the BCB polymer was spun onto the SOI substrate. By baking the substrate at 150 °C for 10 minutes the solvent of the BCB was evaporated. The III-V dies were then placed face-down on top of the user area of the SOI substrate as shown in Fig. 2.4.

Initial fabrication runs resorted to a manual bonding approach, where the InP was placed and pressed manually onto the adhesive layer. This resulted in non-uniform BCB layers with air inclusions and compromised bonding yield. The issue of non-uniformity becomes apparent after substrate removal when processing the epitaxial layer stack in vacuum tools to form the InP microdisks as will be shown below. Fig. 2.8 d) shows a photograph of a de-laminated bonding layer.

In the last fabrication runs the samples were fabricated by machine-bonding according to the recipe given in [79] instead of manual bonding. The samples again were placed manually on the BCB film, but were then mounted on a fixture and loaded into the bonding tool. The fixture was heated under a defined pressure to 280 °C for 1 hour in an inert atmosphere. Finally, the samples were cooled down at a defined rate [79] and unloaded. A photograph of the bonded sample with the InP die on top of the silicon photonics carrier is shown in Fig. 2.7 a). The schematic view after completing this fabrication step is shown in Fig. 2.7 b). Machine bonding supports also the bonding of several InP dies simultaneously on one large SOI substrate. After bonding, the substrate can then either be cleaved to separate the dies, or the InP substrate can be removed at first from the bonded quantum-well structure before cleaving.

InP substrate removal The epitaxial layer stack comprises the InP substrate, onto which an indium gallium arsenide (InGaAs) etch stop layer and later on the laser stack were epitaxially grown. When bonding an InP die with the layer stack face-down on the SOI chip, the laser stack is in close contact with the BCB, while the InP substrate is exposed to the surface and ready for removal. Within this thesis two substrate removal approaches were pursued.

The initial substrate removal process was using a CMP step followed by wet-chemical substrate removal. It was found that the CMP grains result in

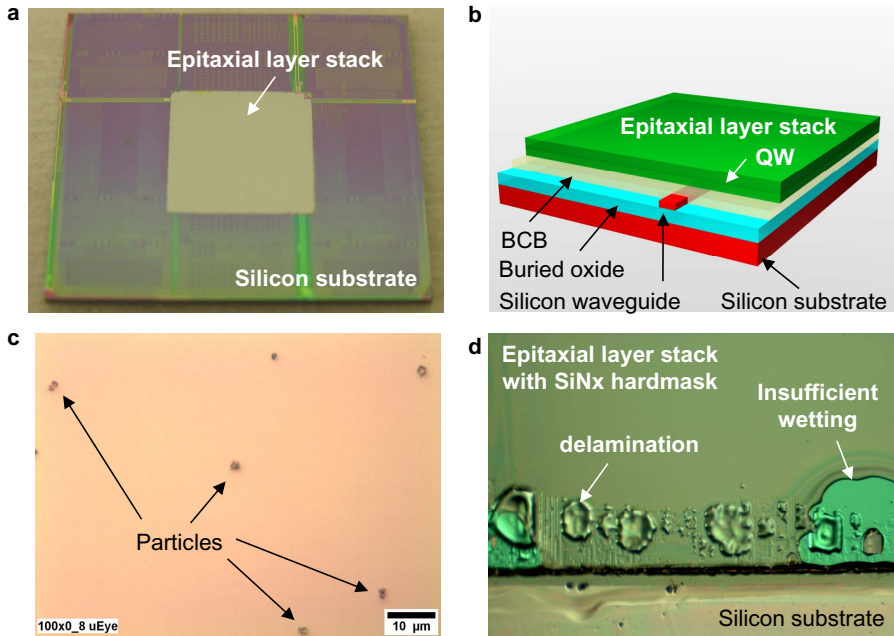


Figure 2.8: InP substrate removal and fabrication issues. a) Photograph of the epitaxial layer stack, which remains on the silicon substrate after bonding, and removing the InP substrate and the etch stop layer. The image is a courtesy of S. Keyvaninia (Ghent University). b) Schematic view at this fabrication stage. The remaining epitaxial layer stack including the quantum well is visible. c) Residual particles after substrate removal using CMP. d) Delamination and compromised photoresist wetting properties of a manually bonded sample. Image is a courtesy of O. Raz (TU Eindhoven).

a substantial amount of particles as shown in Fig. 2.8 c) that are acting as an etch mask in the InP dry etching step during the disk or ring definition. After the disk patterning by dry etching the formed InP spikes are standing upright and are then metallized during the successive metallization steps, resulting in short circuits between the bottom contact and the top contact metallization.

The later fabrication runs made use of the wet etch selectivity of hydrochloric acid (HCl) of InGaAs over InP. Using this approach the substrate can be easily removed wet-chemically resulting in an excellent bonding layer quality as shown in Fig 2.8 a). Therefore, during the later fabrication runs we used the purely wet-chemical substrate removal approach.

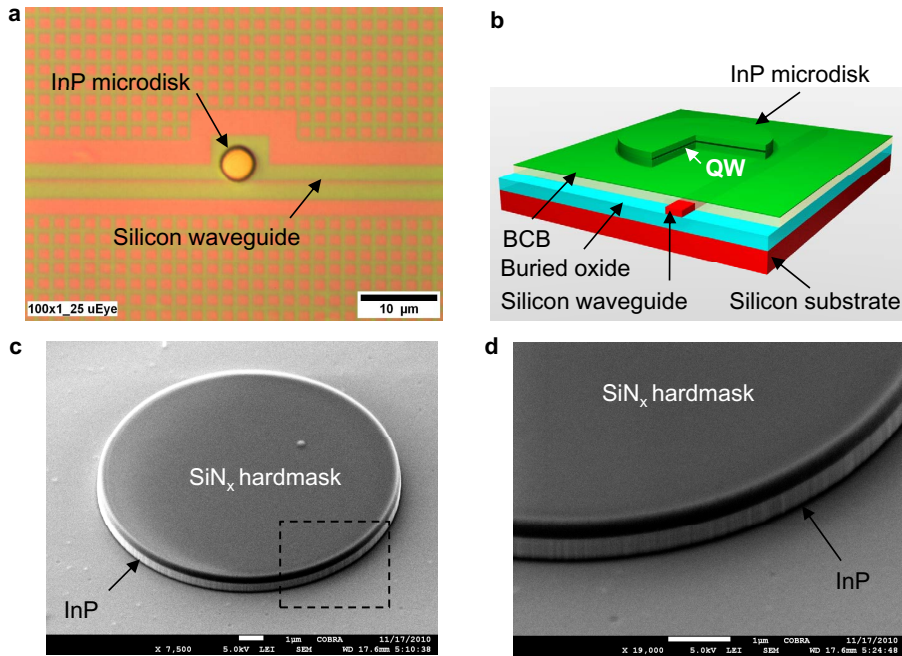


Figure 2.9: a) Optical microscope image after structuring a microdisk with $5\ \mu\text{m}$ diameter. b) Schematic view at this fabrication stage. c) SEM image of a microdisk with $10\ \mu\text{m}$ diameter. d) Close-up view on the smooth sidewall of the InP cavity underneath the silicon nitride hardmask. SEM images are a courtesy of T. De Vries (TU Eindhoven).

Disk definition The definition of the disks is achieved using a hard mask. Two types of hardmasks have been investigated: silicon dioxide (SiO_2) and silicon nitride (Si_3N_4), both deposited by inductively-coupled plasma (ICP)-plasma-enhanced chemical vapour deposition (PECVD). During this process step the samples are exposed to vacuum. Air inclusions within the bonding layer expand and lead to delamination of the membrane and compromised photoresist wetting properties as shown in Fig. 2.8 d) for a manually bonded sample. For machine bonded samples this vacuum-induced delamination was not observed.

After surface treatment of the hardmask to promote adhesion, a photoresist was spun and structured by optical contact lithography using the outer alignment markers in the SOI substrate as shown in Fig. 2.4. Then, the hardmask was structured dry-chemically using reactive ion etching

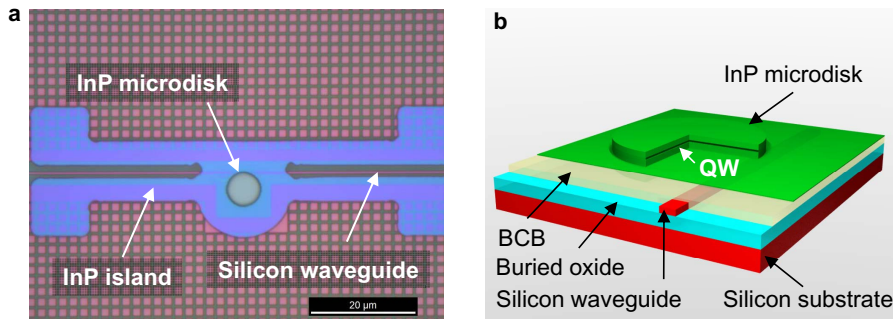


Figure 2.10: The footprint of the InP microdisk device becomes apparent after the island definition. a) Optical microscope image. b) Schematic view at this stage of fabrication.

(RIE). Several gas mixtures with varying ratios of CHF_3 and oxygen (O_2) have been investigated for both dielectrics and it was found that a silicon nitride hardmask etched with a flow rate of 10 % oxygen in CHF_3 resulted in a smooth sidewall profile, a good selectivity with respect to the photo resist and a strongly reduced polymer-re-deposition (*scumming*) tendency compared to etch recipes without lower oxygen ratios.

After structuring of the hardmask, the InP disks including ternary and quaternary material layers were etched dry-chemically by ICP-RIE. The process was operated near room-temperature with a well-established double-etch process using alternating cycles of methane-hydrogen and oxygen chemistry [80]. The epitaxial layer stack had a total thickness of 583 nm. To form the disk or ring cavities only about 508 nm have been etched to obtain simultaneously a good optical confinement and a high electrical conductivity of the remaining highly n-doped island layer. The control of the thickness was obtained by timed etching and subsequent correction of the etch depth after measurement with a profilometer. Fig. 2.9 a) shows an optical microscope image of the etched InP microdisk located on top of an SOI waveguide. A schematic view at this state of the fabrication is shown in Fig. 2.9 b). SEM images of an InP microdisk with a silicon nitride (SiN_x) hardmask are displayed in Figs. 2.9 c) and d).

Island definition After the definition of the disks and rings the islands were defined to form isolated regions preventing possible electrical connections between adjacent devices and also to prevent waveguide losses by

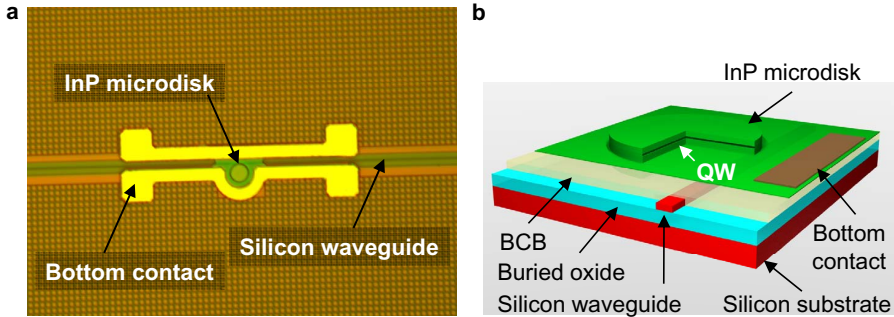


Figure 2.11: a) The bottom metal is formed to minimise the resistance of the devices. A clearance around the InP microdisk was maintained to not introduce absorption as shown in this microscope image. b) Schematic view at this stage of fabrication.

absorption. The islands consist of an ideally 75 nm thick highly n-doped InP layer and forms the bottom contact of the device extending to either side for connection to the ground (GND)-pads in later processing steps. To fabricate the islands a thick positive photoresist was spin-coated and structured using contact lithography. Then, the islands were patterned dry-chemically using the same etch recipe as for the disk definition. Fig. 2.10 shows an optical microscope image and a schematic view after completing this fabrication step. Note that the islands do not cover the waveguides to prevent absorption losses.

Bottom contact metallization A bottom contact metallization was performed to minimise the resistance of the only about 75 nm thick n-doped InP island layer. Using optical lithography, a negative tone photoresist with a thickness of about 750 nm was used that allows for metallization using the lift-off technique. A metal stack with a total thickness of 300 nm containing Ti as adhesion layer, Pt as diffusion barrier and Au as conduction layer has been deposited in an electron-gun evaporator. The device is displayed in Fig. 2.11 after completing the lift-off. During this process step it was critical that the bottom contact metal leads did not overlap with the waveguide to reduce metal absorption losses.

Cladding The first generation of InP microdisks and microrings were fabricated with a polyimide cladding. This material benefits from its planariza-

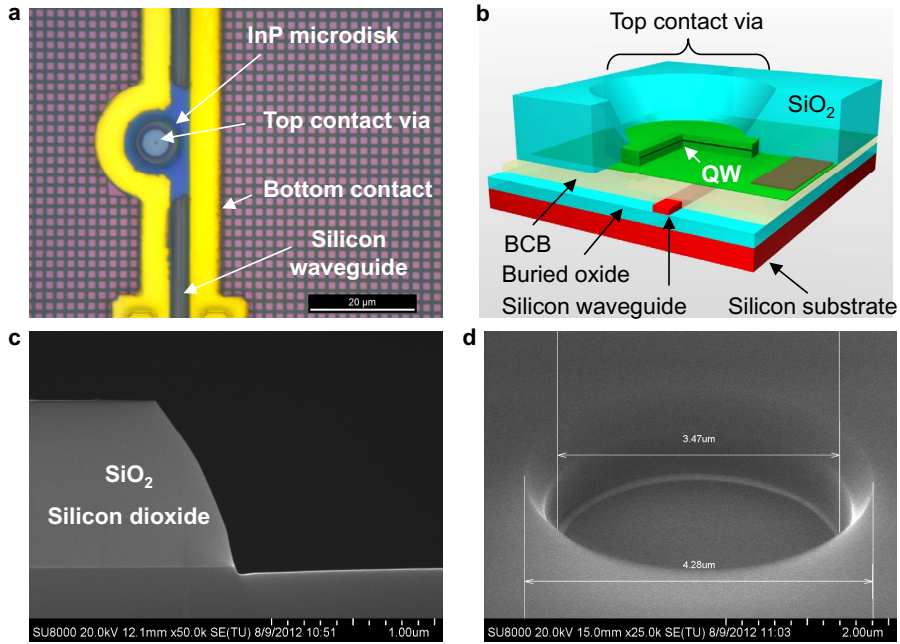


Figure 2.12: a) Optical microscope image after opening the top contact via. b) Schematic view after completing this fabrication step. c) SEM image of the slanted silicon dioxide sidewall, which is required for metallization using evaporation. d) SEM image of a silicon dioxide via with 3.5 μm diameter.

tion properties that ease the successive fabrication steps. The drawbacks of this material are a poor thermal conductivity and a slow process due to the long required baking times. Therefore, the later generations of InP microdisks were fabricated with a silicon dioxide cladding applied by ICP-PECVD. Compared to BCB silicon dioxide has a four times higher thermal conductivity of 1.3 to 1.4 $\frac{W}{mK}$ [81] compared to 0.29 $\frac{W}{mK}$ of cured BCB [82]. The thermally conducting cladding acts as a lateral heat-spreader, which significantly improves the thermal properties of the device as shown in section 3.3.1.

Via opening The via opening was initially performed with a negative tone photoresist and dry etching using RIE. Whereas this method was very convenient to process, it was found in due course of the project that the feature size control of the vias was difficult. This process step was identified

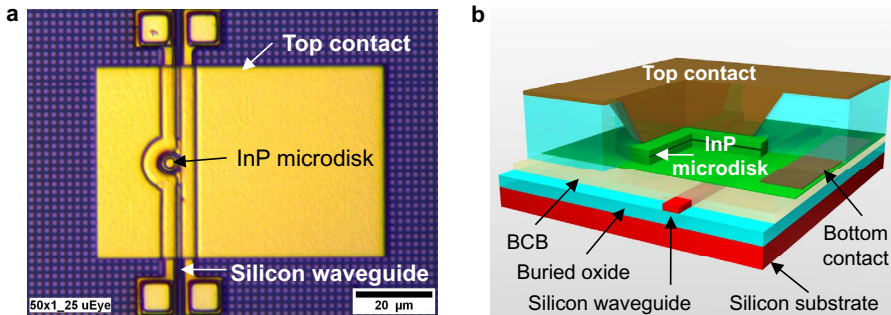


Figure 2.13: a) Optical microscope image after top contact metallization. b) Schematic view after completing this fabrication step.

to be critical because it has direct influence on the optical mode and the quality factor of the microdisk/-ring as will be discussed in Chapter 8. During the last fabrication run an image reversal lithography process was used showing excellent feature size control. Figs. 2.12 a) and b) show an InP microdisk device after completing the oxide via opening. For the subsequent metallization using evaporation it was crucial to obtain slanted oxide sidewalls, which were required to enable the metal to cover the sides of the via and to form a homogeneous metal contact. Fig. 2.12 c) shows a SEM image of the cross-section of such a slanted sidewall of a silicon dioxide via. A close-up SEM image of a $3.5 \mu\text{m}$ via in silicon dioxide is shown in Fig. 2.12 d).

Top contact metallization After the via opening for both top and bottom contact, the metallization for the top contact was applied using lift-off. The applied metal stack had a total thickness of 300 nm and comprises a titanium layer for adhesion, a platinum diffusion barrier and a gold layer for the actual conductivity. In principle, the top contact metallization step could also be combined with the successive pad metallization because both contacts are n-type in the epitaxial material used throughout the thesis. However, the mask layout was designed to also allow for other epitaxial layer stacks without a tunnel junction and containing both n- and p-type contacts.

Pad metallization The pad metallization again was applied by lift-off. A 750 nm thick negative-tone photoresist was used to enable the deposition

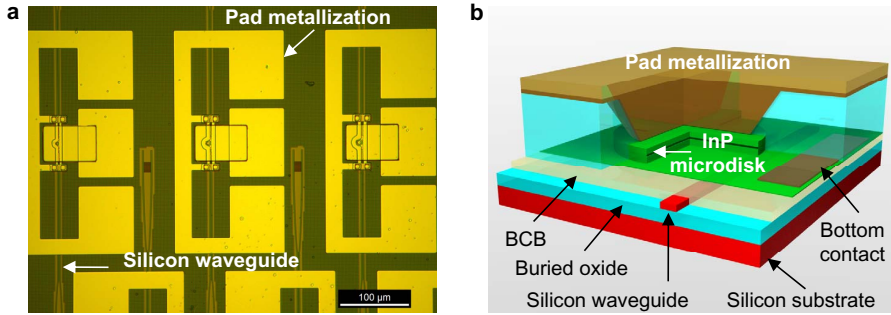


Figure 2.14: a) Optical microscope image after pad metallization. b) Schematic view after completing this fabrication step.

of a 300 nm thick metal layer stack. We used a metal stack containing a titanium adhesion layer and a gold layer for providing good conductivity for electrical measurements. After the pad metallization the devices were complete from an electrical stand-point. However, to improve the thermal properties of the device, an additional layer was added in the last fabrication run.

Pad reinforcement For reinforcing the pads an additional thick metal layer was deposited onto a bilayer-photos resist exhibiting a large undercut. By exposing and subsequently developing the photosensitive upper resist layer the underlying non-sensitive photoresist is over-developed generating a large undercut. Then, a thick layer larger than 500 nm of gold was deposited using sputtering, which required the described bilayer-resist to allow for a reliable lift-off.

The purpose of the additional thick metal layer is two-fold: On one hand it improved the mechanical stability for wire bonding and electrical probing. On the other hand it also improves the heat-sinking of the device because the thick metal layer acts as heat-spreader to efficiently remove heat generated in the device under forward bias. By effectively heat-sinking devices of similar size, it was shown that the small-signal bandwidth could be increased significantly [83].

2.7 Discussion

The present chapter gave an overview about the most promising technologies in photonic integration and positioned the work in this field. The heterogeneous integration technology used in this thesis and the corresponding design methodology were discussed. Then, the fabrication of the InP microdisks was described highlighting some of the special features of the processing flow and improvements over state-of-the-art in heterogeneous integration. The fabrication process is partially similar to first reports of the fabrication of InP microdisks in 2007 [9]. A key difference is that no molecular, but BCB bonding is employed. The fabrication process was set up at TU Eindhoven using the available expertise and processing modules in the cleanroom, such as InP ICP-RIE dry etching and polyimide cladding. Improvements in the fabrication of the active on-chip optical components compared with this initial fabrication process were made in following aspects:

- Purely wet-chemical substrate removal process drastically reducing the amount of particles compared to CMP-based substrate removal techniques.
- Silicon dioxide cladding instead of polyimide or BCB cladding results in a three-fold improved thermal conductivity.
- Accurate size control of the top via opening using an image reversal lithography process.
- A physical pad reinforcement metallization process alleviating the need for wet-chemical plating.

3 InP Microdisk Lasers

The present chapter describes the application of InP microdisks as lasers. After giving an introduction a time-dependent single-mode one-dimensional (1D) laser rate equation model is given. Then the static solutions of this model are presented and an implementation scheme is sketched. Then, an adapted model supporting multiple longitudinal and spectral modes is described that allows to simulate both bi-stable operation of InP microdisks, as well as the application of these devices as wavelength converters. Static and dynamic measurements of InP microdisk lasers are then shown. A parameter extraction scheme is presented enabling the identification of performance limiting components by employing a small-signal equivalent circuit (SSEC). Finally, performance limitations of InP microdisk lasers are discussed. Parts of this chapter were published in several scientific publications^{1,2,3}.

3.1 Laser integration approaches for silicon photonics

Silicon photonics is one of the most promising technology platform for photonic integration. However, the realization of monolithic light sources is hampered by the indirect band-gap of silicon preventing efficient light emission. Also, silicon suffers from Auger recombination and free-carrier absorption (FCA) exceeding the material gain of silicon [47].

Several approaches have been studied to overcome these indirect band-gap related issues. Quantum structures have been investigated, such as silicon nanocrystals and nanopillars, which allow to overcome the traditional phonon-selection rules and allow for more efficient radiative recombination [84, 85]. Although promising results at low temperatures have been reported, a room-temperature laser based on this approach remains to be demonstrated.

¹J. Hofrichter *et al.*, A fast and comprehensive microdisc laser model applied to all-optical wavelength conversion, *Integrated Photonics Research, Silicon and Nano Photonics (IPR), Photonics in Switching (PS), Monterey (CA), USA, 2010*, PTuA2 (2010).

²J. Hofrichter *et al.*, Digital all-optical signal processing using microdisc lasers, *Integrated Photonics Research, Silicon and Nano Photonics (IPR), Photonics in Switching (PS), Monterey (CA), USA, 2010*, PTuA3 (2010).

³J. Hofrichter *et al.*, All-optical wavelength conversion using mode switching in an InP microdisc laser, *Electronics Letters* **47**(16), pp. 927-929, (2011).

Raman lasers Another concept makes use of coherent phonon scattering in semiconductor lattices, known as the Raman effect. Silicon is a very attractive material for lasers based on this principle because of its perfect crystalline quality allowing for long-range phonons in the lattice. These long-range photons enable an efficient Raman scattering process, which is required to obtain a net gain in the material. By pumping at a given laser wavelength Raman-Stokes photons are emitted, which are shifted in wavelength. Lasers based on such an operation principle benefit from a high spectral purity and a high side-mode suppression ratio even outperforming state-of-the-art compound semiconductor diode lasers [86, 87]. On-chip integration is hampered by the lack of an electrical pumping scheme due to the nature of the light-generating process, as well as the need for high bias voltages to remove free carriers in the resonator sections generated by absorption. Also, the Raman-scattering-based photon emission has a low efficiency making this technology unattractive from a power budget point-of-view.

Lattice-matched direct growth Approaches are also pursued to growth lattice-matched materials on silicon, e.g., direct band-gap III-V alloys, such as GaNAsP [88]. Whereas such an approach allows for electrical pumping the laser emission has a limited efficiency and the operation wavelength does not match the wavelength range in which silicon is transparent [89]. Despite the lattice mismatch, it was demonstrated that Ge can be grown epitaxially on silicon to form lasers operating at room-temperature. After the demonstration of an optically pumped laser in 2010 [90], also an electrically pumped Ge-on-Si laser has been shown recently [70]. The emission process is based on the population of a side-valley of the electronic band structure and the use of high doping concentrations resulting in a low material gain and a very low efficiency of the presented lasers.

Hybrid evanescent lasers The most promising approaches for on-chip optical lasers sources resort to the integration of III-V materials on silicon as discussed in section 2.2. Using hybrid integration, where a III-V gain material is molecularly bonded on top of a silicon waveguide, several promising results on lasers have been shown including Fabry-Perot lasers [91], distributed feed-back (DFB) lasers [92, 93] and microring lasers [94]. The output power reported is larger than 0 dBm (1 mW) and thus well

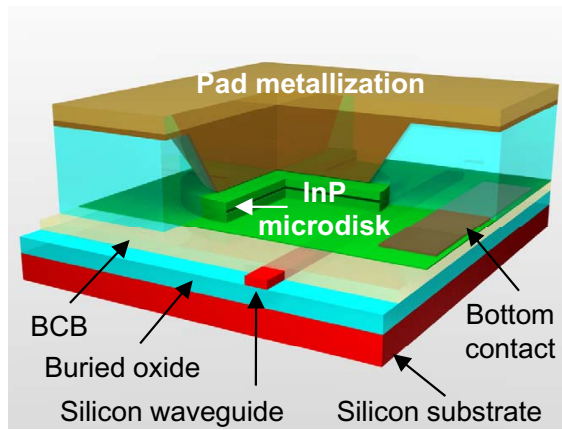


Figure 3.1: Cross-section through an InP microdisk laser heterogeneously integrated on a SOI waveguide. Note that on resonance the optical mode is entirely coupled from the silicon waveguide to the InP microdisk.

suitable for high-speed communication applications. All these aforementioned lasers suffer from the small modal overlap of the optical mode with the silicon waveguide resulting in small modal gain and large threshold currents despite the excellent material quality [8].

Heterogeneously integrated lasers Heterogeneous integration is another approach in which active III-V material is integrated on top of a pre-structured silicon photonic circuit. Instead of hybrid integration, where the III-V material is directly bonded on top of the silicon, heterogeneous integration uses an intermediate bonding layer. To overcome the issue of large threshold currents it is necessary to transfer the mode from the silicon waveguide entirely into the active III-V material. As the intermediate layer, either a polymer, such as BCB, or a silicon dioxide layer is used as the bonding layer between the active III-V device and the silicon waveguide. This way, the coupling can be tailored and device performance can be optimized. Using this technology various lasers have been shown, such as Fabry-Perot lasers [95] and InP microdisk lasers [9]. Fig. 3.1 shows a MDL heterogeneously integrated on a silicon waveguide. The device is electrically contacted allowing for electrical pumping and is evanescently coupled to the SOI waveguide into which the light is emitted.

Heterogeneously integrated microdisk lasers InP microdisk lasers are an interesting candidate for on-chip laser sources [96, 97], all-optical wavelength converters [98] and also all-optical memories [51, 99] due to their compactness and low power consumption. They are also regarded as a viable candidate for all-optical signal processing and photonic switching applications. Within a MDL, several longitudinal optical modes compete. Due to the free spectral range of the cavity and the broad gain spectrum of the MQW gain material, typically several longitudinal lasing modes with azimuthal order M are present in the cavity as shown in Fig. 3.2 a). Each lasing mode normally propagates in clock-wise (CW) and counter-clock-wise (CCW) direction, unless the device operates in the bi-stable regime as will be discussed in Chapter 4 in detail.

3.2 Modelling InP microdisk lasers

This section models InP microdisk lasers by rate equations, the optical properties of the cavity and the coupling between waveguide and microdisk. First, a basic analysis of the device properties of InP MDLs was performed to gain an elementary insight into the device behaviour and the device properties. Therefore, a single-mode 1D laser rate equation model as proposed by Van Campenhout [100] has been implemented and used for numerical investigations. Then, a more sophisticated multimodal model was developed to investigate longitudinal mode competition as the underlying physical principle of the wavelength conversion effect [53] and cross-gain suppression effects, which are the underlying principle for bi-stable operation of MDL-based optical flip-flops [51, 54].

3.2.1 A 1D radially dependent single-mode microdisk laser model

Time-dependent model The time-dependent single-mode laser model is a radially-dependent rate equation model. Because of angular symmetry the rate equations were analysed in cylindrical coordinates, i.e., the model does not account for angular components. This means, that in the investigations below the angular change of the carrier density $\frac{\partial N}{\partial \phi}$ and the photon density $\frac{\partial S}{\partial \phi}$ are zero. Also, a height-dependent change of the internal quantities N and S is neglected assuming only radially dependent, vertical fundamental modes. The assumption is justified as the modes with the largest quality factors, which are of interest for lasing operation, are

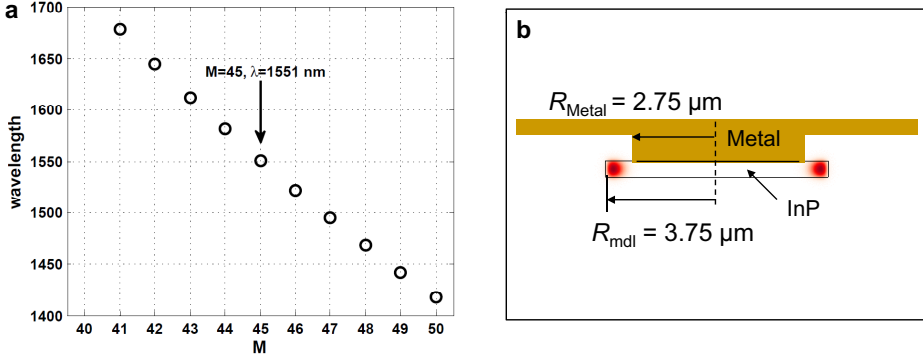


Figure 3.2: a) Lasing wavelengths of the fundamental lasing mode in an InP microdisk laser with $7.5 \mu\text{m}$ diameter. b) Cross-section and field distribution simulated by 2D FDTD.

vertically fundamental modes, as the top and bottom contact of the device are highly-doped resulting in absorption of vertical higher order modes. Furthermore, the vertical fundamental modes have larger overlap with the quantum well material, and thus a higher modal gain.

The electrical field distribution of the optical mode $\Psi(r)$ is modelled as a normalized Bessel function of the first kind J_ν , where ν is the azimuthal order of the corresponding lasing mode. By using Maxwell's equations it is clear that also a field component is existing outside of the disk cavity, which would be modelled by Hankel-functions [101]. However, their field component outside of the disk cavity is negligible, justifying the simplification to account for the field components inside the disk such that the electrical field component in radial direction $E_r(r=R)$ at the perimeter of the disk can be set to zero, which is achieved by normalizing the bessel function J_ν to the first Bessel zero z_0 such that the field distribution becomes $J_\nu\left(\frac{r}{z_0}\right)$ and the electrical field becomes zero at the perimeter of the cavity. The electrical field distribution J_ν is shown in Fig. 3.3 for several optical modes with azimuthal order $\nu = M = 40$. The modal distribution was normalized such that $\int_0^R \Psi^2(r)rdr = 1$.

Equation (1) gives the radially dependent carrier density in cylindrical coordinates. Note that the equations used in this model do not cover angular dependency. In equation (1) g refers to the spatially dependent gain, v_g is the group velocity of the optical mode. R is the radius of the

MDL cavity and S describes the photon density of the lasing mode. In this model it is assumed that the laser operates at a single longitudinal and radial mode. The recombination processes were modelled by the Shockley-Read-Hall (SRH) recombination coefficient A , the radiative recombination coefficient B , and the Auger coefficient C , which are material parameters and not spatially dependent. Furthermore, also the diffusion of charge carriers was modelled by the diffusion coefficient D . The last term in equation (1) holds the electrical pumping of the device with η_v being the vertical injection efficiency and $J(r)$ being the spatially dependent electrical pumping current density. The total thickness of the MQWs is given by t_a and q is the elementary charge. The photon density S was modelled as a lumped photon density and obtains its spatial dependence via the normalized electrical field distribution $\Psi(r)$. The overlap factor of the optical mode with the quantum well region is Γ .

$$\begin{aligned} \frac{\partial N(r)}{\partial t} = & -g(N(r), S) \cdot v_g \cdot \Psi^2(r) \cdot \Gamma \cdot \pi \cdot R^2 \cdot S \\ & - (AN(r) + BN^2(r) + CN^3(r)) \\ & + D \left(\frac{\partial N(r)}{r \partial r} + \frac{\partial^2 N(r)}{\partial r^2} \right) + \frac{\eta_v J(r)}{qt_a} \end{aligned} \quad (1)$$

The photon density S is defined by equation (2) wherein τ_p is the photon lifetime and β is the spontaneous recombination coefficient for coherent coupling to the lasing mode.

$$\begin{aligned} \frac{\partial S}{\partial t} = & -\frac{S}{\tau_p} + \beta \int_0^R B \cdot N^2(r) \cdot \Psi^2(r) \cdot 2\pi r dr \\ & + S\Gamma \int_0^R g(N(r), S) \cdot v_g \cdot \Psi^2(r) \cdot 2\pi r dr \end{aligned} \quad (2)$$

The active region of the MDLs consists of quantum wells, whose gain g is exponentially dependent on the local carrier density $N(r)$ with respect to the transparency density N_0 :

$$g(N(r), S) = g(S) \cdot \ln \frac{N(r)}{N_0} \quad (3)$$

For a given total photon density S the gain is lowered due to spectral hole burning, spacial hole burning and other effects. So the gain $g(r)$ can be reduced to [14]:

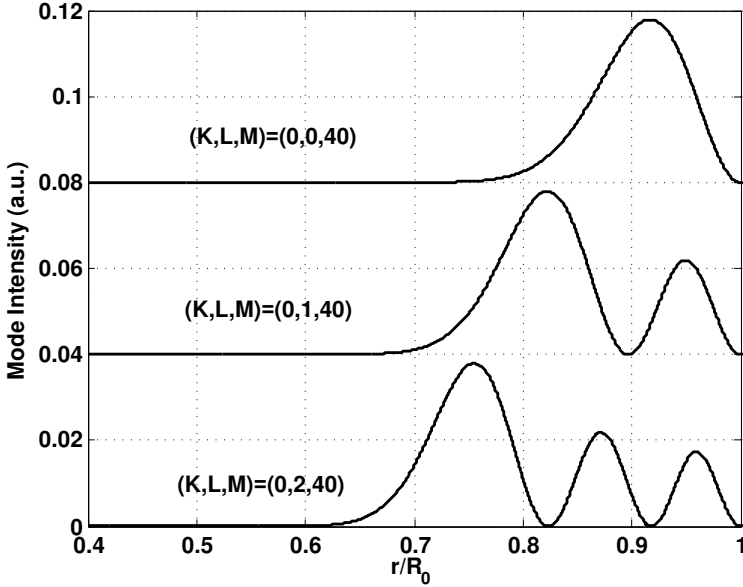


Figure 3.3: Different radial optical modes in a microdisk laser.

$$g(N(r), S) = G_0 \Gamma \cdot (1 - \epsilon_s S) \cdot \ln \frac{N(r)}{N_0} \quad (4)$$

with G_0 being the material gain. The effects are all included in the gain-suppression factor ϵ_s , which reduces the gain for the photon density ΓS in the active region of the MQWs. To save computational time by avoiding divisions the gain has been approximated as given in equation (5) for low gain suppression $\epsilon_s S \ll 1$:

$$\frac{1}{1 + \epsilon_s S} \approx 1 - \epsilon_s S \quad (5)$$

The parameters used for the modelling are given in Tab. 3.1 and are either related to the device geometry, are taken from literature values [9, 14, 81, 102, 103], or are obtained by measurements [15].

The described model allows to compute the internal quantities of the device, such as local gain, electron density and photon density, which are inaccessible by measurements. Fig. 3.4 displays the temporal response of the radially dependent charge carrier density when applying a current

| Parameter | Symbol | Value |
|--------------------------------------|--------------|--|
| Device radius | R | $3.75 \mu\text{m}$ |
| Material gain | G_0 | 1500 cm^{-1} |
| Threshold carrier density | N_0 | $1.5 \cdot 10^{18} \text{ cm}^{-3}$ |
| Self-gain suppression factor | ϵ_s | $2.0 \cdot 10^{-17} \text{ cm}^3$ |
| Cross-gain suppression factor | ϵ_c | $4.0 \cdot 10^{-17} \text{ cm}^3$ |
| Internal coupling factor | k_{int} | $1.5 \cdot 10^8 \text{ s}^{-1}$ |
| External coupling factor | k_{ext} | $8.8 \cdot 10^{10} \text{ s}^{-1}$ |
| Group velocity | v_g | $8.8 \cdot 10^9 \text{ cm} \cdot \text{s}^{-1}$ |
| Operation wavelength | λ_0 | 1550 nm |
| One particle recombination factor | A | $1.0 \cdot 10^{-8} \text{ s}^{-1}$ |
| Bimolecular recombination factor | B | $2.0 \cdot 10^{-10} \text{ cm}^3 \text{ s}^{-1}$ |
| Auger recombination factor | C | $1.6 \cdot 10^{-28} \text{ cm}^6 \text{ s}^{-1}$ |
| Diffusion factor | D | $8 \text{ cm}^2 \text{ s}^{-1}$ |
| Spontaneous emission coupling factor | β | $1.0 \cdot 10^{-3}$ |
| Current injection factor | η | 0.27 |
| Operation current | I | 3.5 mA |
| Gain curvature parameter | a | $1.3 \cdot 10^{13} \text{ cm}^{-3}$ |
| Thickness of MQWs | t_a | 18 nm |

Table 3.1: Parameters used in the radially depended microdisk laser models. The values are taken from literature [9, 14], measured [15] or based on the device geometry.

of 2.5 mA with a step function at $t=0$. The relaxation oscillations, i.e., the balancing oscillations between electron- and photon density towards equilibrium, are clearly visible. After applying a current step function the charge density is increased resulting in a large gain. The optical gain in turn emits a large amount of photons visible as an overshoot of the output power. By emitting photons the electron density is reduced lowering the gain. This in turn reduces the output power and the electron density increases again until a steady-state equilibrium between electron density and photon density, i.e., output power, is reached. The period of the relaxation oscillation largely defines the intrinsic speed of the device for a given bias current.

Stationary case The model presented so far allows for the computation of the temporal response of the laser quantities. However, the computational effort in solving the coupled differential rate equations may be too large to compute the static response of the device for a given bias point. Typically, the model mentioned above requires a computation time of 10-20

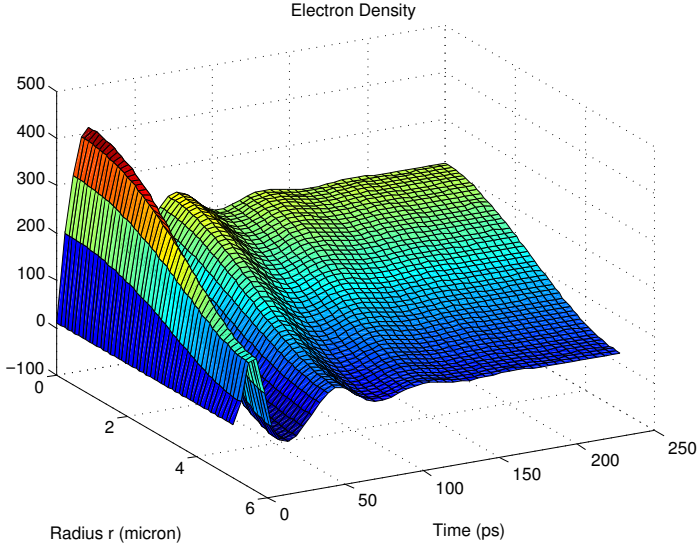


Figure 3.4: Temporal response of the electron density in a microdisk laser when applying a current step of 2.5 mA at $t=0$. The relaxation oscillations as temporal fluctuations of the electron density are visible.

minutes on a desktop PC until it converges when applying a step current function. Hence it is attractive to implement a model, which allows to rapidly compute the static solution of the rate equations above.

In the stationary case the external bias current is constant, i.e. the temporal change of the bias current is zero $\frac{\partial I}{\partial t} = 0$. Consequently, after some settling time, the temporal change of the spatially-dependent charge carrier density $N(r)$ and total photon density S become zero as given in equations (6) and (7).

$$\begin{aligned}
 0 = & -G(N(r), S) \cdot v_g \cdot \Psi^2(r) \cdot \Gamma \cdot \pi \cdot R^2 \cdot S(r) \\
 & - (AN(r) + BN^2(r) + CN^3(r)) \\
 & + D \left(\frac{\partial N(r)}{r \partial r} + \frac{\partial^2 N(r)}{\partial r^2} \right) + \frac{\eta_v J(r)}{qt_a} \quad ,
 \end{aligned} \tag{6}$$

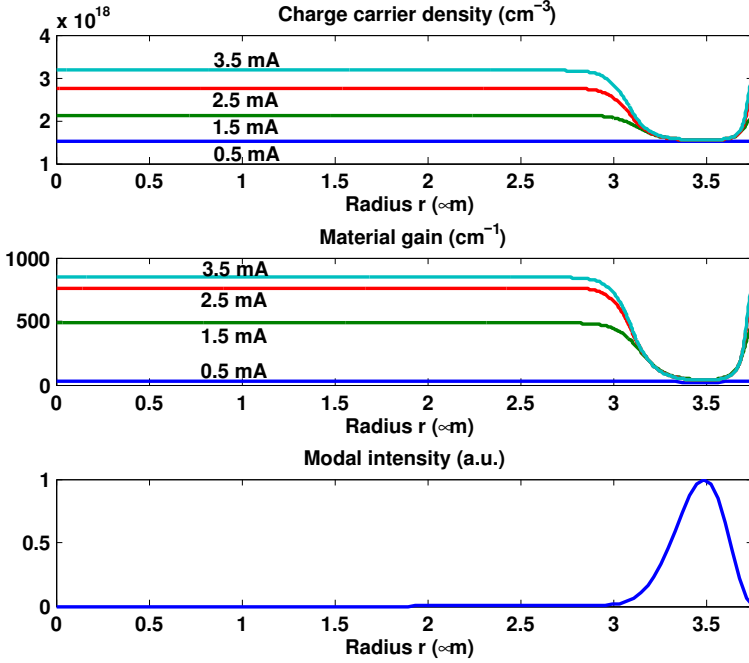


Figure 3.5: Internal quantities of an InP microdisk laser: charge carrier density, material gain and modal intensity (from top to bottom).

$$\begin{aligned}
 0 = & -\frac{S}{\tau_p} + \beta \int_0^R B N^2(r) \cdot \Psi^2(r) \cdot 2\pi r dr \\
 & + S\Gamma \int_0^R G(N(r), S) \cdot v_g \Psi^2(r) \cdot 2\pi r dr \quad .
 \end{aligned} \tag{7}$$

To solve the differential equation system given in equations (6) and (7), boundary conditions are needed to obtain a unique solution. In MDLs, the spatial change of the charge carrier density $\frac{\partial N(r)}{\partial r}$ in the centre $N(r=0)$ is zero due to radial symmetry. At the perimeter, the electron density $N(r=R)$ is clamped by the surface recombination. Hence the boundary conditions, which are given as first derivative in r , resemble *Neumann*-boundary conditions given in equations (8) and (9) with v_s being the surface recombination velocity.

$$\frac{\partial N}{\partial r} \Big|_{r=0} = 0 \quad (8)$$

$$\frac{\partial N}{\partial r} \Big|_{r=R} = N(R) \cdot \frac{v_s}{D} \quad (9)$$

An algorithm to solve the resulting boundary-value problem of the ordinary differential equations in r as given in equations (6) and (7) was implemented in MATLAB using the freely available toolkit `bvp4c` [104]. The algorithm solves these equations in only a few seconds on a desktop computer and can be used in a loop to calculate the output power P_{out} with respect to the bias current I .

Output power The total optical output power is evenly split between the CW and the CCW propagating optical modes in the cavity. The coupling constant between disk and waveguide is α_c and the active volume is $V = \pi R^2 t_a$. The resulting output power in one waveguide is defined in equation (10) with E_{ph} being the photon energy at the given wavelength of the lasing mode.

$$P = 0.5 \cdot \pi R^2 t_a E_{ph} v_g \alpha_c S \quad (10)$$

The static single-mode model presented here will be used in chapter 8 to investigate and predict ultimate device performance figures of InP microdisk lasers.

3.2.2 A 1D radially dependent multi-mode microdisk laser model

The single-mode microdisk laser model presented before in section 3.2.1 can be used to describe the general behaviour of a laser for a single lasing mode. Such an approximation is correct for high SMSRs where only one dominant laser peak is present. However, in a real microdisk laser several lasing modes are present because the free-spectral range (FSR) of the devices is typically smaller than the gain bandwidth of the quantum well laser material resulting in a limited side-mode suppression ratio.

In addition, when biasing the laser high above threshold the device may operate in a bi-stable regime where the dominant lasing mode propagates either in the CW or CCW direction and suppresses the counter-propagating

lasing mode. It is worth noting that in this case not only other longitudinal modes are suppressed but also the counter-propagating lasing mode at the same wavelength. All these effects cannot be accurately rendered by a single-mode model. Therefore a more complex multi-mode model was implemented. This model may be used to model wavelength conversion effects by injecting external light in side-modes, and also to model optical bi-stability in microdisk-laser based optical flip-flops.

Time-dependent model for multiple modes To accurately simulate the switching behavior of a MDL for switching and wavelength conversion applications, we implemented a multi-mode 1D laser rate equation model. We expanded the model suggested by Van Campenhout et al. [100] for self- and cross-gain suppression with the corresponding factors ϵ_S and ϵ_C [102, 103, 105]. A parabolic gain curve $g(\lambda) = G_0(1 - a(\lambda - \lambda_0)^2)$ was assumed to account for the non-uniform gain spectrum [106].

A microdisk laser has several longitudinal modes lasing and competing for gain, which can be exploited for wavelength conversion [53]. Also, each mode lases in CW and CCW direction simultaneously. When the device is biased high above threshold and the cavity has smooth sidewalls resulting in low scattering, the device can operate in the bi-stable regime. In this regime either the CW or CCW is dominant and suppresses the other counter-propagating lasing mode. Using the described effect an optical flip-flop can be realized [51, 54]. A model has been implemented that comprises three longitudinal modes, each of which propagates in CW and CCW direction. The resulting differential equation for the photon densities in each of these modes is given in equation (11), wherein τ_p is the photon lifetime, β is the spontaneous recombination coefficient for coherent coupling to the lasing mode and S_{in} is the injected external field in the respective direction. The external injection coupling factor k_{ext} models the coherent external injection of light into the respective lasing mode [102, 103]. The internal coupling between the CW and the CCW propagating lasing direction is modelled by κ_{int} [15], which accounts for, e.g., sidewall roughness and scattering.

$$\begin{aligned}
\frac{\partial S_{cw,ccw,i}}{\partial t} = & -\frac{S_{cw,ccw,i}}{\tau_p} + S_{cw,ccw,i} \Gamma v_g 2\pi \int_0^R g_{cw,ccw,i}(r) \cdot \Psi^2(r) \cdot r \cdot dr \\
& + 2\pi\beta \int_0^R B n^2(r) \cdot \Psi^2(r) \cdot r \cdot dr \\
& + \kappa_{ext} \sqrt{S_{in,cw,ccw,i} S_{cw,ccw,i}} + \kappa_{int} S_{cw,ccw,i}
\end{aligned} \tag{11}$$

Each photon density experiences a decay time constant τ_p due to, e.g., scattering or absorption. The build-up of the mode is achieved by stimulated emission with the modal gain $g_{cw,ccw,i}$ in the active region, whose overlap with the mode is Γ . Also spontaneous emission with the factor B is coupled into the lasing mode with the spontaneous emission coupling factor β . The respective gain for the multi-modal system is thus:

$$\begin{aligned}
g_{cw,ccw,i}(S_{cw}, S_{ccw}, n(r), r) = & G_0 [1 - a(\lambda_0 - \lambda_i)^2] \\
& \cdot \left(1 - \epsilon_s \sum_i S_{cw,ccw,i} - \epsilon_c \sum_i S_{ccw,cw,i} \right) \cdot \ln \left(\frac{n(r)}{N_0} \right)
\end{aligned} \tag{12}$$

The gain-suppression factors are ϵ_s for self-gain-suppression and ϵ_c for cross-gain-suppression. Due to the symmetric structure, the gain suppression coefficients are also assumed to be symmetrically. By analysing the standing and travelling wave patterns in resonant structures, such as disks or rings, by Maxwell-Bloch-equations it can be shown that the counter-propagating modes result locally in a two-fold magnitude of the electrical fields causing spacial hole-burning, and thus a two-fold cross-gain suppression factor $\epsilon_c = 2\epsilon_s$ [107, 108]. Note, that the equations for the gain suppression only hold for weak gain-suppression $\epsilon S \ll 1$ as mentioned in section 3.2.1. Introducing equation (12) into equation (11) yields the spatio-temporal dependent differential equation for the charge carrier density for the multi-modal case:

$$\begin{aligned}
\frac{\partial N(r)}{\partial t} = & - \left(\sum_i g_{cw,i}(r) S_{cw,i} + \sum_i g_{ccw,i}(r) S_{ccw} \right) \cdot v_g \cdot \Psi^2(r) \cdot \Gamma \cdot \pi \cdot R^2 \\
& - (AN(r) + BN^2(r) + CN^3(r)) \\
& + D \left(\frac{\partial N(r)}{r \partial r} + \frac{\partial^2 N(r)}{\partial r^2} \right) + \frac{\eta_v I(r)}{\pi R^2 q t_a}
\end{aligned} \tag{13}$$

Besides stimulated emission into the respective lasing modes, also charge carrier recombination is taken into account by the coefficients A, B and C for Shockley-Read-Hall (SRH) recombination, spontaneous emission and Auger recombination, respectively. Regions with depleted carrier concentrations due to stimulated emission in the region of the mode (spatial hole-burning) are refilled by diffusion of charge carriers with the diffusion constant D . The diffusion term holds the expression for cylindrical coordinates. The electrical pumping current I flowing through the disk area πR^2 generates charge carriers in the active region, whose thickness is t_a . The model's radial dependency enables the simulation of spatial hole-burning which limits output power, modal recovery and thus the device speed.

The multi-modal laser model presented here is used to model bi-stable MDL-based all-optical flip-flops and their switching properties in Chapter 4. It is also employed in Chapter 5 to simulate wavelength conversion effects in InP microdisk lasers.

3.3 Measurements of InP microdisk lasers

The measurement apparatus used in this work has a temperature-controlled 6 inch substrate holder and custom-made fibre-holders to couple light vertically or near-vertically into the chip or wafer as shown in Fig. 3.6. The available parameter analyzer enables low direct-current (dc) parametric measurements down to currents as low as 10 fA. The electrical high-speed radio-frequency (RF) measurement equipment allows to measure large-signal data integrity by means of bit-error rates up to 12.5 Gb/s. Small-signal measurements can be performed up to a bandwidth of 33 GHz (electrical-electrical, optical-electrical, electrical-optical and optical-optical bandwidth) using a vector network analyzer (VNA) and commercial 40 Gb/s telecommunication equipment, such as a 40 Gb/s lithium niobate

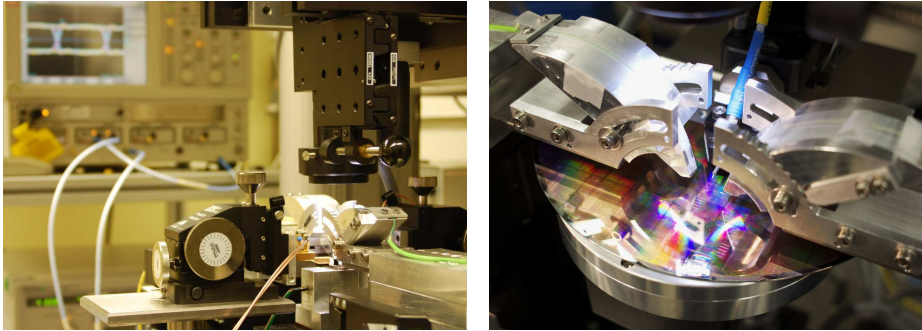


Figure 3.6: Photographs of the wafer-scale measurement apparatus used throughout the work. a) Overview and b) close-up view of the measurement apparatus.

(LiNbO₃) modulator and a 43 Gb/s photoreceiver connected with 46 GHz electrical cables, and 44 GHz RF-probes for connecting on-chip devices.

The fibre alignment can be performed with fully automated 3-axis motorized stages with a resolution of 50 nm. Precise angular alignment of the fibres is guaranteed by computerized numerical control (CNC)-milled fibre holders as shown in Fig. 3.6. Optical signals can be generated at a wavelength span between 1480 and 1610 nm with a fibre-coupled power of 0 dBm (1 mW), which can be boosted to +13 dBm between 1535 and 1565 nm using C-band EDFAs.

For the majority of the experiments the setup available at IBM Research - Zurich has been used. The experiments on wavelength conversion have been performed at TU Eindhoven using similar infrastructure.

3.3.1 Static characteristics

Output power vs pumping current Under forward bias electrons and holes are injected into the MQWs of the InP microdisk, which recombine and emit light. Small currents as low as 2.5 mA are sufficient for more than 3 μ W fibre-coupled optical power as shown in Fig. 3.7. A certain threshold current is required to overcome the internal losses of the device. Whereas threshold currents in the order of 100 mA have been reported for lasers fabricated with hybrid integration [8], the devices investigated in this thesis have a very low threshold current of only 0.5 mA as shown in Fig. 3.7. The waveguide-coupled output power is about 6 dB larger than

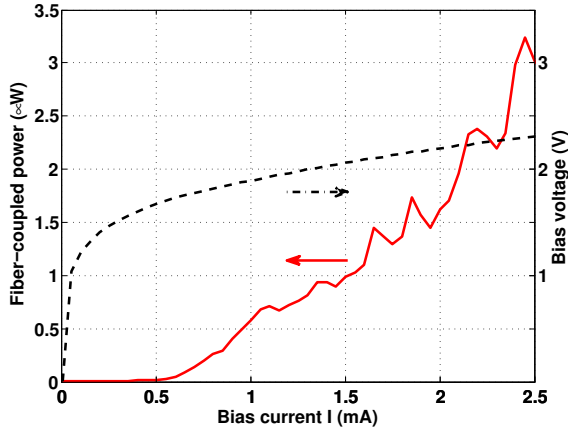


Figure 3.7: Static performance characteristics of an InP microdisk lasers. Left axis: Fibre-coupled output power; and right axis: Bias voltage vs. electrical bias current.

the fibre-coupled output power because of the relatively large fibre-to-chip coupling losses ranging between 6 dB to 12 dB depending on wavelength and sample quality. The electrical threshold voltage of these devices is around 1 V and is governed by the band-gap, which needs to be overcome for light emission. The onset of light emission corresponding to the threshold current is around 1.7 V. The slope of the bias voltage with bias current $\frac{\partial V}{\partial I} = R$ is the series resistance of the device. Typically for the measured lasers the series resistance is in the order of 180 Ω as will be discussed in detail in section 3.3.2 below.

Lasering spectrum and linewidth Because the cavity of the laser is a resonant structure, exhibiting resonances with a FSR smaller than the gain spectrum of the MQW, several lasing modes are supported. Depending on the bias conditions, a lasing mode at a smaller or larger FSR is dominant as shown in Fig. 3.8 b). For a bias current of 2.72 mA the lasing mode at 1560 nm is dominant. When increasing the bias current to 3.53 mA the lasing mode at 1592 nm becomes dominant.

The laser linewidth is shown in Fig. 3.8 b) and was fitted with a Lorentzian of 2 pm linewidth. The corresponding Lorentzian laser linewidth can be approximated according to [109] as in equation (14). The resolution bandwidth of the heterodyne optical spectrum analyzer (OSA) used in this

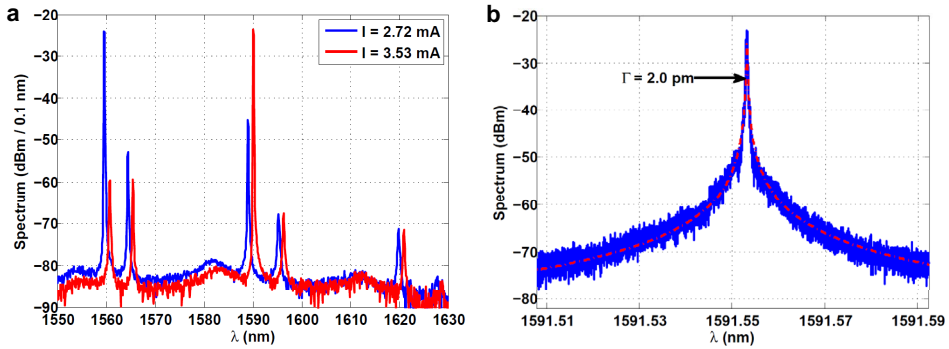


Figure 3.8: a) Lasing spectrum of a free-running microdisk laser. b) Lasing linewidth of the lasing mode around 1590 nm at 3.53 mA bias.

experiment was 0.08 pm.

$$\Delta f \approx \frac{c}{\lambda^2} \cdot \Delta \lambda \approx 237 \text{ MHz} \quad (14)$$

Compared to literature values a linewidth of 237 MHz is relatively large, which is partially due to the low finesse of the resonator because of the limited intrinsic Q of the resonator and the waveguide coupling. Microdisk lasers inherently have a large linewidth for small resonator diameters [110]. For resonators with similar cavity diameters linewidths in the range of 100 to 400 MHz have been reported [110]. As in any diode laser the laser linewidth could be further reduced by biasing the microdisks with a larger current resulting in a higher optical output power [111, 112], which for the given devices would require improved heat-sinking to prevent thermal roll-off, or by using larger resonators, potentially integrated in the silicon waveguide.

Furthermore, more sophisticated resonators can be used to reduce the laser linewidth. DFB lasers fabricated with the related hybrid integration method as described in section 2.2 were reported to have substantially smaller laser linewidths of only 7 MHz [92, 93].

Thermal properties The characteristic temperatures T_0 and T_1 are good measures to characterize the thermal properties of semiconductor lasers. The temperature T_0 describes the change of the threshold current with increasing temperature. The dependence of the threshold current on

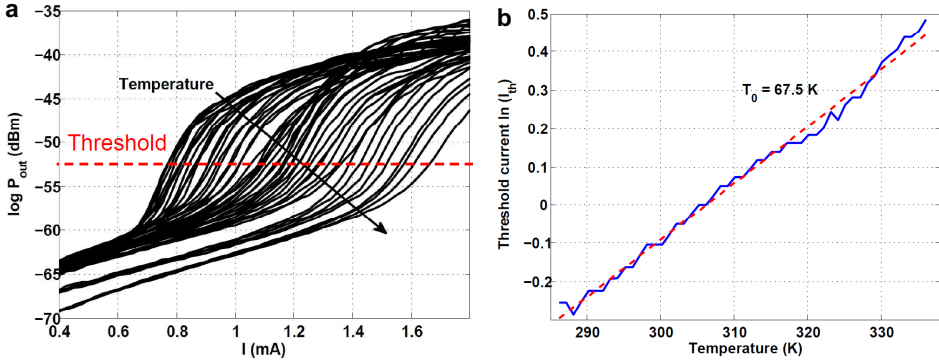


Figure 3.9: Threshold current extraction. a) Logarithmic plot of the output power vs. current for different temperatures. b) T_0 extraction: threshold current vs. temperature.

the temperature can be modelled as in equation (15).

$$I_{\text{th}} = I_{\text{th},0} \cdot \exp\left(\frac{T}{T_0}\right) \quad (15)$$

$$\ln(I_{\text{th}}) = \frac{1}{T_0} \cdot T + \ln(I_{\text{th},0}) \quad (16)$$

Fig. 3.9 a) shows the drift of the threshold current for increasing temperatures from 13°C to 63°C. When monitoring the shift of the threshold current at the position of the largest change in power as indicated in Fig. 3.9 the characteristic temperature T_0 can be extracted. The drift of the threshold current can be fitted with a linear equation according to equation (16) as shown in Fig. 3.9 b). For the lasers having a polyimide cladding as described in section 2.6 a characteristic temperature of 67.5 K was extracted, which is a typical value for quantum-well based semiconductor lasers.

In analogy, the characteristic temperature T_1 denoting the change in the slope efficiency $\frac{dP}{dI}$ with temperature can be extracted. For the device having a polymer cladding a T_1 of only 22 K was extracted clearly indicating temperature issues.

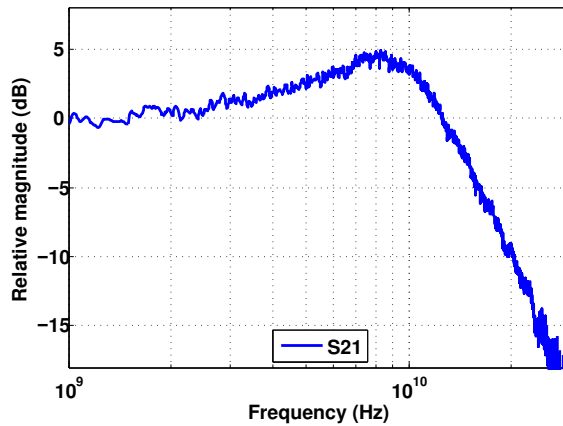


Figure 3.10: Small-signal bandwidth extraction: the transfer parameter S_{21} . The extracted bandwidth is 12 GHz. The S_{21} measurement data are a courtesy of O. Raz (TU Eindhoven).

3.3.2 Dynamic characteristics

A small-signal analysis was performed to investigate the speed limitations of directly modulated InP microdisk lasers. In contrast to a larger-signal analysis, where the device is modulated with the full swing, a small-signal analysis only investigates the device response on a small voltage oscillation around a given bias point. Performing this kind of small-signal analysis employing a small-signal equivalent circuit enables very accurate parameter extraction of the intrinsic device components and also of the parasitics. Such an analysis enables the identification of the components, which limit the device speed. Before the parameter extraction by analyzing the reflection coefficient S_{11} the transfer coefficient S_{21} was measured to acquire the actual speed of the device.

Transfer parameter S_{21} To extract the bandwidth of the optical light emitting components, the device is electrically biased at a static operation point. Note that the extracted bandwidth only holds for a specific bias point as it is bias-dependent. A small-signal modulation is applied around the central operation point by using a bias tee. Typical modulation values are -30 to -10 dBm (electrical power). The optical power is then recorded with a matched photo-receiver, whose bandwidth needs to be larger than the

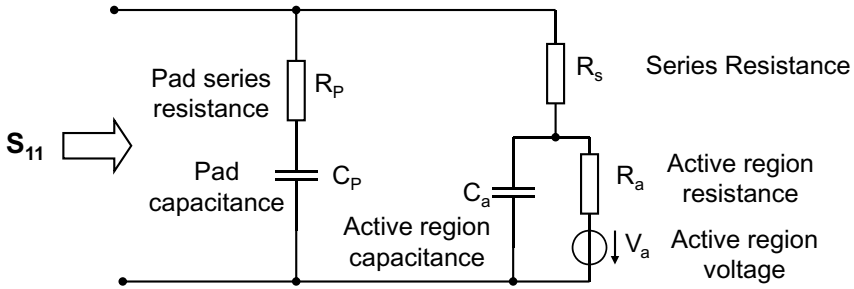


Figure 3.11: Small-signal equivalent circuit of an InP microdisk laser. The model is equivalent to SSEC used to model VCSELs [11].

device under test to allow for accurate normalization. In our experiments we used an electro-optical VNA with an EO-bandwidth of 67 GHz. Fig. 3.10 shows the modulation bandwidth of an InP microdisk laser with a diameter of $7.5 \mu\text{m}$ biased at 3.5 mA, which is a typical operation point. The bandwidth is 12 GHz, which enables data operation of 10 Gb/s and beyond. To operate the device at higher speed it can be biased with a higher drive current, which in turn reduces the output power due to thermal roll off requiring improved heat-sinking. Alternatively seeding can be employed to boost the device speed [98]. By using this method an initial photon population of the lasing mode is given and the device does not have to recover from spontaneous emission thus substantially improving the turn-on-speed.

Reflection coefficient S_{11} By measuring the complex reflection coefficient S_{11} the complex input impedance of an electronic device can be determined and the parasitic and intrinsic electrical components can be extracted. The parameter extraction was performed according to the scheme presented in [113], where the internal and external electrical components of a VCSEL were determined. The complex reflection factor A_{11} was measured and the complex load impedance Z_L was calculated according to equation (17) with Z_S being the source impedance of 50Ω .

$$S_{11} = \frac{Z_L - Z_S}{Z_L + Z_S} \quad (17)$$

The complex load impedance cannot be fitted to a simple RC-model. Instead, the computed complex load impedance Z_L was then fitted to a

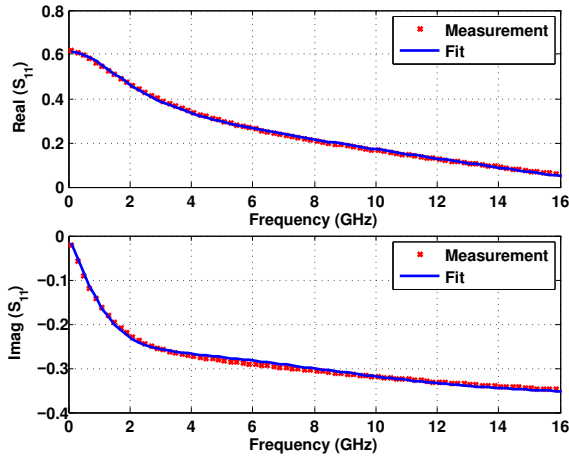


Figure 3.12: Small-signal measurements of InP microdisks. Real and imaginary part of the small-signal scattering parameter S_{11} , and the fit to the small-signal equivalent circuit given in Fig. 3.11.

small-signal equivalent circuits SSEC commonly used to describe VCSELs [11]. Although microdisks lasers have a different coupling mechanism to extract the optical power, and have a different order of the Bessel function describing the electrical field distribution in the cavity, the structure of a microdisk is equivalent to a VCSEL and therefore the same SSEC can be used to extract the parasitics. The used SSEC is shown in Fig. 3.11 and the individual components are indicated. The left hand side of the SSEC describes the pad parasitics consisting of the actual lumped pad capacitance C_p and a resistor R_p modelling pad losses at high speed. The right hand side of the SSEC shown in Fig. 3.11 describes the actual MDL components. The series resistance R_s describes all series resistances of the device including metal-semiconductor contact resistances the sheet resistance of the bottom contact and the resistance of the tunnel junction. The intrinsic device is determined by the capacitance of the active region C_a and the resistance of the active region R_a . The static dc bias voltage defining the point of operation is V_a .

The measured complex reflection coefficient S_{11} of a MDL with a diameter of $15 \mu\text{m}$ is shown in Fig. 3.12. Also, the computed complex reflection coefficient obtained from fitting the measured data to the SSEC is indicated showing excellent agreement and demonstrating that the VC-

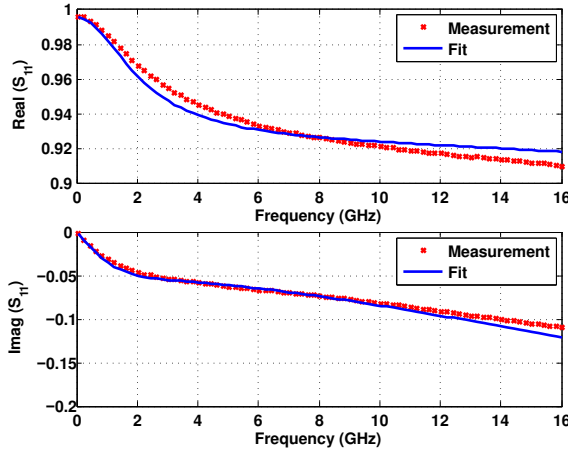


Figure 3.13: Small-signal measurements of the pads. Real and imaginary part of the small-signal scattering parameter S_{11} , and the fit to the small-signal equivalent circuit given in Fig. 3.14.

SEL SSEC can be employed for MDLs. The parameters of the pads were extracted to $R_p = 168.0 \Omega$ and $C_p = 310 \text{ fF}$. The components of the active device were $R_s = 26.6 \Omega$, $C_a = 153.1 \text{ fF}$ and $R_a = 181.8 \Omega$ at a bias current of 3.5 mA. By scaling the active area to a MDL with $7.5 \mu\text{m}$ diameter a capacitance as low as $C_a = 38.3 \text{ fF}$ was obtained. The larger resistance of the active region R_a of more than 180Ω introduces a severe speed limitation and should be reduced to improve the device speed. A detailed analysis on the influence of the individual components on the device speed is given in Chapter 8. Based on the extracted parasitics it became apparent that the device is largely mismatched resulting in strong back reflections reducing the modulation efficiency when driving the device from an electrical 50Ω system.

Pad and metal interconnect parasitics To investigate the influence on the total parasitics, the pads of one device were truncated using FIB etching to enable the extraction of the pad parasitics only. An optical microscope image of this device is shown in Fig. 3.14(top). The small-signal equivalent circuit, which was used for the fitting is shown in Fig. 3.14(bottom). The actual pad-to-ground capacitance is C_1 and C_0 is the fringing capacitance between adjacent pads. The residual conductivity of

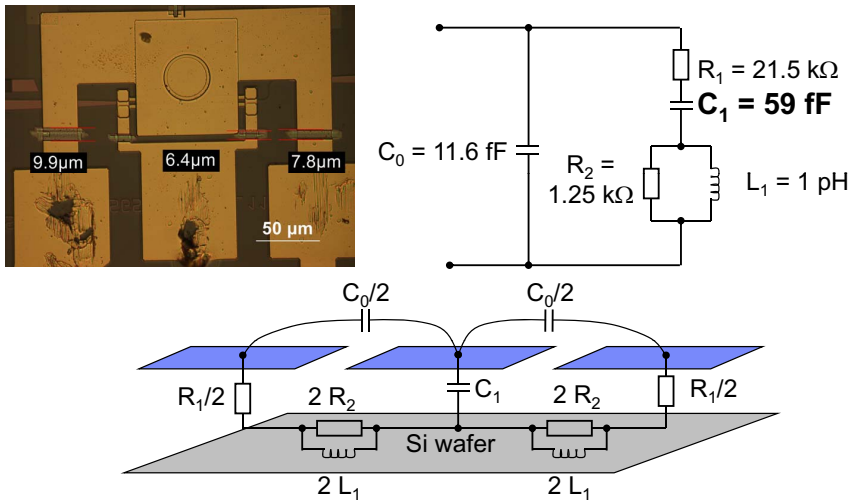


Figure 3.14: Parameter extraction of the pad parasitics. Top left: Microscope image of the truncated pads by FIB cut. The FIB cuts have been performed by A. Fuhrer (IBM Research - Zurich). Top right: Extracted small-signal equivalent circuit. The dominating pad-to-ground capacitance is $C_1 = 59$ fF. Bottom: Small-signal equivalent circuit of the pads.

the BCB adhesive and cladding was modelled as R_1 . The conductivity of the silicon substrate was modelled by the resistors R_2 and the inductors L_1 .

The extraction results of the pads are shown in Fig. 3.14 employing a more sophisticated SSEC to accurately model the behaviour of the pads at high speed. The actual pad-to-ground capacitance C_1 was extracted to 59 fF thus has a considerable influence on the device speed of small InP microdisks with diameters smaller than about $10 \mu\text{m}$. The fringe capacitance $C_0 = 11.6$ fF has a substantial smaller influence. A detailed analysis on the influence of the parasitics pad- and wiring capacitance C_p is given in Chapter 8. A reduction of the capacitance can be achieved by increasing the distance between the pads and ground, i.e., by increasing the cladding thickness. Alternatively, the permittivity of the cladding can be reduced by using polymers or low- k materials, which typically have a lower thermal conductivity, thus resulting in early thermal roll-off of the output power [83].

3.4 Discussion

The present chapter gave an overview of state-of-the-art lasers on silicon. A single-mode laser rate equation model was implemented and solved for static conditions to enable the rapid calculation of internal laser quantities and optical output power. A more sophisticated multi-modal laser model was presented and discussed.

Simulations on the optical properties of the microdisk cavities were performed showing that the positioning of the top contact as well as the waveguide with respect to the disk are crucial for yielding InP microdisk lasers capable of emitting high output power.

The static performance figures of microdisk lasers were reported and compared to other integrated laser approaches. The extracted thermal properties indicate thermal issues, which relate to the cladding material used.

Finally, the dynamic properties of InP microdisk lasers were shown, demonstrating the potential for operation at 10 Gb/s. A parameter extraction scheme enabling access to the intrinsic and parasitic components of MDLs was presented indicating that the device speed is limited by its parasitics, in particular the large resistance of the active region.

4 InP Microdisk Flip-Flops for All-Optical Logic

This chapter discussed the basic requirements of logic systems and special requirements for photonic systems. Then, the switching properties of InP microdisk laser based all-optical flip-flops are presented. Based on the multi-modal microdisk laser model developed in Chapter 3 ultimate switching performance figures are simulated and discussed with respect to the requirements of logic systems. Parts of the present chapter are based on deliverables submitted to the European Commission during the HISTORIC project and on several scientific publications^{4,5}.

4.1 Introduction

Logic systems typically consist of several building blocks (e.g., combinational logic, gates and sequential logic, such as flip-flop memory elements), each of which perform certain logic operations with a limited set of functionality. This chapter first describes the characteristics of all-optical flip-flops based on InP microdisk lasers. The switching properties are shown experimentally and compared to the spatially-dependent multi-modal microdisk laser model presented in Chapter 3. Then, ultimate performance figures of the switching process are estimated to extract an approximate minimum switching energy and an approximate upper limit for the switching speed.

The achieved results are then discussed in the light of the requirements for optical logic systems. To concatenate several identical logic blocks, independent of whether their working principle is electronic or optical, they must fulfil certain requirements, which are discussed below. The chapter is then summarized and remaining challenges towards all-optical digital systems are discussed.

4.2 Switching properties of all-optical InP microdisk flip-flops

Lasers supporting multiple modes may exhibit bi-stable behaviour [102]. Bi-stability is induced by the cross-gain suppression of the lasing modes

⁴J. Hofrichter *et al.*, Digital all-optical signal processing using microdisc lasers, *Integrated Photonics Research, Silicon and Nano Photonics (IPR), Photonics in Switching (PS)*, 2010, PTuA3 (2010).

⁵J. Hofrichter *et al.*, Specifications for All-Optical Flip-Flops, Gates and Digital Photonics, *HISTORIC Deliverable D1.2*, (2010).

competing for gain. Bi-stability was observed in semiconductor ring lasers, in which the counter-propagating modes are suppressing each-other [99]. Also, InP-based microdisk lasers show bi-stability of the counter-propagating modes [51]. This effect may be used to form bi-stable optical memory elements, which are called *flip-flops* in analogy to their electrical counter parts.

When electrically pumping a ring- or disk-laser-based optical flip-flop the laser emission in either CW or CCW direction becomes dominant. The initial lasing direction is determined by numerous factors, such as the external coupling properties to the external waveguide, imperfections of the cavity shape, carrier density fluctuations, etc. By injecting external light pulses into the silicon waveguide they are coupled into the device provided they are on one of the resonance wavelengths of the device. The injected photon density of the suppressed mode may then be amplified in the laser. When injecting a sufficiently large amount of photons over-compensating the photon density of the initial lasing mode, the state of operation may be reverted. The remainder of this section discusses the dynamics of InP microdisk-laser-based all-optical flip-flops.

To investigate these devices, the multi-modal temporal model developed in Chapter 3 was applied to calculate the dynamic behavior of the switching process [51, 54]. Experiments and simulations were carried out in which the devices were driven with a constant electrical dc and external light pulses were injected to determine the switching speed and minimal required optical pulse energy for switching. Optical pulses with an estimated switching energy of 1.8 fJ having a duration of 100 ps and a power of 18 μW were injected into the waveguide in both the experiment and the simulations to investigate the switching behaviour of the counter-propagating modes. Details on the experiment can be found in [51].

The curves for the rising edge of the CW mode in the experiment and the simulations are shown in Fig. 4.1 a). In the experiment, the injection pulse in the waveguide cannot be separated from the MDL output lasing power. However, the simulations provide insight into these modal dynamics and reveal a slight overshoot of the lasing mode. Also the emitted power level can be related to the injection power level in the waveguide. With the parameters and bias conditions given in Table 3.1, the MDL emits 71 μW and can be switched with only 18 μW leading to a fan-out of $F = \frac{P_{\text{MDL}}}{P_{\text{SW}}} > 3$ demonstrating MDL signal refreshing and fan-out properties, which are

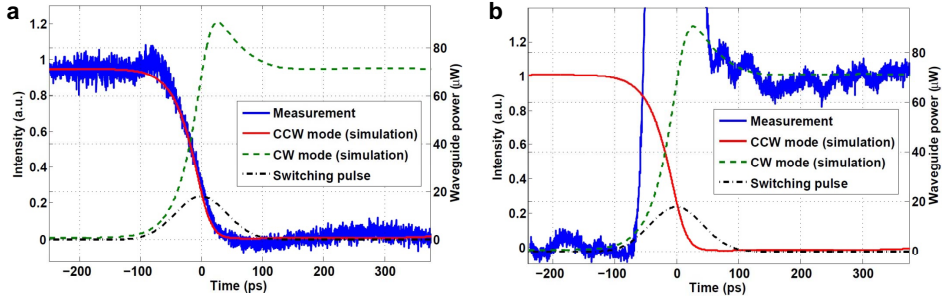


Figure 4.1: Switching of a MDL-based flip-flop. a) Falling edge and b) rising edge of the optical flip-flop. Note that the injected pulse reflected by the grating couplers screens the rising edge in the experiments. The measurement traces are a courtesy of L. Liu (Ghent University)

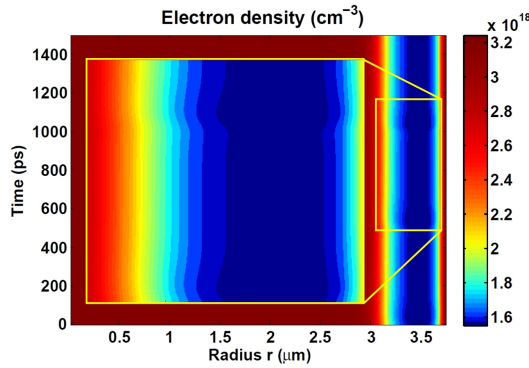


Figure 4.2: Temporal response of the electron density when switching, i.e., reverting the state of operation of the MDL-based optical flip-flop every 500 ps.

crucial for all-optical logic [114]. In Fig. 4.1 b) the falling edge of the CCW mode is shown, and a switching time of 60 ps is extracted from both the experiment and the simulations. Note that the rising edge could not be observed in the experiments because of back-reflections from the grating couplers screening the emitted laser power as evident from Fig. 4.1 b). Not only the switching time shows perfect agreement between experiment and simulation, but also the shape of the falling edge. This is attributed to the lateral discretization of the 1D model in which the modal and carrier dynamics can be simulated. Furthermore, the spatial hole burning of the carrier density can be temporally resolved.

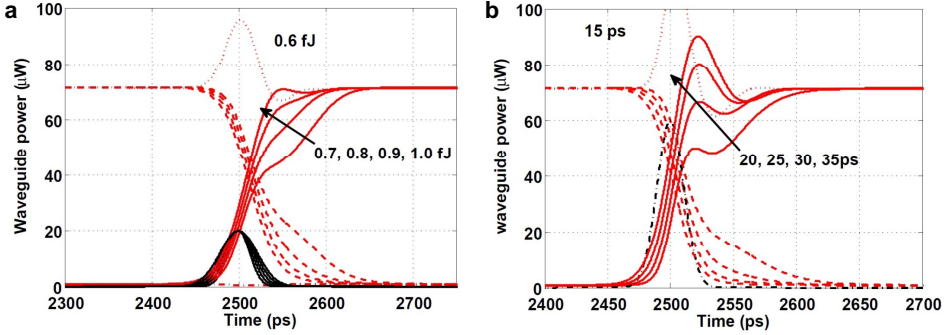


Figure 4.3: Simulations to investigate the ultimate switching performance of InP MDL-based optical flip-flop. a) Injection of an optical pulse with varying pulse energies (black curves) from 0.6 to 1.0 fJ. The emitted power of the central lasing mode of the device is shown in red. The device reverts its operation state for pulse energies as low as 0.7 fJ. b) Injection of an optical pulse with varying pulse widths from 15 to 35 ps. The device reverts operation for pulsed as short as 20 ps.

The carrier density is only reduced close to the perimeter of the MDL where the mode is located as can be seen in Fig. 4.2. However, if a pulse is injected and the state is switched, variations in the carrier density can be observed at $t_1 = 50$ ps. However, these variations are fairly low and only visible for the time of the overshooting photon densities in Figs. 4.1 a) and b), leading to the conclusion that the switching times are limited by the optical injection and suppression of the lasing mode rather than by a relaxation oscillation, in which an exchange of the power between the charge carrier density and the modal intensity takes place. Instead, switching between the two states is achieved when the external light injection is sufficiently long and with a sufficient energy to support the lasing of the suppressed mode. Thereby the dominant mode is suppressed by the non-linear gain suppression. When the intensity of the supported mode exceeds that of the dominant mode, the system flips and suppresses the previously dominant mode even further. Now, the other mode is stable suppressing the previously dominant mode until an external injection is applied.

Further simulations were performed to investigate minimum switching energies and injection times to flip the state of the device. Under the same bias conditions and with a lowered pulse width a minimum switching energy of 0.7 fJ was obtained as indicated in Fig. 4.3 a). Lower switching energies of 0.6 fJ did not revert the state of operation.

The switching energy basically scales with the number of photons that are present in the cavity and that need to be over-compensated by injecting into the counter-propagating lasing direction. When lowering the device size further the switching energy will be reduced accordingly, which, however, in turn also decreases the output power of the MDL-based flip-flop. This leads to a trade-off between the minimal output power that should be sustained in order to be able to detect the signal at a given speed with a given receiver, and the targeted switching energy.

To investigate the ultimate switching speed of the device, a relatively high power level of $60 \mu\text{W}$ was injected into the waveguide, which is still lower than the output power of the MDL. This condition must be fulfilled to simulate, e.g., a chain of equivalent MDLs in a system and to account for propagation losses of the waveguides. The pulse width has been varied from 15 to 35 ps as presented in Fig. 4.3 b). While a switching pulse of 15 ps is too short, a pulse width of 20 ps is sufficient to reverse the state of the MDLs. The corresponding switching energy of 1.2 fJ is still very small and comparable with that of low-power CMOS circuitry [115].

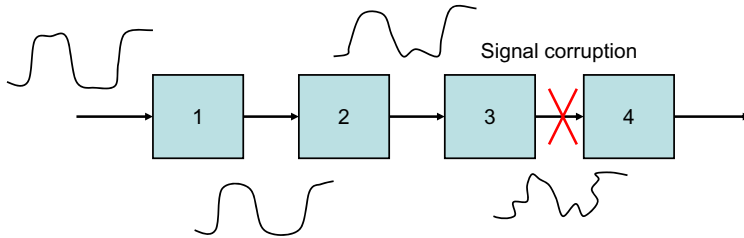


Figure 4.4: Illustration for cascability.

4.3 Requirements for all-optical logic and digital systems

The present section describes the fundamental requirements of logic systems, which also apply when building optical logic systems. The content of this section is largely based on the investigations of D.A.B. Miller et al., see Ref. [114]. The derived requirements are compared with the capabilities of InP microdisk-laser based all-optical flip-flops. Namely, the prerequisites for building logic systems are cascability, fan-out, signal refreshing and isolation, which are closely related. The following paragraphs give a short description of the terms.

Cascability Cascability defines the number of identical gates or logic blocks that can be concatenated without losing signal integrity. Fig. 4.4 illustrates such principle. A signal is injected into block 1, which leads to a distortion of the signal shape and also to an attenuation of the signal power at the output. The same happens for gates 2 and 3. However, at the output of gate 3, the signal has degraded so much that gate 4 cannot process the information any more. In the present example, the cascability would be limited to 3 gates / functional blocks. It is interesting to note that in CMOS logic gates each stage refreshes the signal thus assuring cascability.

It was found from simulations (and to some extent experiments) that the switching of the microdisk based all-optical flip-flops is not very sensitive to the power or energy level of the switching pulse, as long as it is larger than a power or energy threshold. The output power from a microdisk laser is also sufficiently large to allow it to switch another microdisk laser, cf. the fan-out specification. The main challenge is the required wavelength matching between different microdisk lasers. The injection locking range

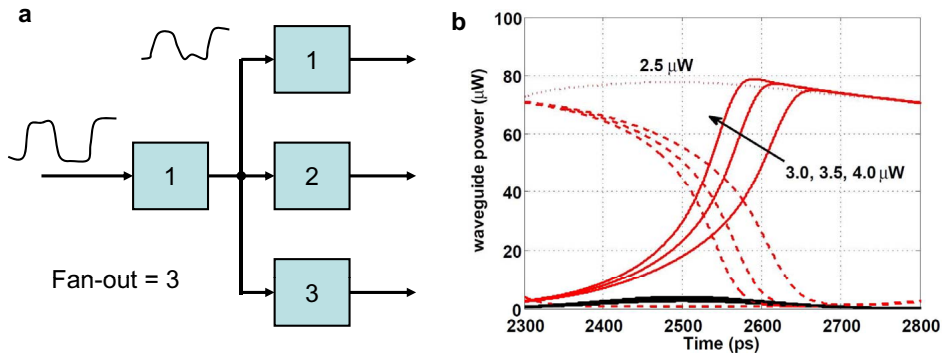


Figure 4.5: a) Illustration for fanout. b) Simulated fan-out.

for these lasers is currently a few tens of GHz (or few hundreds picometers). This requires quite accurate control of the different microdisk lasers and gates and it should be investigated whether the locking range can be made larger without compromising the switching properties too much. A possible solution is to increase the coupling between the microdisk and the straight silicon wire. The discussed measure lowers the quality factor Q of the cavity and broadens the wavelength range in which external light can be coupled into the device.

Fan-out The fan-out of a device defines the number of identical devices which can be driven. Fig. 4.5 a) illustrates how one stage can drive 3 identical stages. As the output power of the first stage is split into the amount of driven stages, the signal quality degrades. While in electronics the fan-out is limited to 2-4 due to the ever more reduced operation voltage, the microdisk laser exhibits a fan-out significantly larger than 10. Simulations have shown that a long-lasting input signal, see black curve in Fig. 4.5 b), can be as low as $3 \mu\text{W}$ and still change the state of the microdisk laser based flip-flop emitting at an output power (red curve) of approximately $70 \mu\text{W}$ resulting in a fan-out of larger than 23. Experimentally it could even be shown that an injection power of only 360 nW is sufficient to switch the state of a flip-flop emitting at $20 \mu\text{W}$ resulting in a fan-out of larger than 50 [51].

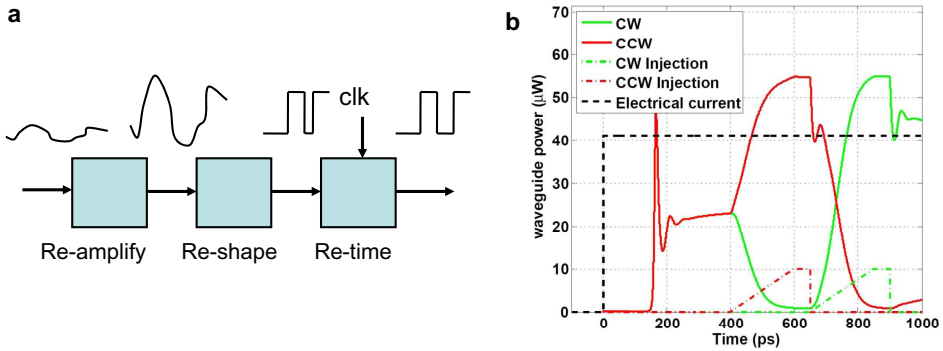


Figure 4.6: a) Illustration for signal refreshing including signal re-amplification, signal re-shaping and signal re-timing. b) Simulated signal re-generation properties of a MDL-based all-optical flip-flop.

Signal refreshing To prevent signal corruption between several stages (e.g., due to losses between the gates, attenuation within the gates, etc.), the signals need to be refreshed when necessary. Signal refreshing means that the signal is re-amplified, re-shaped and if necessary also re-timed. In CMOS, typically inverter chains fulfil this functionality. In optics, however, such functions remain challenging. Simulations have shown that signal re-amplification and re-shaping could be achieved with microdisk lasers as shown in Fig. 4.6 b). A weak signal is injected into the device with low power and a shallow slope. The microdisk laser flip-flop outputs a strongly amplified signal with a different shape (which would approach a rectangle for lower operation speeds). A gate is needed to achieve re-timing. This function could not be shown experimentally or by simulations, yet. Fig. 4.6 a) displays the different signal refreshing types. The given structure fulfils the functionality of a data-recovery unit. Note that each signal refreshing functionality can be performed by different blocks. It is not necessary to have one single block fulfilling all tasks.

Ideally, a digital system would intrinsically restore the signal integrity by performing 3R signal refreshing within the gate (e.g. as in an inverter in CMOS). However, it would also be possible to construct larger systems with signal refreshing stages when needed. E.g., in submarine communication lines there are repeaters only every few hundreds of kilometres.

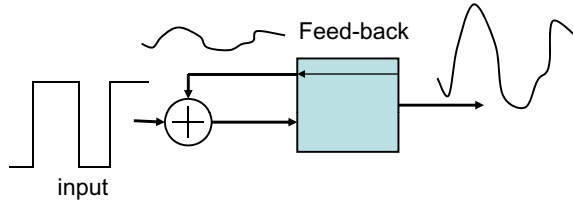


Figure 4.7: Illustration for optical isolation.

Isolation Optics is inherently reciprocal. This means that any given material supports the propagation of light independent of the propagation direction. Based on the reciprocity of the materials, no isolators can be formed in linear isotropic media. One exception is the Faraday rotator, in which the magneto-optic effect is used. In these devices, the polarization of the light is turned independent of the propagation direction. When placing a polariser as an analyser or a birefringent medium at the in- and output of the system, light in one propagation direction is blocked, while the other propagation direction is supported. In contrast to electric systems, where isolation can be achieved simply by adding an isolating layer between the input and the output of logic blocks (e.g., a gate dielectric), integrated optical isolators remain a challenge. One potential approach to achieve non-reciprocal structures are indirect photonic bandgap transitions, which was described theoretically [116] and demonstrated experimentally [117]. Although a CMOS compatible implementation of a non-resonant optical isolator was claimed recently [118], it was clarified meanwhile that this approach does not break the laws of reciprocity and cannot be used as an optical isolator [119]. Without breaking the reciprocity an approach to obtain a quasi-isolator is the implementation of resonant structures, which have a direction-dependent spatial distribution of the optical modes [120], which however is only feasible for multi-modal systems.

Approaches enabling true optical isolation are based on Faraday-rotation in which the light is rotated according to the propagation direction and subsequently filtered out. A viable, yet not CMOS compatible approach is the implementation of iron (Fe) doped InP waveguides mimicking the birefringence of garnet crystals [121].

Fig. 4.7 illustrates the case of an insufficient input-output isolation. In this example, part of the output signal is fed back into the input superimposing the input signal. This might lead to signal corruption at the output or even an oscillatory behaviour. Instead of corrupting the own input, also adjacent devices might be affected. This typically arises when coupling two microdisk lasers to one waveguide. In this case, an isolator should be placed in between the devices to grant only one signal propagation direction. Especially for the operation as all-optical set-reset flip-flop, any back reflection into a microdisk causes extra coupling between clockwise and counter clockwise modes, which can destroy the bi-stable operation possibility. Also, light injected into one disk by another disk can have a similar effect when the two disks can injection lock each other.

It has been derived that good unidirectional operation at realistic current injection requires the coupling between clockwise and counter clockwise modes to be smaller than $2 \times 10^9 \text{ s}^{-1}$. This implies that back reflections should be smaller than 10^{-3} (field reflection). The side mode extinction ratio of the device should be larger than 30 dB as only for devices exhibiting this SMSR value bi-stability could be observed.

Summary of requirements for logic The required functionalities to achieve an all-optical logic system are summarized in Tab. 4.1 and compared with CMOS electronics. It could be shown experimentally and through simulations that microdisk-based flip-flops fulfil the requirement of fan-out, i.e., that several devices can be driven by the emission of a single flip-flop. Also, it could be shown via simulations that microdisk-based optical flip-flops have the potential for signal re-generation, while this could not be shown experimentally.

The devices fail to fulfil the requirements of cascadability, which could not be shown within this thesis. I.e., it was not possible to connect the devices such that the emission of one flip-flop controls the emission of another one. This may be explained by the wavelength mismatch of adjacent devices due to fabrication tolerance during the disk definition. Although it could have been possible to compensate for this by carefully tuning the bias current, this careful adjustment of parameters is not desired in large-scale logic systems and violates the requirement for the absence of critical biasing [114].

The most challenging requirement of isolation was not met by the con-

| | Requirement | Achieved | CMOS electronics |
|-------------------|-------------|--|------------------|
| Cascadability | ∞ | 1 | ∞ |
| Fan-out | > 2 | > 20 (Simulation) > 50 (Experimental) | > 2 |
| Signal refreshing | 3R | 2R (Simulation), re-shape and re-amplify | 3R |
| Isolation | > 10 dB | 0 dB (Experimental) | > 20 dB |

Table 4.1: Parameter used in the 1D radially depended microdisk laser model.

cept of all-optical flip-flop based logic. Although there have been extensive numerical investigations on resonator structures with direction-dependent optical mode profiles mimicking optical non-reciprocity, this effect could not be observed experimentally in due course of this thesis. Therefore, further research in this direction is highly recommended.

4.4 Discussion

This chapter dealt with InP microdisk lasers used as all-optical flip-flops as building blocks for digital photonic circuits.

After introducing the concept of the optical flip-flop the spatially dependent multi-modal rate equation model presented in Chapter 3 was applied and compared to measurements. An optical switching energy of 1.8 fJ and a switching time constant of 60 ps were found experimentally and through simulations. Further simulations have shown the speed limitations of the switching process. It was found than these optical flip-flops can revert their state by injecting light pulses as short as 20 ps lending the device for high-speed operation. The minimal pulse energy to revert the state was estimated to 0.7 fJ. These results clearly show the potential for high-speed low-power bi-stable optical memory elements.

To investigate if these devices were also feasible for all-optical logic systems further simulations and measurements have been performed indicating that these devices meet the requirements of fan-out and signal refreshing. However, because of the need for critical biasing, no interaction between microdisk flip-flops could be shown and the requirement of cascadability could not be demonstrated. Furthermore, the requirement of signal isolation of forward-propagating signals from spurious reflecting signals could not be shown. Further research should be directed towards this goal in order to verify whether digital optical systems are a viable approach.

5 InP Microdisk Wavelength Converters

The present chapter describes the application of InP microdisks as wavelength converters. First, an introduction is given why wavelength conversion is an important functionality in optical systems. After explaining the principle of wavelength conversion in InP microdisks the static performance and dynamic operation of the devices are shown. Finally, the chapter is concluded and gives an outlook about how to further improve the wavelength conversion capabilities of InP microdisks. Parts of this chapter are published in several scientific publications^{6,7,8}.

5.1 Introduction

Silicon photonics is a promising technology platform, which is expected to deliver the ever more demanding IO bandwidth and IO density as required in future computing systems. As silicon does not exhibit electrically pumped optical gain due to its indirect band structure, heterogeneously integrated MDLs as shown in Fig. 5.1 are interesting candidates for on-chip laser sources [9]. Besides being used as laser sources, these devices, in combination with an external filter, have recently been demonstrated to operate as all-optical wavelength converters [55, 98]. Such functionality is needed for, e.g., optical networks for routing and contention resolution purposes. While most wavelength converters are based on four-wave mixing [43, 44] or cross gain modulation of single-pass devices [45, 46] and thus power hungry, wavelength conversion using longitudinal mode competition in MDLs was shown to be energy efficient as the device is a resonant structure, which enhances the cross-gain suppression [55].

When targeting scalable systems, it is desirable to have a single integrated device exhibiting the functions of both wavelength up- and down-conversion. As will be show shown, MDLs can be operated in such a man-

⁶J. Hofrichter *et al.*, All-optical wavelength conversion using mode switching in an InP microdisk laser, *Electronics Letters* **47**(16), pp. 927-929 (2011).

⁷J. Hofrichter, InP Microdisks as versatile devices for light generation, processing and detection, *Proceedings of the 37th European Conference and Exhibition on Optical Communication, ECOC 2011*, Geneva, Switzerland, Sunday workshop on optical integration, invited, (2011).

⁸J. Hofrichter *et al.*, Dual Wavelength Conversion Using Electrically Pumped Microdisk Lasers, *IEEE Group IV Photonics Conference*, London, United Kingdom, ThB3, (2011).

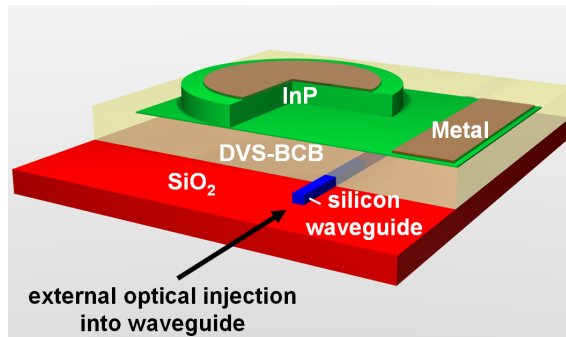


Figure 5.1: Device structure of an MDL heterogeneously integrated on a silicon-on-insulator waveguide. The InP cavity is mounted on top of a pre-structured silicon nanophotonic waveguide using BCB as adhesive material and electrically connected using platinum-gold metal pads.

ner, enabling small, integrated wavelength converters. Their typical footprint and power consumption are orders of magnitude smaller than those of other devices used for wavelength conversion, such as distributed feed-back lasers [122], dielectric Bragg reflector lasers [123], InP semiconductor optical amplifiers [46], silicon waveguides [43, 44], Fabry-Pérot lasers [124], and vertical-cavity surface-emitting lasers [125]. While for MDLs it has recently been shown that wavelength conversion can be performed towards shorter wavelengths [55], the complementary conversion capabilities to longer wavelengths are to be demonstrated. Furthermore, the use of a seeding laser, which greatly improves the operation speed of such a converter [98], should be avoided to lower the system complexity.

In this chapter, the operation of a single MDL as both an up and down wavelength converter without the use of a seeding laser is reported. Error-free operation of the disk laser converter at a bit rate of 2.5 Gb/s is presented with a power penalty of ≈ 8 dB.

5.2 Principle of mode switching

The basic concept for employing a disk laser for wavelength conversion can be explained using Fig. 5.2. Under normal operating conditions, the MDL, whose diameter is $7.5 \mu\text{m}$, emits light into a single longitudinal mode, see Fig. 5.2 a). Bi-modal operation in both directions results from the gain dependence on wavelength and the large wavelength separation of ≈ 30 nm,

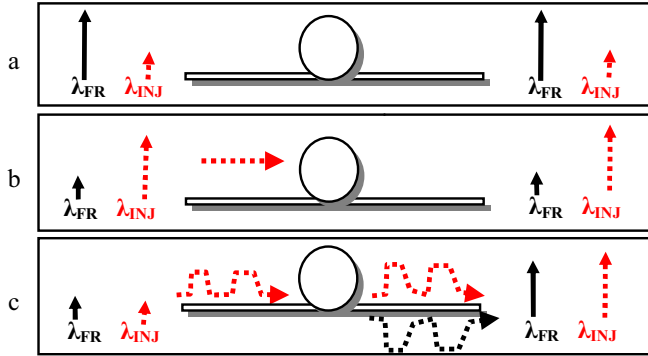


Figure 5.2: Operation of a disk laser as a wavelength converter. (a) Free-running (FR) lasing with predominant λ_{FR} . (b) Light is injected into the suppressed side-mode (λ_{INJ}) to injection-lock the laser, resulting in suppression of λ_{FR} . (c) If the injected light is modulated, the laser is wavelength converting the signal at λ_{INJ} to λ_{FR} .

due to the micron-sized cavity, between consecutive longitudinal modes. Injecting light into any of the suppressed lasing cavity modes of the MDL will force the disk to lase at the injected wavelength. This principle is called injection-locking [126]. All other longitudinal modes of the MDL including the free-running mode will be suppressed in both directions (see Fig. 5.2 b). When the injected light is removed, the MDL reverts to operating at its original free-running lasing mode (see Fig. 5.2 c). When the free-running mode is selected by a filter and detected by a photo diode, the device performs the function of a wavelength converter.

5.3 Static characteristics

The characterization was performed on a custom made setup with manually aligned fiber probes sensing the grating couplers. The threshold current of the device was ≈ 0.25 mA and the fiber-coupled power exceeded $10 \mu\text{W}$ for a bias current of 4 mA. When biasing the MDL at $I_{LO} = 2.72$ mA, the mode at 1560 nm becomes dominant. Due to a shift of the gain spectrum and the variation of the refractive index due to Joule heating, the lasing mode at 1590 nm becomes dominant for a higher bias current of $I_{HI} = 3.53$ mA. For both cases, the line-width is 2 pm. Static injection locking experiments were performed first to quantify the static extinction ratio of the lasing

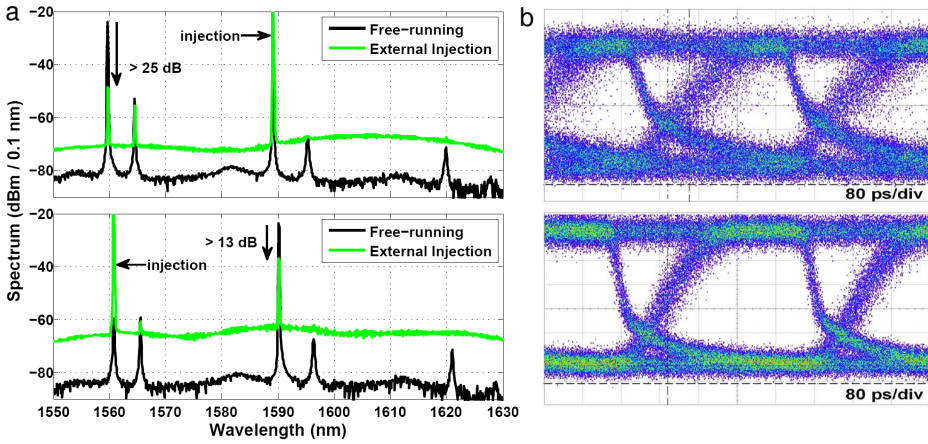


Figure 5.3: a) Top: Lasing spectrum for $I_{LO} = 2.72$ mA with and without external injection. Bottom: Lasing spectrum for $I_{HI} = 3.53$ mA with and without external injection. b) Eye diagrams for dynamic operation at 2.5 Gb/s. Top: With bias current $I_{LO} = 2.72$ mA. Bottom: with bias current $I_{HI} = 3.53$ mA

modes. When biasing the device with $I_{LO} = 2.72$ mA and injecting an external continuous-wave (cw) light signal at 1590 nm, an extinction of 25 dB was obtained as shown in Fig. 5.3 a) (top). For $I_{HI} = 3.53$ mA and injection at 1560 nm, an extinction ratio of over 13 dB was achieved as visible in Fig. 5.3 a) (bottom).

This proves that the MDL can be injection-locked to either of its suppressed side modes, i.e., to a higher and to a lower wavelength lending the device to wavelength conversion applications as will be shown below. The different noise floors in Fig. 5.3 a) stem from the EDFA's amplified spontaneous emission (ASE) accompanying the injected beam, which was not filtered out.

5.4 Dynamic characteristics

After the static measurements, dynamic measurements were performed to investigate the temporal behavior of the conversion process. The measurement setup is depicted in Fig. 5.4. The sample was mounted on a thermoelectric cooler (TEC) to stabilize the device temperature at 18 °C. RF probes connected the device with a current source for electrical pumping. The light was then coupled off the chip by a grating coupler using a single-

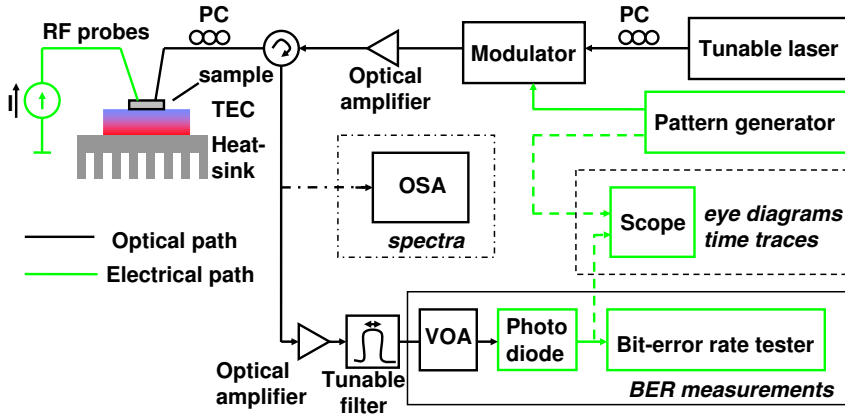


Figure 5.4: Measurement setup for the dynamic wavelength conversion experiments

mode fiber. The spectra were taken by an HP OSA, and the high resolution spectrum to estimate the line-width was taken with a high-resolution OSA. For the wavelength conversion experiments, a tunable laser was modulated with a 10 Gb/s lithium niobate modulator driven by a pulse pattern generator (PPG) and subsequently amplified. The light was then coupled in and off the chip with the same fiber. The converted light was coupled out through a circulator and amplified by a second optical fiber amplifier. The ASE of the amplifier was filtered out by a manually tunable filter centered at the wavelength of the free-running lasing mode thus extracting the wavelength-converted signal. Then the signal was detected in a high-speed photo diode (PD) and was either attenuated for BER measurements using an Anritsu 12.5 Gb/s bit-error rate tester or detected by a high-speed optical sampling scope. For both conversion directions, open eyes at 2.5 Gb/s were obtained as shown in Fig. 4. BER measurements with a non-return-to-zero (NRZ) PRBS length of $2^{31}-1$ were performed to analyze the quality of the converted signal.

For 2.5 Gb/s, operation with a BER of 1×10^{-10} was achieved with a power penalty of 8 dB at an injection power level of 1.5 dBm as shown in Fig. 5.5. Assuming a coupling loss of 6 dB, the corresponding emitted waveguide power is $60 \mu\text{W}$, while the injected waveguide power is $355 \mu\text{W}$, resulting in an emission-to-injection power ratio of 0.17 or -7.5 dB. Note, that the experiments were performed without the use of an additional

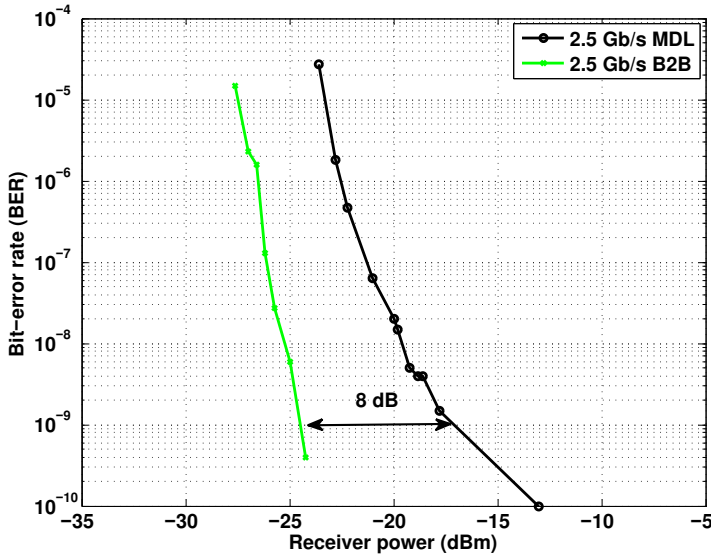


Figure 5.5: Bit-error rate measurements of the MDL and the back-to-back (B2B) system at a 2.5 Gb/s. The bias current is $I_{HI} = 3.53$ mA.

continuous-wave seeding beam to improve the speed of the modal recovery [98]. Although this greatly simplifies the operating condition, the disadvantages are an increased turn-on delay and a random turn-on behavior as the mode has to recover from noise and spontaneous emission. The large power penalties are due to the low emission power of the MDL-based wavelength converter and the fibre-to-chip coupling losses. The extinction ratio was measured to be 8.4 dB. The power penalty can be improved further by increasing the output power of the device by, e.g., further optimizing the coupling between waveguide and MDL cavity.

5.5 Improving the speed of wavelength conversion by seeding

To investigate the speed limitations and ways to improve the speed of the wavelength conversion process the multimodal MDL model as described in section 3.2 was employed. By gain suppression, the previously dominant central lasing mode is suppressed. In order to operate at high bit rates and high repetition rates, the recovery of the central lasing mode may be accelerated by seeding low-power continuous-wave light into the

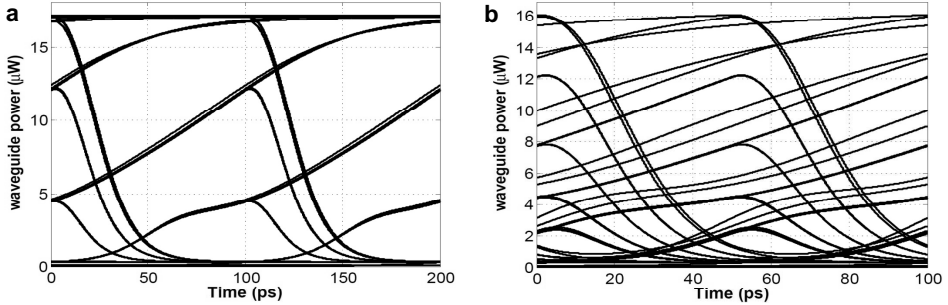


Figure 5.6: Simulated eye diagrams for wavelength conversion with $50 \mu\text{W}$ external injection. a) Without seeding at 10 Gb/s and b) Without seeding at 20 Gb/s.

central lasing mode [98, 127]. When monitoring the relative eye opening $EO = (P_{1,eye} - P_{0,eye}) / P_{1,max}$ during wavelength conversion, it becomes clear that seeding improves the eye opening for both 10 Gb/s and 20 Gb/s as can be seen in Figs. 5.7 a) and b), the EO is strongly improved by seeding of continuous-wave light into the central mode.

The eye diagram for $50 \mu\text{W}$ signal injection in the absence of seeding is reproduced in Figs. 5.6 a) and b) for 10 and 20 Gb/s. The largest EOs that can be achieved with seeding are shown in Figs. 5.7 a) and b) for 10 and 20 Gb/s, respectively. The simulated eye diagrams demonstrate excellent agreement with the experimental data in Figs. 5.7 c) and d). Although the power levels in the waveguide are experimentally inaccessible, the rise and fall times are not only equivalent but also symmetric in both cases. From Fig. 5.7 a) the 10%-to-90% rise time was estimated to be approximately 55 ps. To further improve the operation speed of the devices, a higher external signal injection may be used. It was also found that a lower total intensity in the cavity, i.e. a smaller disk diameter, leads to faster switching time. Experimentally [127], the scheme of injection seeded disk lasers wavelength converter was shown to operate error-free with a BER below 10^{-9} for the operation at 10 Gb/s when using seeding. Although the eye for 20 Gb/s looks degraded, a BER below 10^{-3} was achieved which is sufficiently low for applications using forward error correction (FEC).

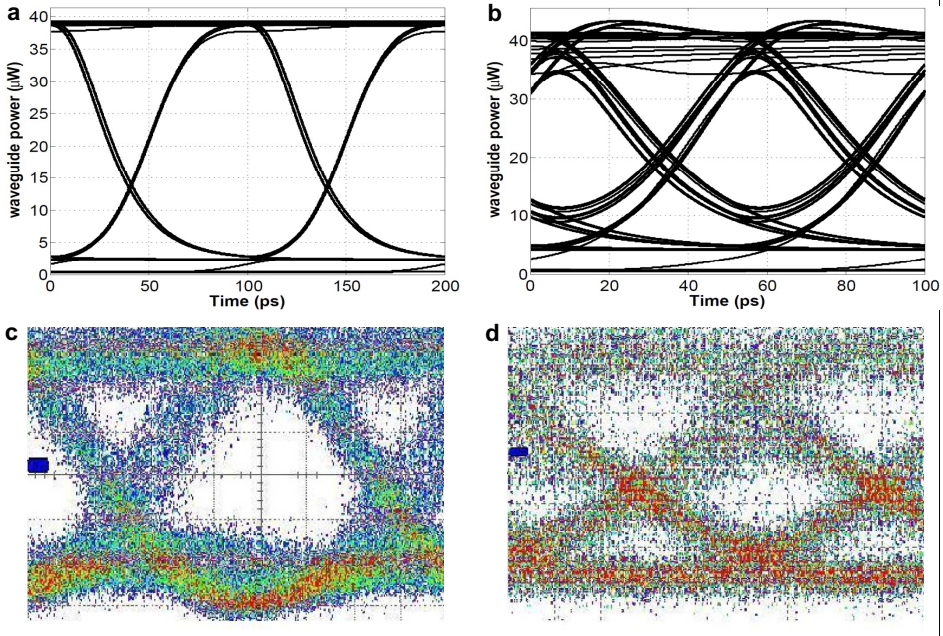


Figure 5.7: Eye diagrams for wavelength conversion with $50 \mu\text{W}$ external injection: a) with seeding with a power of $2 \mu\text{W}$ at 10 Gb/s and b) with seeding with a power of $5 \mu\text{W}$ at 20 Gb/s. c) Measured eye diagram at 10 Gb/s with seeding. d) Measured eye diagram at 20 Gb/s with seeding. The measured eye diagrams are a courtesy of Dr. Oded Raz, TU Eindhoven.

5.6 Discussion

We have demonstrated the wavelength up- and down-conversion in a single MDL heterogeneously integrated on top of an SOI waveguide. To investigate the application in the system context, the wavelength conversion experiments have been performed without seeding. For the first time, it has been shown that a single MDL can perform both up- and down-conversion, enabling large-scale wavelength conversion systems. Static extinction ratios of 25 dB and 13 dB, respectively, were shown for injection locking to a side mode. Error-free operation with a BER of 1×10^{-10} at 2.5 Gb/s and a power penalty of 8 dB was reported. The work presented here demonstrates the feasibility of MDLs in scalable wavelength conversion systems, in which the capability of performing both up- and down-conversion in a single device is essential. The demonstrated speed is on the order of the

central processing unit (CPU) clock speed and thus suitable for on-chip applications.

We have employed the microdisk laser model presented in section 3.2.2. The simulations of the wavelength conversion process using seeding resulted in good agreement with measurements at both 10 and 20 Gb/s. It was shown that with seeding, wavelength conversion can be performed at 20 Gb/s with an acceptable BER. The model holds promise to facilitate the further exploration of various MDL functionalities, and to guide experimental work.

The limitations of using microdisk lasers as wavelength converters are the fixed wavelength grid defined by the FSR and the relatively large power penalty. When using such devices in wavelength conversion systems special attention is to be paid that the FSR of the device matches the desired wavelength conversion grid. As the device is not tuneable a cascade of MDL-based wavelength converters may be employed.

To overcome the large power penalty the devices may be optimized such that they emit large output power levels by the measures discussed in chapter 3. Furthermore, the coupling losses caused by the grating couplers may be reduced as discussed in chapter 8.6 at the end of this thesis.

The advantages of MDL-based wavelength conversion are the high conversion efficiency compared with other wavelength conversion concepts, such as four-wave mixing [43, 44], and the low power consumption compared with e.g., SOA-based approaches [45, 46].

6 InP Microdisk Detectors

This chapter describes the use of InP microdisks as photodetectors under negative bias. First, static performance figures such as the spectrally-resolved responsivity are presented. Then, results on dynamic operation including eye diagrams and bit-error rates are reported. The performance limitations encountered are discussed and an indication for future work how to improved the performance of InP microdisk detectors is given.

Parts of this chapter were published in several scientific publications^{9,10,11}.

6.1 Introduction

The heterogeneous integration platform is an attractive path to extend the capabilities of silicon photonics. In this technology, photo detectors [128], lasers [9], wavelength converters [56], and modulators [50] have been shown. In InP-based material with MQWs the band gap and thus the absorption can be modulated by the quantum confined Stark effect (QCSE) [71]. Moreover, the light intensity can be modulated, and also detected as a photo current [58].

In this chapter, the performance of InP microdisks used as photo detectors under negative bias, which have been heterogeneously integrated on a SOI waveguide, is reported. Eye diagrams, a small signal analysis and bit-error rates up to 10 Gb/s are presented.

6.2 Static characteristics

InP microdisks can be used as resonant photo detectors under negative bias. When injecting light pulses on resonance wavelengths of the device, the absorption induced by the QCSE results in substantial photocurrent as

⁹J. Hofrichter *et al.*, Compact InP-on-SOI Microdisks Used as High-Speed Modulators and Photo Detectors, *Proceedings of the 38th European Conference and Exhibition on Optical Communication, ECOC 2012*, P. 2.03 (2012)

¹⁰J. Hofrichter, InP Microdiscs as versatile devices for light generation, processing and detection, *Proceedings of the 37th European Conference and Exhibition on Optical Communication, ECOC 2011*, Geneva, Switzerland, Sunday workshop on optical integration, **invited** (2011).

¹¹J. Hofrichter *et al.*, Microdisc Lasers Coupled to Silicon Waveguides as Versatile On-Chip Optical Components for Light Generation, Conversion and Detection, *Semiconductor Conference Dresden, SCD 2011*, Talk 2.6.2 (2011).

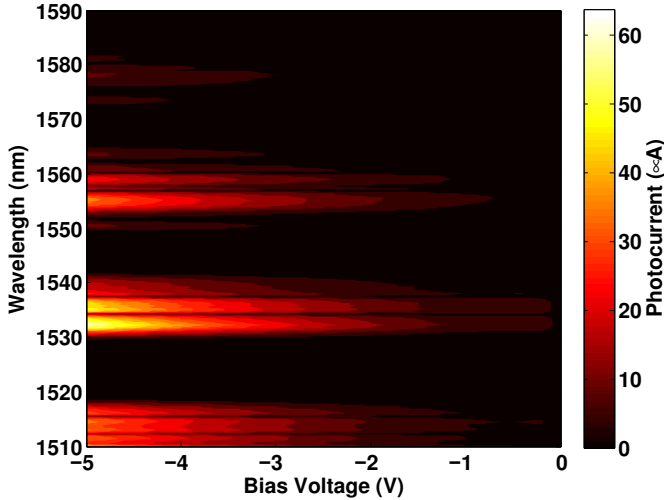


Figure 6.1: Photo-current generated in the InP microdisk photo detector as a function of bias and wavelength.

shown in Fig. 6.1. The plot displays the spectral response of the photocurrent for varying bias voltage. The absorption in the cavity is resonantly enhanced enabling photocurrents as large as $60 \mu\text{A}$ on-resonance at a wavelength of 1532 nm and a bias voltage of -5 V. The resonances are repeated every 24 nm, which is the FSR of the cavity. For each FSR, several modes are present in the cavity resulting in several side-modes with a lower signal response, for example at around 1536 nm.

By normalizing the photocurrent to the power in the waveguide, the responsivity has been computed as shown in Fig. 6.2. A negative bias voltage as low as 1 V is sufficient to achieve unity responsivity, whereas a bias voltage of -5 V yields a responsivity of more than 5 A/W due to the high electric field in the non-doped region of the devices which is sufficient to create an avalanche effect [129]. When assuming ideal, steep doping profiles of the epitaxial stack and an un-doped region with a width of 113 nm, the electric field strength at 1 V negative bias is 88.5 kV cm^{-1} , which is similar to the field strengths ranging from 40 to 120 kV cm^{-1} observed in bias-free tungsten-germanium avalanche photo-diodes (APDs) [69].

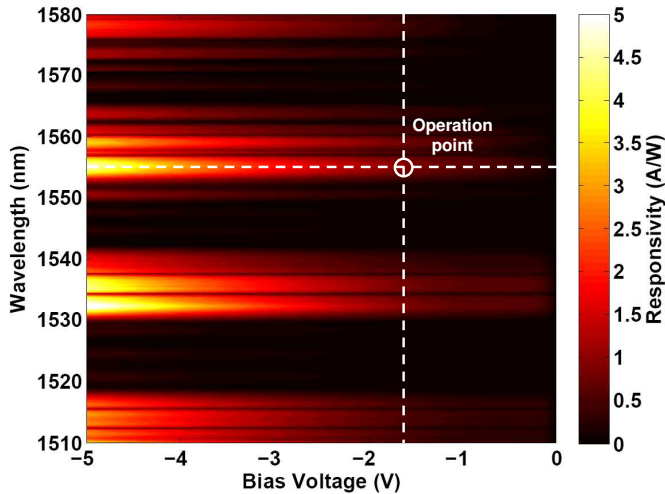


Figure 6.2: Responsivity of the InP microdisk used as a photo detector as a function of bias and wavelength.

6.3 Dynamic characteristics

For evaluating the temporal behavior of the detection process, BER measurements with a PRBS pattern length of $2^{31}-1$ have been performed at a wavelength of 1555.6 nm and a negative bias voltage of 1.7 V. Although the responsivity around 1532 is slightly higher, an operation wavelength of 1555.6 nm was chosen in order to be able to amplify the signal with an EDFA. As shown in Fig. 6.4 error-free operation could be achieved for 2.5 Gb/s and 5.0 Gb/s. For 10 Gb/s operation with a BER below 1×10^{-3} (i.e., below the FEC limit) could be achieved. The photocurrent was translated into a voltage using the 50Ω input impedance of the amplifiers, which electrically amplified the signal by 50 dB. The cascade of electrical amplifiers had a bandwidth of 12 GHz. The noise figure of the amplifiers was 6 dB thus inducing substantial noise. Still, an open eye was achieved for 10 Gb/s as shown in Fig. 6.4 (inset). To gain insight into the actual speed limitations of the device a small signal analysis was performed to determine the S_{21} parameter. The reference measurement was made with a 40 Gb/s lithium niobate modulator and a commercial 43 Gb/s photo receiver. For the InP microdisk device a 3dB-optical-electrical bandwidth of 8 GHz (see Fig. 6.3) was measured indicating that the device can be used as a photo

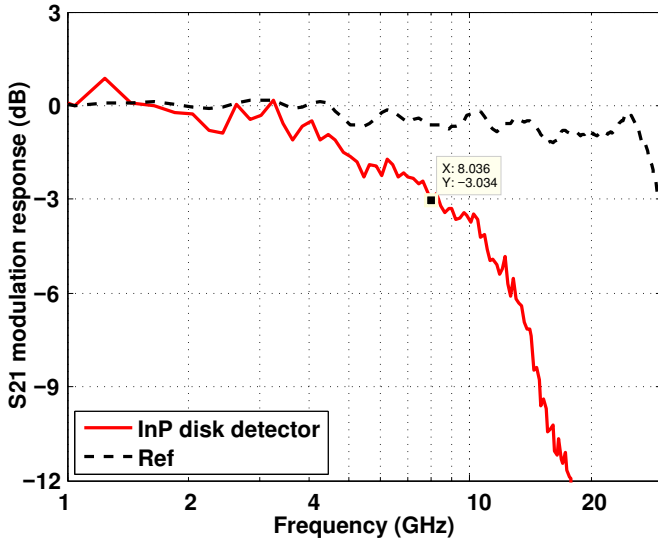


Figure 6.3: Small signal response of the InP microdisk used as a photo detector. The black broken line indicates a commercial 43 Gb/s photoreceiver.

receiver up to 10 Gb/s when co-integrating a trans-impedance amplifier.

6.4 Discussion

Resonances and spectral behaviour The potential of reversely biased InP microdisks heterogeneously integrated on top of a SOI waveguide as high-speed photo detectors was demonstrated. The detectors are based on resonant devices resulting in a response corresponding to the resonance wavelengths of the InP disk cavity. Whereas it is difficult to control the exact spectral position of the resonance wavelength by accurate size control of the disk, it is possible to implement several disks with varying diameter on one single silicon waveguide bus that fully cover one spectral range [39, 130]. The free-spectral range is determined by the diameter of the disks. If a process variation results in an altered diameter, then all disks are affected equally resulting only in a relative shift of the resonances with respect to each other. A wavelength-selective detector array can be formed by integrating a plurality of microdisk detectors on one waveguide. This way, wavelength splitters, such as AWGs for instance, which have a large foot-print, may be omitted. Such a resonant detector bench can then be

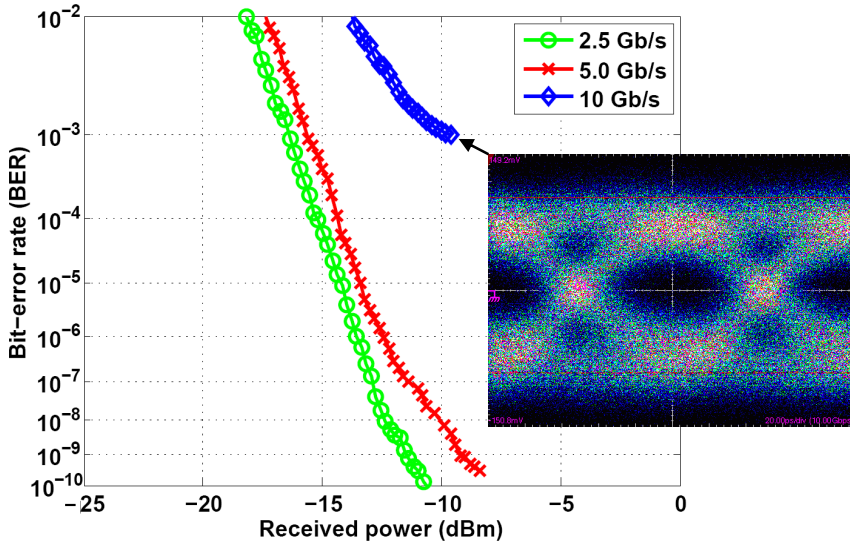


Figure 6.4: Bit error-rate measurements of the InP microdisk used as a photo detector at 2.5, 5.0 and 10 Gb/s and a PRBS length of $2^{31}-1$.

electronically re-scrambled using, e.g., a shift register [39]. When using the InP microdisks as lasers the same principle can be applied enabling wavelength-grid matched laser and detector benches.

Responsivity Static measurements demonstrated on-resonance responsivities of up to 5 A/W, which is substantially larger than normal non-resonant detectors. This clearly shows that these devices are well-suitable to be operated as photodiodes.

High-speed operation Dynamic operation up to 10 Gb/s and a S_{21} bandwidth of 8 GHz was demonstrated. Error-free operation could be achieved for 2.5 Gb/s and 5 Gb/s and operation below the FEC limit was shown for 10 Gb/s. The device combines low footprint and high operation speed.

This, together with the possibility of co-integrating lasers with modulators [60, 61, 131] and photo detectors [59] using the same epitaxial material and processing scheme, makes the presented device very attractive for integrated photonics.

Outlook The performance of the InP detectors was largely limited by the absence of a TIA. Such an electronic component is needed to efficiently transform the generated photocurrent into a voltage, which can then be amplified electronically. For the present experiments only normal electronic amplifiers have been used that are impedance-matched to 50Ω , and thus only have a transimpedance of this value. It is expected that when co-integrating the devices with a TIA error-free operation up to 10 Gb/s is within reach as the device exhibits a small-signal bandwidth of 8 GHz.

7 InP Microdisk Modulators

The present chapter describes the use of InP microdisks as electro-optical modulators. First, an introduction to the state-of-the-art in modulators is given and then the use of InP microdisks as electro-optical modulators is highlighted. The modulators can be operated either under forward bias conditions using the free-carrier plasma-dispersion effect by injecting carriers, or under negative bias conditions where the absorption of the device is modulated. For both modes of operation static and dynamic measurements are performed. The capabilities of both modes of operation are compared at the end of this chapter. Parts of this chapter are published in several scientific publications^{12,13,14,15}

7.1 Introduction

Heterogeneous integration is an attractive path to extend the capabilities of silicon photonics [73]. In the heterogeneous integration platform photodetectors [74], lasers [9], wavelength converters [55, 56, 98] and modulators [50] have been shown. Modulators based on the free-carrier plasma-dispersion effect, either formed as a disk, [50, 132], a ring [48, 133], or a Mach-Zehnder interferometer [68, 134] have attracted much interest. Other modulators are based on the Franz-Keldysh effect in strained silicon-germanium (SiGe) [135, 136]. Because the electro absorption obtained by the QCSE of InP-based MQWs is higher than that of SiGe based MQW materials, the former material system was investigated more closely.

In this section, two different operation modes of an InP microdisk modulator heterogeneously integrated on top of a silicon waveguide [131] are reported. Static electrical and optical performance metrics are presented, and dynamic operation up to 2.5 Gb/s is shown. Bit-error-free operation

¹²J. Hofrichter *et al.*, A low-power high-speed InP microdisk modulator heterogeneously integrated on a SOI waveguide, *Optics Express* **20**(9), pp. 9363-9370 (2012).

¹³J. Hofrichter *et al.*, Inverting and non-inverting operation of InP microdisk modulators, *Electronics Letters*, **48**(10), pp. 586-588 (2012).

¹⁴J. Hofrichter *et al.*, Compact InP-on-SOI Microdisks Used as High-Speed Modulators and Photo Detectors, *Proceedings of the 38th European Conference and Exhibition on Optical Communication, ECOC 2012*, P. 2.03 (2012)

¹⁵J. Hofrichter *et al.*, Compact high-speed InP microdisk modulators heterogeneously integrated on a SOI waveguide, *Proceedings of the IEEE Optical Interconnects Conference*, Paper MB6 (2012).

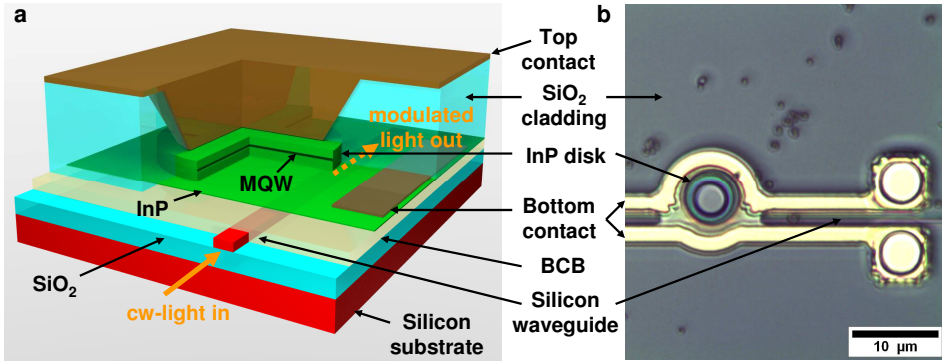


Figure 7.1: Device structure of an InP microdisk modulator heterogeneously integrated on a SOI waveguide. a) Schematic view of the final device including the final metalization. b) Optical microscope image of the InP microdisk modulator before the final pad metallization.

(BER lower than 1×10^{-10}) at 1.0 Gb/s is reported for both operation modes. In the experiments, the device was biased with voltage swings as low as $V_{pp} = 1.0$ V and can thus be directly driven with state-of-the-art CMOS electronics.

This section shows also the performance of InP microdisk modulators in the carrier depletion operation regime, i.e. under negative bias. [60]. High-speed operation of the device with a bit-error rate below 1×10^{-9} at data rates of 2.5 Gb/s, 5.0 Gb/s and 10 Gb/s is demonstrated. The performance of the InP microdisk modulators is compared with a commercial lithium niobate modulator. Power penalties are presented and discussed. Finally, the power consumption is calculated and compared with that of state-of-the-art modulators [60].

7.2 Fabrication

The InP microdisk modulator has been fabricated using the heterogeneous integration platform [73]. First, the silicon photonic waveguide circuitry including waveguides and grating couplers is fabricated on a SOI wafer using 193 nm DUV lithography [37]. On an InP wafer a MQW structure is grown as described in section 2.5. The MQW structure is formed by three InAsP quantum wells with a PL emission at 1520 nm embedded in non-intentionally doped (nid) quaternary indium gallium arsenide phos-

phide (InGaAsP) material with a band gap of 1.2 eV. The layer stack also comprises a tunnel junction that allows for only one metallization step to contact both n-contacts of the device [12]. Then, a BCB adhesive was spun on top of the SOI substrate onto which a die of the InP wafer was bonded. Subsequently, the InP substrate is removed chemo-mechanically and the device is structured using optical lithography and dry etching. A silicon dioxide over-cladding of the device was used to improve its heat-sinking. The metallization is realized by lift-off and titanium-platinum-gold (TPA) contacts. Figure 7.1 a) displays the schematic device structure after completion all fabrication steps. An optical microscope image made before the final pad metallization is shown in Fig. 7.1 b). The diameter of the active region, i.e. the MQW disk structure, is $8\ \mu\text{m}$, resulting in an active area of only $\approx 50\ \mu\text{m}^2$. When light is injected into the waveguide at one of the resonance wavelengths, it can couple to the whispering-gallery modes of the disk. The light can be modulated by changing either the resonance wavelength of the device using the free-carrier plasma-dispersion effect [50] or by changing the absorption properties of the disk, as will be shown below.

7.3 Forward biased InP microdisk modulators

7.3.1 Static characteristics

The characterisation was performed on a custom-made setup with automatically aligned fibre probes injecting polarisation-controlled light from a tunable laser into the waveguide using grating couplers. The device was biased electrically using a semiconductor device analyser. Fig. 7.2 a) shows the I-V characteristics of more than 30 microdisk modulators fabricated on the same chip. For zero bias, the measured current is within the noise and thus negligible.

At 1 V bias the current is about $10\ \mu\text{A}$ and increases to 1 mA for 2 V bias voltage. To demonstrate low-power operation for potential on-chip applications with very limited supply voltage, the bias voltage swing was restricted to $V_{pp} = 1.0\ \text{V}$. Also, it is desirable to have the functions of inverting and non-inverting modulation operation in the same device. By increasing the voltage from 0 V to 1 V, the resonance wavelength of the device is blue-shifted because of the free-carrier plasma-dispersion effect, resulting in a drop of the static transmission by 9.6 dB at a wavelength of 1556.2 nm, as shown in Fig. 7.2 b). Note that, although Fig. 7.2 b)

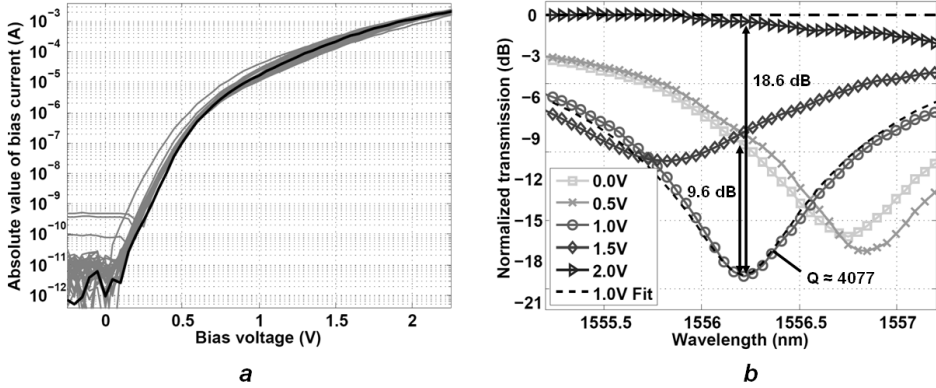


Figure 7.2: a) Static electrical I-V-characteristics of more than 30 microdisk modulators on same chip. Device investigated is highlighted b) Static optical transmission curves of measured device highlighted in 7.2 a) for positive bias voltages.

displays the optical transmission characteristics for only one device, this behaviour was also observed for the other devices, but at a different wavelength because of fabrication variations slightly altering the diameter of the InP disc cavity. When increasing the bias voltage above the threshold voltage ($V_{th} = 1.5$ V) to 2 V, the resonance is strongly reduced because the microdisk is electrically pumped and the losses in the microdisk are reduced. In static operation, also the resonance is red-shifted because of thermal heating of the device (see Fig. 7.2 b). However, under dynamic operation this cannot be observed because the thermal time constant is in the order of microseconds. For the operation wavelength of 1556.2 nm and at a bias of $V_{HI} = 2$ V, the transmission increases by 18.6 dB, reducing the loss to 0.4 dB compared with the straight waveguide. For this wavelength and a bias of 1 V, the transmission drops to the minimum value, thus indicating critical coupling. The maximal transmission dip was fitted with a simple ring resonator model and extracted a quality factor of $Q = 4077$. In summary, the device can be operated in inverting operation mode when biased between $V_{LO} = 0$ V and $V_{HI} = 1$ V and as a non-inverting modulator when driven with $V_{LO} = 1$ V and $V_{HI} = 2$ V.

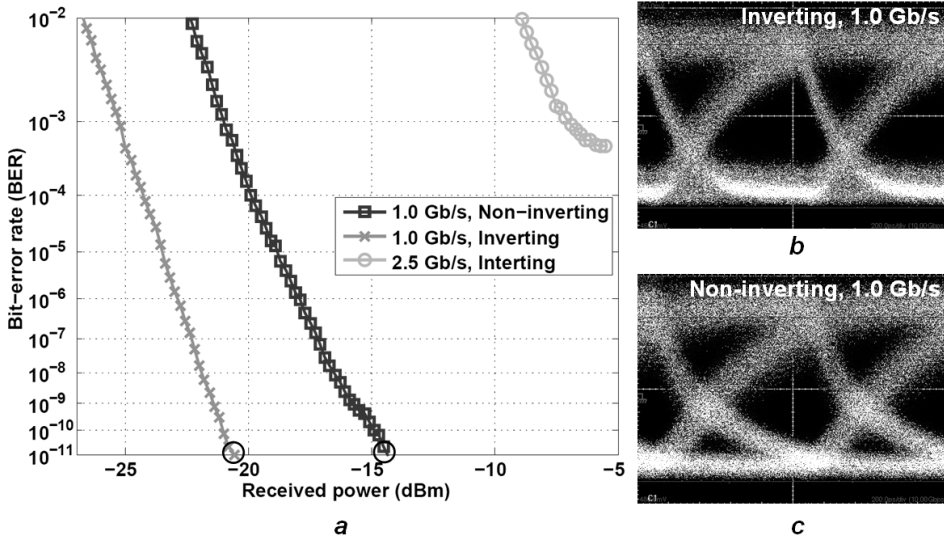


Figure 7.3: Dynamic measurements of the forward-biased InP microdisk modulator a) Bit error rate measurements at 1.0 Gb/s for inverting and non-inverting operation, and at 2.5 Gb/s for inverting operation. b) Eye diagram for inverting operation at 1.0 Gb/s. c) Eye diagram for non-inverting operation at 1.0 Gb/s.

7.3.2 Dynamic characteristics

Dynamic measurements were performed to investigate the temporal behaviour of both operation modes. The sample was mounted on a thermoelectric cooler to stabilise the device temperature at 20 °C and was directly driven by a high-speed PPG using a radio-frequency probe. Polarisation-controlled light from a tunable laser was coupled into and out of the chip by grating couplers and cleaved singlemode fibres. The transmitted optical signal was amplified by an EDFA and spectrally filtered. A 10 Gb/s photoreceiver was used for detection and electrically amplified the signal before measuring the BER using a 12.5 Gb/s error detector. The eye diagrams were recorded with a high-speed oscilloscope. For a NRZ-PRBS length of $2^{31}-1$, error-free operation (i.e., operation with a BER lower than 1×10^{-10}) was achieved for both operation modes at 1.0 Gb/s as shown in Fig. 7.3 a). For the inverting and non-inverting operation mode a received power of -19.2 dBm and -18.0 dBm, respectively, is required to recover the signal without errors.

As shown in Fig. 7.3 b), the eye is clearly open for the inverting mode with a dynamic extinction ratio of 6 dB, whereas it appears slightly less open for the non-inverting mode with an extinction ratio of 8 dB as indicated in Fig. 7.3 c). When biasing the disc between 1 V and 2 V in the non-inverting operation mode, the lasing threshold is crossed resulting in slower rising and falling times as well as cross-gain modulation induced jitter, as the turn-on of the disc laser is pattern-dependent and affects the exact timing of the resonance shift [137]. The jitter translates to the power penalty observed in Fig. 7.3 a). For 2.5 Gb/s, the operation could be demonstrated for the faster inverting operation mode. For a received optical power of -7 dBm, the BER is lower than 1×10^{-3} , which is sufficient for systems using forward error correction. Small-signal S-parameter measurements have shown a 3 dB bandwidth of 1.44 GHz for the inverting mode. The non-inverting mode exhibits 0.84 GHz, thus clearly indicating speed limitations for the operating mode based on the modulation of the losses in the disc cavity. If desired, the speed of the device could be further improved with the pre-emphasis technique [133].

7.4 Negatively biased InP microdisk modulators

This section reports on the performance of InP microdisk modulators in carrier depletion operation regime, which have been heterogeneously integrated on a SOI waveguide. High-speed operation of the device with a bit-error rate below 1×10^{-9} at data rates of 2.5 Gb/s, 5.0 Gb/s and 10 Gb/s is demonstrated. The performance of the InP microdisk modulators is compared with a commercial lithium niobate modulator. Power penalties are presented and discussed. Finally, the power consumption is calculated and compared with that of state-of-the-art modulators.

7.4.1 Static characteristics

Below the lasing threshold the device can also be used as a carrier-injection-based modulator as presented in section 7.3. Instead of positive bias, here the negative bias regime is of interest. Leakage currents lower than $1 \mu\text{A}$ were sustained for voltages larger than -4 V as shown in Fig. 7.4 a), which displays the I-V curves of more than 30 devices on the same chip.

By biasing the device negatively, the QCSE modulates the absorption [71]. Although the device consists of the same epitaxial material used for

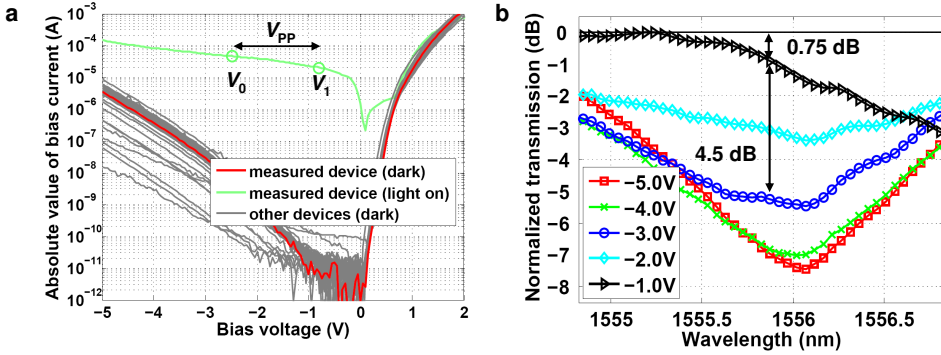


Figure 7.4: a) Static electrical characteristics of the negatively-biased InP microdisk modulator with and without light in the waveguide. The image also displays the dark IV-curves for more than 30 devices on the same chip. b) Static optical characteristics of the InP microdisk modulator. Transmission characteristics of one device for several negative bias voltages.

lasing, the enhancement of the absorption due to the resonant cavity is sufficient to demonstrate the modulation of light. Therefore, processing steps to reduce the band gap of the quantum well, such as quantum-well-intermixing, are not required when co-integrating the modulator with a laser [138]. As operation point for the experiments a wavelength of 1555.8 nm was chosen. Starting from a pre-bias of -1 V the transmission drops by 4.5 dB with a voltage swing of only $V_{pp} = 2.0$ V as displayed in Fig. 7.4. When biasing the device at -5 V more than 6 dB extinction can be achieved. To demonstrate that the modulator could be directly driven by co-integrated electronics the voltage swing was limited to $V_{pp} = 2.0$ V, which is supported by state-of-the-art bipolar complementary metal oxide semiconductor (BiCMOS) technologies commonly used for high-speed optoelectronic circuits [139]. At 1555.8 nm, the additional loss caused by the modulator compared with the off-resonance transmission of the waveguide is only 0.75 dB as shown in Fig. 7.4 b).

7.4.2 Dynamic characteristics

Dynamic measurements were performed to investigate the electro-optic modulation behavior of the modulator under reverse bias conditions. The measurement apparatus is depicted in Fig. 7.5. The sample was mounted on a TEC to stabilize the device temperature at 20 °C. Light from a tun-

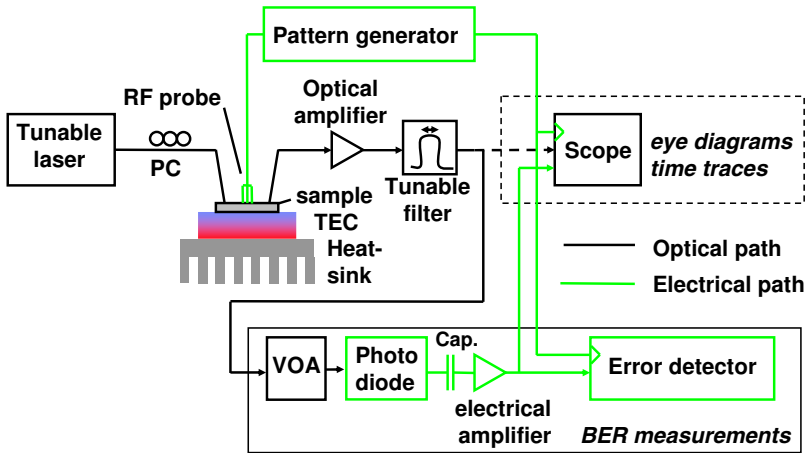


Figure 7.5: Measurement apparatus for high-speed measurements (eye diagrams and BER test).

able laser was fed into a polarization controller (PC) and injected into the chip by grating couplers using a cleaved single-mode fiber. This resulted in -10 dBm optical power in the silicon waveguide. A RF probe was connected to the device and directly driven by a high-speed PPG. The light was then coupled out off the chip by a second grating coupler and amplified by about 30 dB using an EDFA. To measure optical eye diagrams, the light was spectrally filtered using a tunable filter with an insertion loss of 5 dB and a 3 dB-bandwidth of 0.25 nm, and monitored by a high-speed oscilloscope. For measuring BER traces the signal was fed into a variable optical attenuator (VOA), launched into an alternating current (ac)-coupled 10 Gb/s photo receiver and electrically amplified. The electrical signal was then analyzed in a 12.5 Gb/s error detector, which was synchronized with the pulse pattern generator, or monitored in the oscilloscope.

The reference measurements were made with a commercial 40 Gb/s lithium niobate (LiNbO_3) modulator. The optical signal was attenuated to obtain the same power at the input of the EDFA as with the InP microdisk modulator to account for the amplifier noise and evaluate the actual modulator performance.

The operation wavelength was set to 1555.82 nm for all measurements. The InP microdisk modulator was driven with a one-drive-level of $V_1 = -0.875$ V and a zero level of $V_0 = -2.5$ V, resulting in a peak-to-peak swing

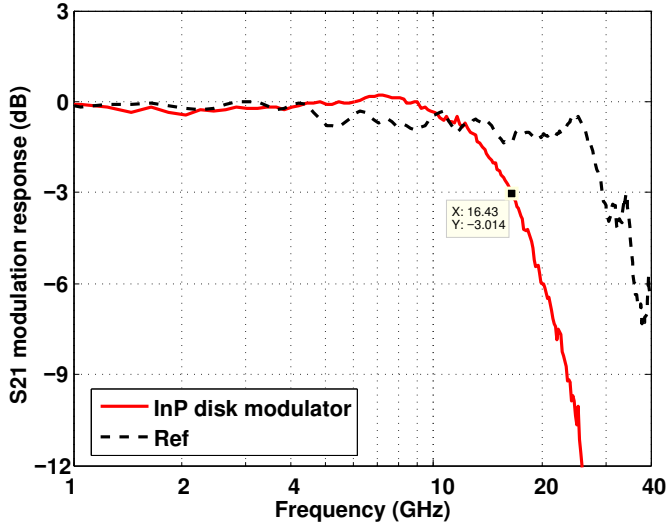


Figure 7.6: Electro-optical small signal bandwidth S_{21} of the negatively-biased microdisk modulator. The broken black lines are reference measured with a commercial 40 Gb/s LiNbO₃ modulator.

of $V_{PP} = 1.625$ V. Figure 7.7 displays eye diagrams for the InP microdisk modulator at 2.5 Gb/s (Fig. 7.7 a)), 5.0 Gb/s (Fig. 7.7 b)) and 10 Gb/s (Fig. 7.7 c)), for NRZ-PRBS lengths of $2^{31}-1$. As can be seen from Figs. 7.7a and 7.7b, the extinction ratio of the InP microdisk modulator was about 4.5 dB for 2.5 Gb/s and 5.0 Gb/s. For 10 Gb/s the extinction ratio degraded to 2.2 dB as shown in Fig. 7.7 c). However, by ac-coupling the photo receiver, the offset was removed, resulting in a clear open eye at 10 Gb/s as evident in Fig. 7.7 d).

The speed limitations of the device originate from the parasitics and are not fundamental to the absorption mechanism [140]. A small-signal 3dB-bandwidth larger than 16 GHz was measured, which is governed by the parasitics of the device as discussed in section 3.3.2. Reducing these parasitics would improve the device speed further to allow for operation at 20 Gb/s and beyond. However, small-signal measurements only give a rough indication about the large-signal behavior of the device.

Therefore, BER measurements were performed to quantify the actual quality of the modulated optical signal. The measurements were carried out at 2.5 Gb/s, 5.0 Gb/s and 10 Gb/s and NRZ-PRBS lengths of 2^7-1

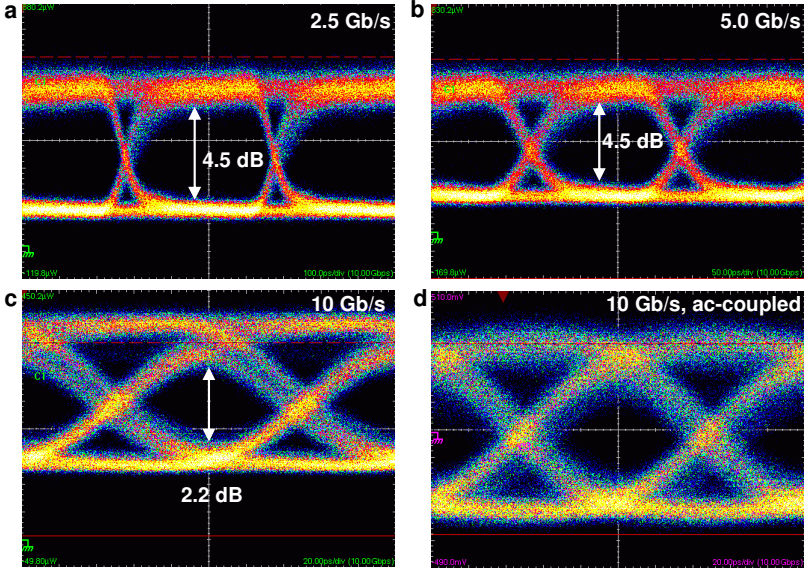


Figure 7.7: Optical eye diagrams of the negatively-biased InP microdisk modulator: a) at a bit rate of 2.5 Gb/s, b) at a bit rate of 5.0 Gb/s. c) at a bit rate of 10 Gb/s, and d) electrical eye at a bit rate of 10 Gb/s and using an ac-coupled photo receiver.

and $2^{31}-1$. Error-free operation ($\text{BER} < 1 \times 10^{-11}$) was achieved for 2.5 and 5.0 Gb/s at a PRBS length of $2^{31}-1$ as shown in Fig. 7.8 a). The power penalty compared with the commercial modulator at 2.5 Gb/s and 5.0 Gb/s was 3.1 dB and is caused by the limited extinction ratio, that can be approximated as [141]

$$P_{\text{dB}} \approx 10 \cdot \left(\frac{\text{ER}_{\text{lin}} + 1}{\text{ER}_{\text{lin}} - 1} \right), \quad (18)$$

where ER_{lin} denotes the linear extinction ratio. For 10 Gb/s the penalty slightly increases to 4.7 dB for a pattern length of 2^7-1 due to the limited extinction ratio of 3.2 dB as evident from Fig. 7.8 b). At a PRBS length of $2^{31}-1$, pattern effects are limiting the extinction ratio to 2.2 dB as indicated in Fig. 7.8 c). resulting in an increased power penalty of 7.0 dB as shown in Fig. 7.8 a). Still, a BER lower than 1×10^{-9} could be achieved for that pattern length. This means that although the modulator exhibits a relatively limited extinction ratio error-free operation at 2.5, 5.0 and 10 Gb/s

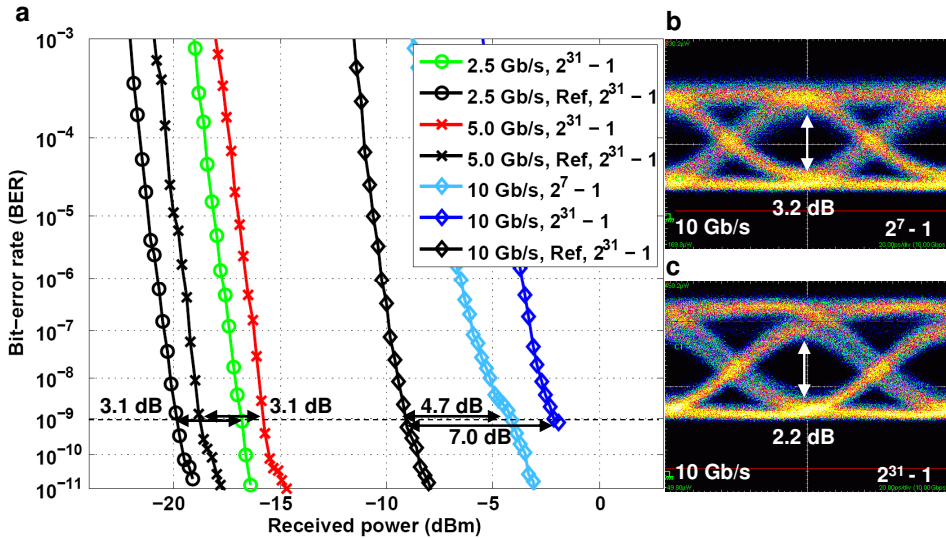


Figure 7.8: a) Bit-error rate measurements of the negatively-biased InP microdisk modulator and a commercial modulator with bit rates of 2.5, 5.0 and 10.0 Gb/s. Eye diagrams for operation at 10 Gb/s and b) a PRBS length of $2^7 - 1$ c) a PRBS length of $2^{31} - 1$.

was successfully demonstrated. The implications of the limited extinction ratio are only an increased power penalty with respect to a modulator with a large extinction ratio. Consequently, a higher laser power would be required in an optical link to obtain the required receiver power to recover the signal error-free. Therefore, it is desirable to improve the extinction ratio to obtain a low-power optical link.

During all measurement an optical signal-to-noise ratio (OSNR) larger than 25 dB is sustained, thus its contribution to the power penalty is not significant. Note that, because of the attenuation of the optical signal and the use of the EDFA, the commercial modulator also requires more than -10 dBm received power at the photo receiver to recover the signal without errors. Without attenuation and successive amplification, a receiver power of -19 dBm was required to obtain error-free operation with the modulator, which is consistent with the datasheet of the photo receiver, not shown in Fig. 7.8 a).

| Publication | Year | Type | V _{pp} | Area | Speed | Static ER | Energy |
|------------------------------|-------------|--------------------|-----------------|--------------------------------------|----------------|---------------|------------------|
| Green <i>et al.</i> [68] | 2007 | MZM | 7.6 V | 1000 μm^2 | 10 Gb/s | 6 dB | 5 pJ/bit |
| Xu <i>et al.</i> [133] | 2007 | Ring | 3.5 V | 310 μm^2 | 10 Gb/s | 6 dB | 5 pJ/bit |
| Lui <i>et al.</i> [136] | 2008 | EAM | 3.0 V | 200 μm^2 | 1.2 GHz | 8 dB | 50 fJ/bit |
| Watts <i>et al.</i> [132] | 2008 | Disk | 3.5 V | 13 μm^2 | 10 Gb/s | 4.8 dB | 58 fJ/bit |
| Dong <i>et al.</i> [142] | 2009 | Ring | 2.0 V | 1000 μm^2 | 11 GHz | 6.5 dB | 50 fJ/bit |
| Dong <i>et al.</i> [143] | 2010 | Ring | 1.0 V | 1200 μm^2 | 10 GHz | 6.0 dB | 10 fJ/bit |
| Watts <i>et al.</i> [16] | 2011 | Disk | 1.0 V | 10 μm^2 | 12.5 Gb/s | 3.2 dB | 3 fJ/bit |
| <i>This work</i> [60] | 2011 | <i>Disk</i> | 1.6 V | 50 μm^2 | 10 Gb/s | 4.5 dB | 56 fJ/bit |

Table 7.1: Comparison of the present work with state-of-the-art modulators in terms of drive voltage, area, speed, static extinction ratio and energy consumption per bit [16].

7.4.3 Energy consumption

The power consumption of a modulator is predominated by ohmic losses and capacitive losses. Typically, in forward-biased devices, which are based on carrier injection, the energy consumption is predominated by the injected current [68]. However, because a negative drive was used, the junctions were reversely biased and the ohmic losses are reduced significantly. The drive currents under external illumination at the one drive level $V_1 = -0.875$ V are $I_1 = 2.1 \times 10^{-5}$ A, and at the zero level of $V_0 = -2.5$ V it is $I_0 = 4.6 \times 10^{-5}$ A, see Fig. 7.4 a). Consequently the energy consumption per bit due to Ohmic losses at a given bit rate (BR) is:

$$E_{\text{bit,curr}} = \frac{1}{2} \cdot \frac{I_1 V_1 + I_0 V_0}{\text{BR}} = 7 \text{ fJ/bit} \quad (19)$$

Note that the static currents were measured with the light in the waveguide thus including the photocurrent, which is generated in the device. In the reverse biased device, the main source of power consumption is energy to charge and discharge the active region capacitance. Fitting the S_{11} parameters with a small-signal equivalent circuit as explained in section 3.3.2, a capacitance of the active region of $C_a = 54.7$ fF has been extracted. A simple plate capacitor model $\tilde{C}_a = \epsilon_0 \epsilon_r \frac{A}{d}$ with a distance of the total undoped layer thickness of $d = 113$ nm resulted in an approximate capacitance of $\tilde{C}_a = 43$ fF, which does not include fringe capacitances. The energy to charge the capacitor is $\frac{1}{2} \cdot CV^2$; for a PRBS stream it is half of that:

$$E_{\text{bit,cap}} = 0.5 \cdot \frac{1}{2} \cdot C_a (V_1^2 - V_0^2) = 49 \text{ fJ/bit} \quad (20)$$

Hence, the modulator requires a total energy of only 56 fJ to process

one bit at 10 Gb/s, when neglecting the power for stabilizing the resonance wavelength. Since most resonant devices are sensitive to temperature fluctuations resulting in wavelength shifts, power to keep them on-resonance is required. The tuning can be realized either by heating or by cooling. Also within heaters and coolers, several techniques exist. Also the temperature stabilization system of the laser could be shared with the modulator and also filters. The energy consumption of the wavelength tuning system strongly depends on the application, the implementation and the system and is therefore not considered here. Table 7.1 compares the operating principle, biasing conditions, area consumption, speed, static extinction ratio, and energy consumption of several high-speed low-power modulator concepts. Extensive research efforts have reduced the energy consumption of modulators from 5 pJ/bit [68] down to single-digit fJ/bit values [16] over the last years. Whereas most devices suffer from limited extinction ratios [16], high drive voltages [68] and a large energy consumption [68, 133], the presented devices represent a good compromise. Moreover, this proof-of-concept study on InP microdisk modulators uses devices that are not fully optimized yet. Especially a reduction of the device diameter, leading to a quadratic reduction of the capacitance, is expected to deliver even higher speed and reduce the energy to the single-digit fJ/bit regime. Also, a reduction in the parasitic pad capacitances is expected to increase the device speed while lowering the total energy consumption leading to ultra-low power high-speed modulators.

7.5 Discussion

Under forward bias it was demonstrated that an InP microdisk heterogeneously integrated on top of a SOI waveguide can be used as an electro-optical modulator. Static electrical and optical performance figures were measured and presented. In the experiments a single InP microdisk modulator has been used as both an inverting and a non-inverting modulator with only 1 V bias, which allows the use of CMOS driver electronics. At 1.0 Gb/s, quasi-error-free operation with a BER lower than 1×10^{-10} was demonstrated for both modes with dynamic extinction ratios of 6 dB and 8 dB for the inverting and the non-inverting operation mode, respectively. Moreover, for the inverting operation mode of the modulator, operation at 2.5 Gb/s with a BER lower than 1×10^{-3} , i.e. below the FEC limit, was achieved. The device investigated in this chapter represents an interest-

ing alternative to state-of-the-art modulator concepts because it combines compactness and very low drive voltage with flexibility in operation. The operation speed of a forward biased modulator is inherently limited by the carrier lifetimes, making this concept unattractive for high-speed operation, unless sophisticated electrical waveforms to drive the device are applied [133]. The advantage of the forward-bias modulation regime is that large extinction ratios can be achieved with low drive voltages. This may be beneficial for applications, where the voltage swing is limited.

For high-speed operation the negative bias regime is much more attractive as the charge carriers generated by absorption can be efficiently transferred to the contacts using the applied voltage and/or electric field. Making use of this operation mode, the modulation characteristics of a reversely biased InP microdisk modulator heterogeneously integrated on top of a SOI waveguide were reported. Static extinction ratios of 4.5 dB for a bias swing of only $V_{pp} = 2.0$ V were presented. Bit-error rates at 2.5 Gb/s, 5.0 Gb/s and 10.0 Gb/s were measured to investigate the signal quality of the modulation process. Operation with a BER lower than 1×10^{-9} was successfully demonstrated for data rates up to 10 Gb/s. The performance was analysed with respect to a commercial modulator and power penalties of about 3.1 dB for 2.5 Gb/s and 5 Gb/s due to the limited extinction ratio were found. For 10 Gb/s the power penalty was 4.7 dB for a pattern length of 2^7-1 , whereas for $2^{31}-1$ the penalty was 7.0 dB. The reduced extinction ratio at high speed and long patterns was found to be the main source of the power penalty.

The results presented here demonstrate the applicability of InP microdisks as high-speed electro absorption modulators in the carrier depletion operation regime. Drive voltages of $V_{pp} = 2.0$ V can easily be achieved by state-of-the-art BiCMOS technologies [63, 64]. The energy consumption of 56 fJ/bit of the presented device is comparable to fully optimized state-of-the-art modulators. The device combines low footprint and high operation speed. This together with the possibility of co-integrating lasers, wavelength converters and detectors using the same epitaxial material and the same processing scheme, make the presented modulator very attractive for integrated photonics. The operation speed of the device can be improved by reducing the parasitics and by reducing the series resistance of the device limiting the electric field required for removing the absorbed charge-carriers. To reduce the observed power penalty the extinction ratio

of the modulator needs to be improved. This can be achieved by growing a larger number of quantum wells to improve to overlap with the optical mode. Also, the coupling between waveguide and microdisk can be optimized towards critical coupling, which in turn, however, would reduce the optical bandwidth of the device. Also, when using the device under forward bias, the lasing properties may be compromised resulting in a trade-off between modulation and lasing properties.

8 Improving the Performance of InP Microdisk Lasers

The present chapter discusses ways how to improve the performance of InP microdisk lasers, in particular how to improve their lasing properties. Ways how to solve the alignment issue and how to improve the output power are discussed. Also, an advanced coupling scheme on how to improve the SMSR is presented. Measures on how to improve the performance of InP microdisk-based modulators and detectors are then discussed. The grating couplers used in this work partially limited the measurements of the MDLs because of the small bandwidth and relatively low efficiency. Therefore the design and fabrication of advanced grating couplers is discussed at the end of this chapter. The improved grating couplers are to be seen as measures to improve the usability of the InP microdisks. Parts of this chapter are based on scientific publications^{16,17}.

8.1 Output power and coupling

The output power of microdisk lasers is governed by numerous factors discussed in chapter 3. The following factors and/or parameters have direct influence on the output power of the device.

The alignment of the InP microdisk towards the waveguide is critical and significantly influences the lasing properties. To achieve precise alignment either steppers / scanners or electron beam lithography may be employed.

For the given material structure with the parameters given in table 3.1, the output power vs. the electrical pumping current I has been calculated with the static single-mode model given in section 3.2.1. As shown in Fig. 8.1 coupling constants $\alpha_c \leq 15 \text{ cm}^{-1}$ correspond to a too weak coupling between microdisk and waveguide. As the coupling constant is decreased, i.e., the coupling thickness increased, the output power gradually drops as fewer power is coupled out from the MDL to the waveguide. The total coupling thickness may comprises both adhesive bonding layer, typically

¹⁶J. Hofrichter *et al.*, Gating Couplers as Optical Probe Pads in a Standard CMOS Process, *IEEE Group IV Photonics Conference*, London, United Kingdom, P1.24, (2011).

¹⁷S. Assefa *et al.*, A 90nm CMOS Integrated Nano-Photonics Technology for 25Gbps WDM Optical Communications Applications, *International Electron Devices Meeting (IEDM 2012)*, San Francisco, USA, Post-deadline paper, (2012).

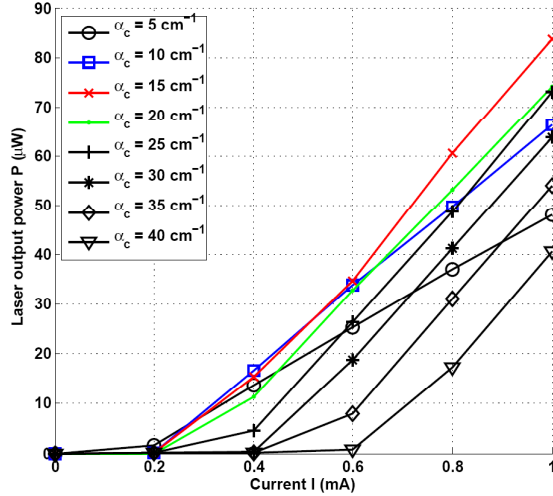


Figure 8.1: Optical output power of an InP MDL for different coupling coefficients α_c under continuous electrical bias.

BCB, and also an adhesion promoting layer on the InP, such as silicon dioxide. For coupling constants $\alpha_c \geq 25 \text{ cm}^{-1}$ the output power also drops as more photons are coupled out before being re-amplified inside the cavity. This case corresponds to a too strong coupling, potentially caused by a too low coupling layer thickness. The optimum was found to be at $\alpha_c \approx 15 \text{ cm}^{-1}$ where the output power exceeds $84 \mu\text{W}$ in the waveguide for a pumping current of only 1 mA. Note that the calculation refers to *waveguide power*, whereas the power levels stated in chapter 3 refer to *fibre-coupled power* and are thus about 6-10 dB lower due to the grating coupler losses. This indicates that by appropriate design of the coupling between waveguide and cavity the output power can be substantially increased while maintaining a low threshold current. The microdisk lasers measured in section 3.3.1 are too weakly coupled as they exhibit a low threshold current and a low output power at the same time.

The optimal coupling constant α_c that guarantees the maximal output power for a desired bias point can then be used to compute the optimal BCB or coupling layer thickness. The coupling constant can be converted into an equivalent quality factor [96]:

$$Q_c = \frac{2\pi n_g}{\alpha_c \lambda_0} \quad (21)$$

Then, 3D FDTD calculations were performed on the cavity structure including the top and bottom contact metal to account for absorption losses to compute both the intrinsic, i.e., *unloaded* quality factor Q_i of the cavity and the *loaded* quality factor Q_l with the waveguide coupled to the device. Here, it was found to be crucial to compute the correct mode in the cavity.

- **The optical mode must be the actual dominant lasing mode.**
- **The optical mode must couple to the waveguide.**

It is important to stress that not every reduction of the cavity- Q is identical to efficient waveguide coupling, a fact which is commonly overlooked in the literature [96, 144]. It is not trivial to identify the correct lasing mode: Because the cavities investigated in this thesis have a total height of 583 nm they are multi-modal in the vertical direction. Also, the top-contact requires a clearance of $\approx 1 \mu\text{m}$ to the perimeter of the disks as discussed in section 8.2, resulting in radial multi-mode behaviour. Furthermore, the gain spectrum is broader than the free-spectral range of the microdisk cavities resulting in longitudinal multi-modal behaviour.

In light of the variety of modes simple 2D approaches and also 3D FDTD approaches, in which the coupling of waveguide modes to the cavity instead of the coupling of lasing modes to the waveguide are computed to save computation time [144], are clearly insufficient and only fully-vectorial 3D FDTD approaches [145], in which the cavity modes are computed and the coupling towards the waveguide is computed, are able to yield accurate results.

After having identified the correct lasing mode the vertical distance between the waveguide and the disk was varied and the loaded quality-factor Q_l was computed. The corresponding ideal coupling-factor Q_c can then be computed according to equation (22) to extract the ideal coupling or bonding thickness [146]:

$$Q_c = \left(\frac{1}{Q_l} - \frac{1}{Q_i} \right). \quad (22)$$

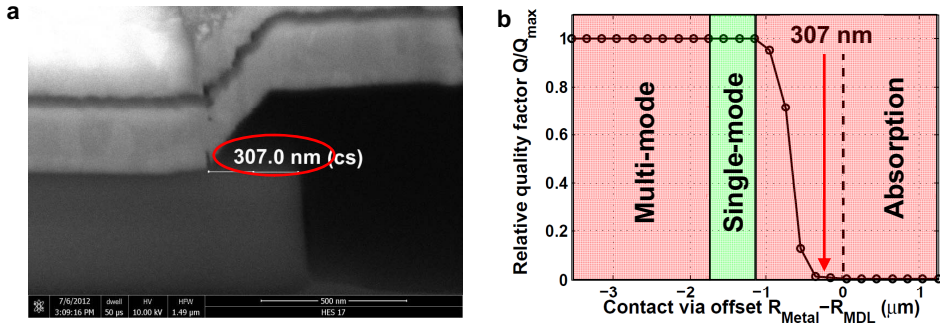


Figure 8.2: Effects on optical properties of via opening: a) SEM image of a FIB-cross section of an InP microdisk with a via that is too close to the edge, or too large. b) Influence of metal absorption on the quality factor Q of the fundamental mode. The distance of the metal of the left image is indicated.

8.2 Influence of top via on Q -factor

Alignment of top contact It was found in this work that not only the alignment towards the waveguide is critical, but also the positioning of the top contact via with respect to the perimeter of the disk.

During the fabrication of the InP microdisks a top contact has to be applied. As described in section 2.6 after structuring the InP disks or rings and subsequent cladding of the devices with either a polymer (BCB or polyimide) or silicon dioxide, openings in the cladding layer, i.e., vias need to be patterned. Different methods to open the top contact via have been investigated. First, a negative tone photoresist has been used, that, however, resulted in an increased size of the via with respect to the design and the photo mask. Although this does not affect electrical performance and even resulted in up to 95% electrically working disks per chip, a too large via does indeed compromise the optical properties of the device. The modes propagating in the device are whispering gallery modes propagating close to the perimeter of the cavity. When the top metal contact is either too close to the edge, or too large, the absorption of the metal starts to quench the optical modes.

To investigate this effect more closely 2D FDTD simulations have been performed in MIT electromagnetic equation propagation (MEEP) [145]. Because the interface between the InP disks or rings with the top contact consists of titanium, this metal has been used in the simulations and was

implemented with a Drude model [147, 148]. Fig. 8.2 a) shows an SEM image of a FIB cross-section through the centre of a microdisk with $7.5 \mu\text{m}$ diameter fabricated using negative tone photoresist for the top via opening. For this device the alignment accuracy was excellent, but the size of the top contact via was too large so that the metal inside the via is as close as 307 nm to the edge of the disk. Fig. 8.2 b) shows the simulation results obtained for the fundamental mode inside a disk with a varying top via diameter filled with metal. It is evident that a clearance of at least $1.1 \mu\text{m}$ is to be sustained to prevent absorption-induced reduction of the Q -factor. A metal-to-edge clearance of more than $1.7 \mu\text{m}$ would result in radial multi-mode behaviour as shown in Fig. 3.3 and is also not desirable. The annotations in Fig. 8.2 b) also show that the metal-to-edge offset of 307 nm results in a significant reduction of the Q -factor strongly reducing the output power of this particular device. This simulation demonstrates that not only an accurate alignment is required to obtain high- Q cavities, but also the size of the top contact via is to be controlled precisely. To account for this an image reversal process was used as described in section 2.6 allowing to accurately tune the size of the via, and also to obtain a process margin for misalignment by tuning the lithography process to obtain an appropriately sized top contact via opening as shown in Fig. 8.2 b).

8.3 Side-mode suppression ratio

The side-mode suppression ration of the InP microdisk lasers investigated in this thesis was typically in the order of 20-30 dB as reported in section 3.3.1. The short coupling lengths of the investigated devices resulted in coupling conditions that support several modes per FSR. Moreover, the SMSR was limited because the coupling was also supporting the modes with wavelengths $\lambda_0 + \text{FSR}$ and $\lambda_0 - \text{FSR}$.

By increasing the coupling lengths these modes can be effectively suppressed as the group index difference results in a substantial phase difference after a longer propagation lengths. Fig. 8.3 shows such an implementation, where the silicon waveguide was meandered around the disk cavity to increase the coupling lengths and achieve the described mode-filtering functionality.

The measurements carried out on this device geometry are displayed in Fig. 8.4. The intensity of the central lasing mode at $\lambda_0 = 1559 \text{ nm}$ was -26 dBm. The side-modes at $\lambda_0 - \text{FSR} = 1528 \text{ nm}$ and $\lambda_0 + \text{FSR} = 1591 \text{ nm}$ had

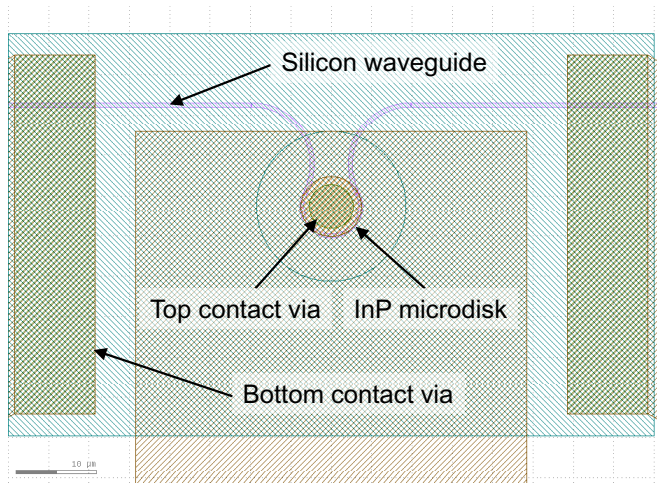


Figure 8.3: An InP microdisk with improved coupling. The coupling length of the waveguide is increased by meandering the waveguide around the disk cavity.

an intensity of -62 dBm and -64 dBm, respectively, resulting in a side-mode suppression ratio of 36 dB. Typical disk lasers without meandering waveguide exhibited a SMSR of about 30 dB. The improvement demonstrates the feasibility of the described approach to enhance the spectral purity of microdisk lasers.

It is therefore recommended to increase the coupling distance between microdisk cavity and waveguide in order to enable a longer coupling length for a given fixed coupling constant not to alter the threshold current and slope efficiency of the lasers.

8.4 Enhancing the device speed by reduction of electrical parasitics

The speed of the InP microdisk lasers is governed by current flowing through the active region in which the emission takes place. Internal and external parasitics of the device influence the current distribution of the high-frequency electrical signal when the laser is driven at high speed. The parasitics of the device have been discussed and extracted in section 3.3.2 according to the SSEC shown in Fig. 3.11. The current contributing to the lasing emission is the current flowing through the active region of the active region of the laser diode. By analysing the ratio of the current through

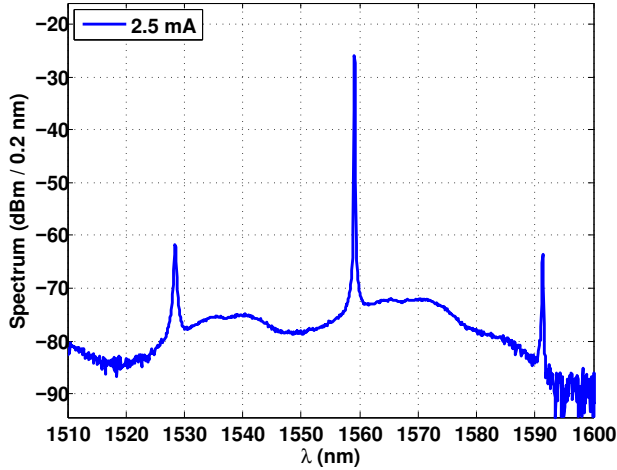


Figure 8.4: Lasing spectrum of an InP microdisk with improved coupling by meandering the waveguide around the disk cavity. The bias current was 2.5 mA resulting in a lasing power -26 dBm of the central mode at 1559 nm. The SMSR was determined to 36 dB.

the active diode region I_{Diode} with respect to the applied total small-signal current I_{Total} the speed limitations of the device induced by internal and external parasitics can be investigated. The 3dB-roll-off frequency was investigated as a measure of the device speed.

The speed limitations of an InP microdisk laser with a diameter of 15 μm were analysed. The parasitics of the device extracted in section 3.3.2 were the series resistance $R_s = R_{s,0} = 26.6 \Omega$, the capacitance of the active region $C_a = C_{a,0} = 153.1 \text{ fF}$, the resistance of the active region including the total epitaxial layer stack $R_a = R_{a,0} = 181.8 \Omega$ and the external parasitic capacitance $C_a = C_{a,0} = 310 \text{ fF}$ including pad- and wiring-capacitances. These initial values were varied systematically to analyse their impact on the device performance and possible improvements in the operation speed.

First, the influence of the pad capacitance C_p and of the series resistance of the device including metal the wiring resistance, the metal-semiconductor and the semiconductor-metal contact resistance. Fig. 8.5 shows the frequency response of the diode-current-to-total-current ratio as a function of the small-signal operation frequency. The original device had a 3dB-bandwidth of 3.1 GHz (red curve), which can be improved slightly to 3.3 GHz by reducing the series resistance of the device by factor of two

(light green curve). This can be achieved, e.g., by using larger contact vias, increasing the bottom contact island thickness, or by increasing the doping and thus the conductivity of the bottom contact island. Moreover, the series resistance can be reduced by forming nickel-InP alloys [149]. A larger impact on the device speed has the pad capacitance. By reducing the pad capacitance by a factor of 2 the 3 dB-bandwidth can be increased to 4.7 GHz (dark blue curve). When applying both optimizations the speed of the investigated microdisk laser with $15\mu\text{m}$ diameter can be increased to 4.8 GHz (cyan curve), which enables the use of the device for direct modulation at 5 Gb/s.

By reducing the active region capacitance C_a by a factor of two the device speed can be increased from 3.1 to 3.9 GHz as shown in Fig. 8.6 (light green curve). A larger improvement was observed when reducing the resistance of the epitaxial layer stack R_a . When decreasing R_a to half of its original value a bandwidth of 10 GHz is observed (dark blue curve). By implementing both changes at the same time the 3dB-bandwidth of the current-ratio is boosted to 19.8 GHz. However, it is likely that devices under forward bias cannot be operated at this speed as the device dynamics will be dominated by relaxation oscillation effects.

The same analysis was performed with a microdisk laser with $7.5\ \mu\text{m}$ diameter. Fig. 8.7 displays the original 3dB-bandwidth of 4.5 GHz (red curve). By reducing the series resistance to half of its original value the bandwidth can be improved to 5.1 GHz (green curve). The device speed can be improved to 7.8 GHz when decreasing the external pad capacitance by a factor of two (dark blue curve). When implementing both improvements the 3dB-bandwidth can be increased to 8.6 GHz enabling directly driven InP microdisk lasers at 10 Gb/s. It is noteworthy, that the change of the current ratio with frequency of the unoptimized microdisk laser with $7.5\ \mu\text{m}$ diameter is relatively shallow. This in turn means that also small variations in the diameter of the disk, in local changes of doping concentrations, etc., may result in a significant change in bandwidth. In this context it should be mentioned that for the same device geometry devices have been measured with small-signal S_{21} -bandwidths ranging from 2.5 GHz up to 12 GHz, of which the latter was the highest bandwidth measured during the experiments.

Fig. 8.8 displays the parameter for the active region capacitance C_a and the active region resistance R_a . By reducing capacitance of the active

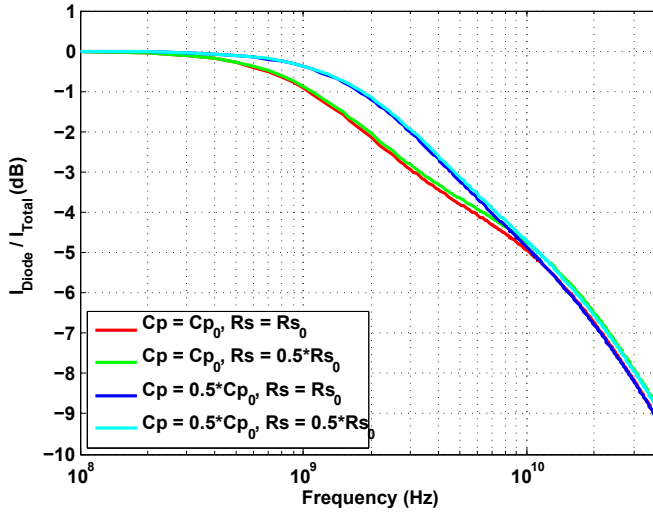


Figure 8.5: Parameter variation analysis of an InP microdisk laser with $15 \mu\text{m}$ diameter. The parasitic pad- and wiring-capacitance C_p and the series resistance of the device R_s were varied with respect to the original extracted values $C_{p,0}$ and $R_{s,0}$ presented in section 3.3.2.

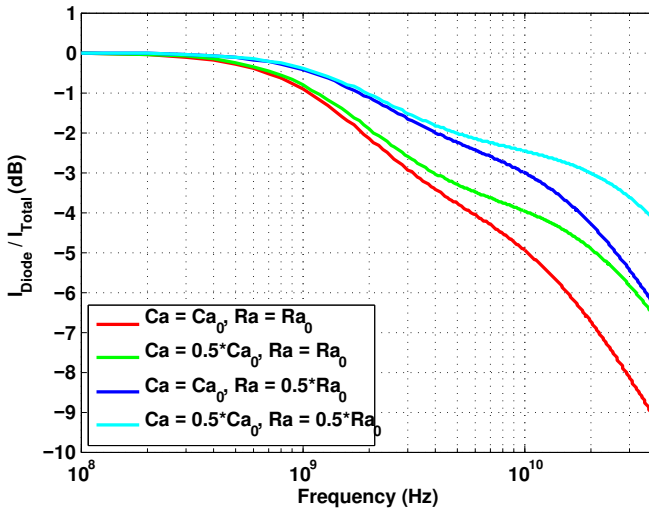


Figure 8.6: Parameter variation analysis of an InP microdisk laser with $15 \mu\text{m}$ diameter. The active region capacitance C_a and resistance of the active region of the device R_a were varied with respect to the original extracted values $C_{a,0}$ and $R_{a,0}$ presented in section 3.3.2.

region, which corresponds to a further reduction in diameter, the device speed can only be improved from 4.5 GHz (red curve) to 4.8 GHz (green curve). By decreasing the resistance of the active region to half of its original value large increase of the bandwidth to 40 GHz was observed (dark blue curve), which can be raised even further by reducing the capacitance C_a simultaneously.

Although bandwidths in excess of 40 GHz have been suggested by the presented small-signal analysis, these bandwidths are not realistic as in lasers relaxation oscillations play an important role, which typically limit the device speed to about 10 GHz when using direct modulation. These investigations are therefore to be seen as design guidelines for large microdisk lasers with diameters larger than 10 μm for which the device speed is clearly limited by the parasitics. Although smaller lasers may operate faster than large disk lasers, the latter devices may also be of interest as they emit more optical output power, which may be favourable.

In conclusion, also microdisk lasers with diameters larger than 10 μm may be operated at high speed when reducing the resistance of the active region. This may be achieved by reducing the resistance of the tunnel junction, e.g. by forming more abrupt interfaces or by introducing a background-doping in the barrier regions.

8.5 Epitaxial material

The used epitaxial material contains three strained InAsP quantum wells, in which the light emission takes place [13]. For this particular material it is well-known that the photon emission process is very temperature dependent and lasers fabricated using this material system suffer from thermal instability.

A future direction for the research on InP microdisk lasers may therefore be directed towards improving the quantum well material. Besides a study on the barrier height defining the thermally-induced exciton escape rate from the quantum wells, also a study on the quantum well material is highly recommended. For example by implementing quantum wells using the GaInAs/AlInAs material system the thermal stability of the lasers can be largely improved [150].

Another approach to improve the thermal stability of lasers is the implementation of quantum dots as the active lasing material. Although the most promising results have been reported on InGaAs/GaAs-based quan-

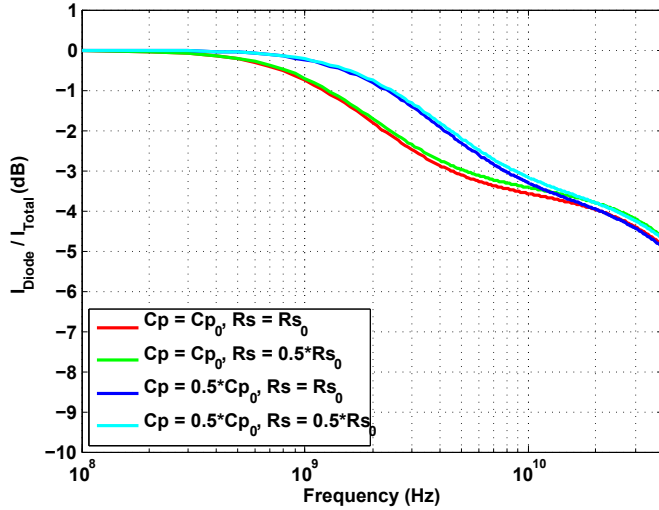


Figure 8.7: Parameter variation analysis of an InP microdisk laser with $7.5 \mu\text{m}$ diameter. The parasitic pad- and wiring-capacitance C_p and the series resistance of the device R_s were varied with respect to the original extracted values $C_{p,0}$ and $R_{s,0}$.

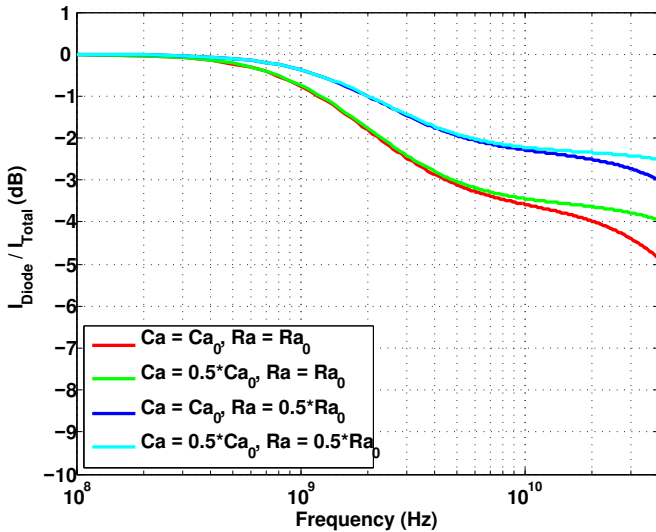


Figure 8.8: Parameter variation analysis of an InP microdisk laser with $7.5 \mu\text{m}$ diameter. The active region capacitance C_a and resistance of the active region of the device R_a were varied with respect to the original extracted values $C_{a,0}$ and $R_{a,0}$.

tum dots emitting around 1300 nm [151], the results are promising as lasing operation in excess of 200 °C was recently demonstrated [152].

8.6 Grating couplers

Grating couplers were used in this work for fibre-to-chip coupling. They were used in the experiments to measure and evaluate the on-chip devices, i.e., the electrically contacted InP microdisk. Therefore the performance of the grating couplers is strongly influencing the measurements. This section describes the figures-of-merit of the grating couplers used in this work and how to improve their performance. Therefore this section is not discussing ways *how to improve the performance* of microdisk lasers, but instead discusses measures *how to improve the usability and how to facilitate the measurement* of on-chip optical components.

Grating couplers used during MDL-experiments The grating couplers used in this work were the standard grating couplers being included in the design tutorial [33]. They consist of a partially etched grating coupler with a 250 μm long parabolic taper. The grating coupler ridges were partially etched with an etch depth of 70 nm and a period of 630 nm. The grating couplers are centred around 1550 nm and are designed to operate at a coupling angle of 8° from the surface normal [33]. The peak efficiency of the grating couplers was found to be between -6 and -8 dB, varying from SOI fabrication run to run.

These grating couplers were used as standard means of optical measurements, but it was found very soon that the performance of the gratings was not ideal for the following reasons:

- The standard grating couplers have a relatively high back-reflection of circa -20 dB, which is translated to a ripple in the frequency response of the grating couplers. These reflections impair passive transmission measurements through the silicon waveguides. These reflections also cause bi-stable devices such as optical flip-flops [51] by reverting the operation direction or becoming unstable.
- The centre wavelength of the gratings was designed to be 1550 nm, which was also the peak of the PL spectrum of the epitaxial material. When electrically pumping the material the electronic bands are

tilted resulting in a reduction of the band-gap, which corresponds to a red-shift of about 30 nm of the lasing spectrum with respect to the PL spectrum as discussed in section 2.5. At the resulting lasing wavelength of 1580 nm the grating coupler efficiency is about 6 dB to 8 dB lower resulting in about 12 dB to 16 dB insertion loss on either side. Therefore it is desirable to have gratings centred at around 1580 nm, or designed for operation at a larger off-axis angle and operated at a smaller angle, resulting in the desired red-shift of the coupling curve.

- The 3dB-bandwidth of the standard grating couplers was about 50 nm, which is sufficient for C-band operation. However, as mentioned above, the majority of the devices were operating at around 1580 nm or even larger wavelengths. Either the above mentioned changes could be implemented, or ways to increase the bandwidth to reduce the roll-off of the grating couplers for larger (and also smaller) wavelengths.
- Most grating couplers measured had a peak coupling efficiency of -8 dB to -6 dB. Although this coupling efficiency is sufficient for device characterization, where a laser operated at relatively high power (of about 0 dBm) is located outside the chip, this coupling loss is problematic when measuring the InP microdisks operated as on-chip lasers. The reason is the limited receiver sensitivity at high speeds. E.g., for a positive intrinsic negative (PIN) diode based receiver a receiver power of -18 dBm at 10 Gb/s is required to detect an optical signal without errors [141]. These are typical power levels at which a microdisk laser emits, thus the mentioned coupling losses complicate high-speed measurements and should be further reduced.

All the aforementioned aspects resulted in challenging measurements, which would have been much more relaxed if grating couplers with an improved efficiency, or at least a larger bandwidth would have been used. Also, the footprint of the used grating couplers partially determined the physical layout of the designs.

Improved grating couplers Based on the drawbacks of the standard grating couplers discussed above, ways to improve the coupling performance, in particular in the aspects mentioned above, are discussed. The

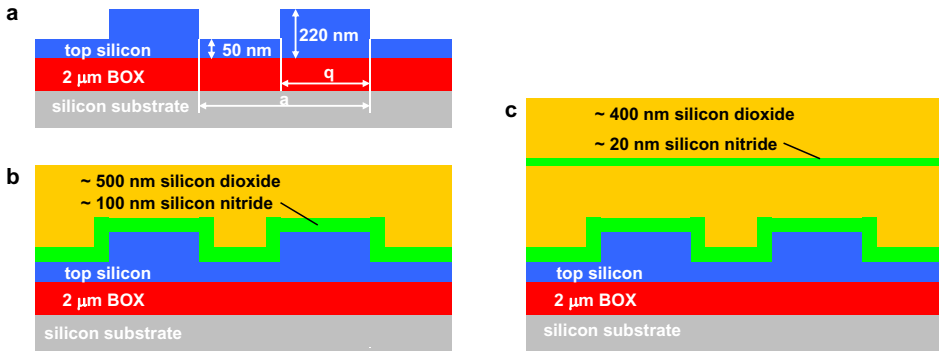


Figure 8.9: Cross-section of the investigated partially etched grating couplers. a) Cross section after structuring the FEOL by partially etching to form the grating teeth and fully etching to form the waveguides. b) Cross-section after cladding the grating couplers capped with a silicon nitride layer and subsequent first metal oxide (M1) planarized oxide. c) Cross-section of the layer stack after completing all process steps. Note that only layers influencing the optical performance of the grating couplers are shown for sake of clarity.

available technology allowed the fabrication of partially etched grating couplers with the cross-sections shown in Fig. 8.9. First, the front-end-of-line (FEOL) is structured by fully etching the SOI waveguides and partially etching the grating teeth as illustrated in Fig. 8.9 a). Then the grating teeth were cladded by a thin silicon nitride film and a thick planarized oxide, see Fig. 8.9 b). Finally, the whole CMOS process was finalized including the numerous FEOL layers. Fig. 8.9 c) displays the optically active layers, which determine the performance of the grating couplers.

To enable a fast and accurate simulation of the grating couplers a two-stage simulation approach was used [62]. First, the eigenmodes of a single grating tooth with periodic boundary conditions, representing an infinite grating, have been calculated using the free toolkit MIT photonic bands (MPB) [153], which is a fully-vectorial eigenmode solver of Maxwell's equations with periodic boundary conditions [153]. The computed eigenvalues, i.e., the computed frequency of the eigenmodes, are solutions of a scale invariant problem and need to be translated into the grating period by scaling the problem to the desired wavelength or frequency. These solutions were then analysed using Meep, a fully-vectorial 3D FDTD solver for Maxwell's equations [145]. Because the grating coupler ridges can be assumed to have

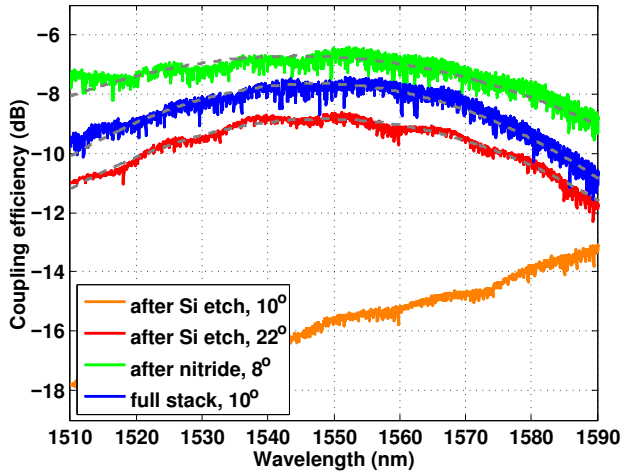


Figure 8.10: Partially etched grating couplers for wafer-scale testing throughout the fabrication of a CMOS process.

a constant index of refraction orthogonal to the propagation direction of the light (i.e. along the grating teeth), 2D FDTD simulations were carried out to calculate the spectral response of the gratings and to select the correct solutions of the calculated eigenmodes, which are computed because MPB cannot differentiate between positive and negative k-vectors, i.e., coupling angles. The source is a matched Gaussian waveguide-mode located on the left-hand side in the silicon waveguide. After propagating through the grating the emitted power is calculated in a flux plane located in the core of the single mode fibre on the upper right side.

A first set of these grating couplers was fabricated using IBM’s silicon integrated nanophotonics platform [38]. This process combines both optical and electrical functions on one wafer. Consequently, the optical devices have to fulfil the DRC of the electrical components, and also have to share the same processing modules. A key benefit of the grating couplers compared to edge-coupling is the possibility to couple light vertically off the chip lending these devices to wafer-scale characterization [62]. Furthermore, because the grating couplers are structured at the beginning of the FEOL processing, they can also be used as optical probe pads to monitor the device performance of photonic devices throughout the entire CMOS fabrication process. Fig. 8.10 displays the coupling performance of partially etched grating couplers fabricated in a CMOS process at dif-

ferent stages of the fabrication. The grating couplers have been designed to operate at 1550 nm at a coupling angle of 10° when all layers including the back-end-of-the-line (BEOL) are applied. When defining the transistors and the waveguides in one of the first processing steps no cladding is present resulting in a strong red-shift of the coupling curve, which can be compensated by increasing the coupling angle to 22° . After deposition of the silicon nitride passivation layer on top of the FEOL the coupling curve is blue-shifted and the grating can be used at a more moderate coupling angle of 8° . The grating coupler can be used for wafer-scale characterization of the completed wafer including all films at the designed angle of 10° . Compared to the coupling efficiency including only the nitride passivation layer the coupling efficiency is slightly reduced due to interference effects in the mainly dielectric BEOL films.

After this first demonstration of grating couplers in a standard CMOS process further efforts were made to improve the grating couplers in two aspects: First of all, the footprint is to be reduced to minimize the area overhead of these photonic probe pads compared to the actual photonic circuits. Secondly, also the residual ripples stemming from the end-facets of the grating couplers are to be reduced to improve quality of the coupling spectrum to enable accurate characterization of, e.g., WDM devices, and also to prevent unwanted mode flipping in bi-stable optical elements, such as microdisk laser based all-optical flip-flops [51].

In order to reduce the footprint of the grating couplers the taper was integrated into the grating to form a focusing grating, where the grating ridges are located on an ellipse having one focal point at the taper-to-waveguide junction [154, 155]. Note that for perfect vertical coupling, the ellipse is reduced to a circle. The resulting focusing grating has a total length of about $30 \mu\text{m}$ and a total width of about $18 \mu\text{m}$ thus reducing the footprint by a factor of 16 compared to linear tapers and by a factor of 8 compared to parabolic tapers.

Anti-reflection wedges have been designed to reduce the ripples in the grating spectrum caused by the reflection of light at the rear facet of the grating. 3D FDTD simulations in Meep [145] have been performed for different lengths and widths of the taper obeying a DRC clean design. A wedge with a length of $2 \mu\text{m}$ and a starting width of 500 nm was computed using 2D FDTD to have a residual reflection of less than 0.5 % and was implemented into the grating design as shown in Fig. 8.11 a). This particu-

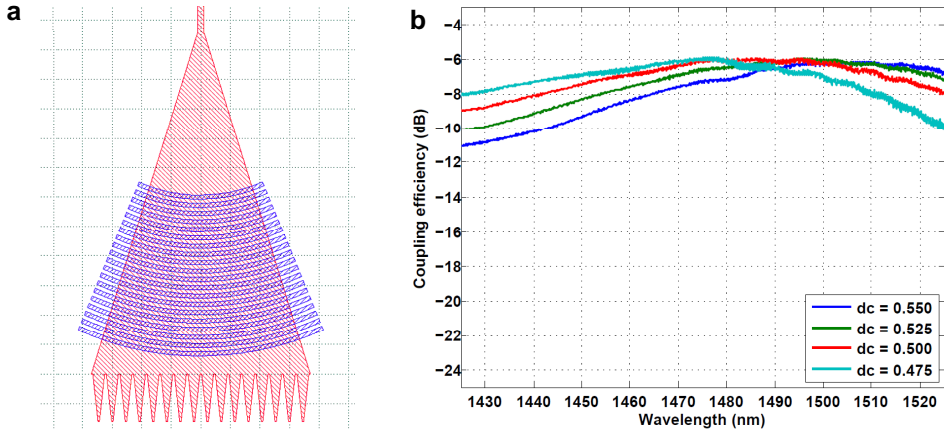


Figure 8.11: Partially etched focusing grating couplers. a) Print-screen of GDSII layout. b) Measurement of a partially etched focusing grating coupler with varying duty cycle dc . The period is fixed with $p = 720$ nm.

lar grating coupler was designed for applications in the tele-communication S-band and is thus centred around 1490 nm as shown in Fig. 8.11 b). The gratings have an efficiency of about -6 dB (25 %) and a 3dB-bandwidth larger than 110 nm, combined with less than 0.2 dB peak-to-peak ripple clearly excelling the performance of the standard grating couplers in terms of footprint, bandwidth and ripple. These partially etched focusing grating couplers have a period of $p = 720$ nm and are fabricated using the fabrication process reported in [156].

Also, an index matching liquid may be applied between the cleaved fibre facet and the grating coupler to improve the performance further. This way, the residual back-reflection between the fibre facet and the grating can be eliminated. We used glycerine as index matching liquid because of easy handling and its wetting properties, which allow the drop of glycerine to be transported over the chip by scanning the fibre, to which it is attached. Fig. 8.12 displays the measured coupling performance for grating couplers with a duty cycle of 0.5 with varying periods. The width of the silicon ridges and the trenches was designed to be identical for easier metrology and fabrication. Adding glycerine does not only reduce the ripples below 0.05 dB peak-peak, which is limited by intensity noise of the super-luminescence light-emitting-diode (SLED) used for the characterization, but improves

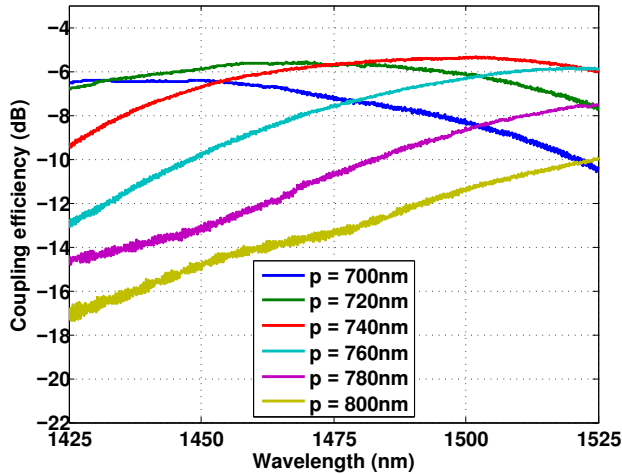


Figure 8.12: Spectral response of the improved grating couplers when using an index-matching liquid.

also the coupling efficiency resulting in -5.3 dB (29.5 %) peak coupling efficiency and an increased 3dB-bandwidth of 130 nm for a device with a period of 740 nm.

The presented approach demonstrates a clear path towards compact high-performance grating couplers meeting the requirements for wafer-scale testing of on-chip optical components. Furthermore, the design is fully CMOS compatible and can be integrated into purely photonic fabrication processes [31, 37] and also into standard CMOS fabrication process containing both optical and electrical components [156].

8.7 Discussion

This chapter discussed numerous aspects in which the performance and also the usability of InP microdisk lasers can be improved. By implementing all the changes discussed in this chapter, it is expected that the devices will have a wall-plug efficiency in the percent range while operating at 10 Gb/s and beyond, have a largely improved side-mode suppression ratio, improved thermal stability and can be characterized and used for on-chip experiments at lasing wavelength span of more than 100 nm.

First, the static single-mode microdisk laser model developed in chapter 3 was employed to analyse the influence of the coupling coefficient on the laser output power and the threshold current. It was found that by accurately tuning the coupling constant α_c it is possible to substantially increase the laser output power while leaving the threshold current largely unchanged.

It was then discussed that the waveguide has a substantial influence on the lasing modes in the disk cavity as coupling losses and scattering losses induced by the waveguide serve as filter for certain optical modes. Therefore, the lasing modes inside the cavity can only be identified when including the waveguide in the calculations. The coupling constant of the lasing modes can then be calculated by a reduction of their respective quality factor Q induced by the waveguide.

Although the alignment of the waveguide is critical for the lasing performance of the devices, it was found that the positioning accuracy and size control of the top contact via opening has an equivalently important role in defining the laser performance. It was found that a clearance of at least $1\ \mu\text{m}$ of the metal to the disk perimeter has to be sustained to not reduce the quality factor of the fundamental lasing mode.

During the experiments described in chapters 3 and 5 it was found that the laser has a limited side-mode expression ratio, which may be used beneficially for, e.g., wavelength conversion [53, 56]. However, when using the device as a laser source a high side-mode suppression ratio is required, which can be achieved by implementing a meandering waveguide in the coupling section. A side-mode suppression-ratio of 36 dB was demonstrated. Also, higher-order optical modes were suppressed resulting in an improved lasing spectrum.

The speed of the devices was found to be determined by their parasitics as discussed in section 3.3.2. The device speed of InP microdisk lasers

can be improved by reducing the active region capacitance of the device, which can be achieved by reducing the diameter. Also, instead of a disk the cavity may also be formed as a ring. Moreover, the speed can be slightly improved by reducing the external parasitic capacitances formed between the metal wiring and the bottom contact island layer. This can be achieved by using a thicker cladding layer for instance. The largest influence on the device speed has the resistance of the active region, i.e., of the epitaxial layer stack. The resistance can be reduced by improving the abruptness of the tunnel junction doping regions or by introducing a background doping in the barrier regions. By implementing this improvements it is expected that InP microdisk lasers may be directly modulated with data rates in excess of 10 Gb/s.

Further improvements of the laser can be implemented by adjusting the epitaxial layer stack. On one hand, the barrier heights may be adjusted to reduce the thermally-induced charge-carrier escape-rate. On the other hand, the light emitting material, namely the quantum wells may be changed to more temperature-stable alternatives. For instance aluminium-containing alloys or quantum wells may be implemented.

The fibre-coupling method using grating couplers was elaborated and potential improvements in the design and in the fabrication of these components highlighted. Several improvements over the original grating couplers used in this work could be achieved. The footprint of the grating couplers was reduced by more than 16x using focusing grating coupler designs compared to grating couplers with linear tapers. The ripple of the grating couplers resulting from residual reflection of the rear facet of the grating was reduced by anti-reflection wedges and a partially etched grating coupler design. The coupling angle was increased from 8° to 15° off-vertical angle to further reduce the ripple in the spectral response of the grating couplers. An efficiency larger than -6 dB (25%), a 3dB-bandwidth of 130 nm and a peak-to-peak ripple smaller than 0.05 dB were demonstrated when using an index matching liquid.

9 Conclusion and Outlook

This chapter summarizes the work and highlights the major scientific and technological achievements obtained in context of this thesis. Also, issues observed and limitations of the devices are discussed briefly. An outlook is given how the work on the presented InP microdisks and the used technology should be continued. Finally, this chapter ends with a critical analysis on the perspective of this device class and the photonic integration approach used.

9.1 Summary and conclusion

An introduction to the subject of this thesis was given in Chapter 1. The evolution of telecommunication systems and computing system towards state-of-the-art was described. A discussion was given, why a convergence of the technology used in both application fields is expected and why photonic integration is required. Unsolved challenges in the field of photonic integration were presented and the major contributions of this thesis that address these challenges were highlighted.

Chapter 2 described the photonic integration technology and fabrication methods used in this work. After giving a general introduction to the state-of-the-art optical integration technologies, the silicon photonic base technology used in this work was described. The heterogeneous integration technology used within the thesis was highlighted and the fabrication scheme to achieve electrically contacted InP microdisks was described. Changes in the fabrication process to improve the performance of the microdisks were discussed.

In Chapter 3 the application of the InP microdisks as a laser was explained. First, the device was modelled using a set of rate equations. The equations were solved statically and dynamically. The model was then employed for modelling bi-stability mode switching [53] and wavelength conversion [54]. After presenting static performance figures and the characteristic temperatures of InP microdisk lasers the high-speed properties of the devices were presented. A parameter extraction scheme to accurately extract the parasitics and the intrinsic electrical components for modelling the InP microdisks with a small-signal equivalent circuit was discussed.

The application of InP microdisk lasers as all-optical flip-flops was described in Chapter 4. The model derived in Chapter 3 was implemented

to investigate the switching properties of the counter-propagating modes. A switching time of 60 ps and a switching energy of 1.8 fJ were found experimentally and through simulations. The switching limitations were then further investigated through simulations. It was found that a minimal optical pulse energy of 0.7 fJ is sufficient to reverse the state of operation of a microdisk-flip-flop. By injecting short optical pulses into the flip-flop it was found by simulations that pulse durations of 20 ps are sufficient to revert the lasing direction. The potential application of these flip-flops in all-optical logic systems was discussed. It was found that the devices fulfil some requirements on logic systems, such as fan-out and signal refreshing properties. However, the required cascability could not be confirmed experimentally. Also, the need for an optical isolation scheme is an open issue, which requires further research.

Chapter 5 contains a detailed study on microdisk-based all-optical wavelength converters. The underlying switching mechanism was explained and simulated with the model given in Chapter 3. Static and dynamic characteristics of the conversion process were presented. Wavelength conversion is an important functionality that is interesting for, e.g., contention resolution in optical switching systems. For this and other applications it is required to perform wavelength conversions towards larger and shorter wavelengths in the same device. For the first time, it was shown that a single InP microdisk can be used for wavelength up- and down-conversion [56, 57].

Chapter 6 covered the use of InP microdisks as photodetectors under reverse bias and external illumination. The spectral response of the photocurrent and the corresponding responsivity were reported. Also, the temporal behaviour of this operation mode of the device was studied and operation up to 10 Gb/s was reported [59].

Chapter 7 highlighted the application of InP microdisks as modulators, both under forward and negative bias. The static and dynamic performance of both bias conditions were presented and speed limitations were discussed. Under forward bias, a study on both the inverting and non-inverting operation was carried out. For the first time also negative-biased InP microdisk modulators suitable for high-speed operation up to 10 Gb/s were presented using a small-signal analysis and a large-signal analysis [60, 61].

Chapter 8 discusses several approaches how to improve the performance of the microdisk devices. First, ways to improve the output power of microdisk lasers were described. It was found that by accurately tuning the

coupling between disk and waveguide a significant increase in output power can be expected. Moreover, the positioning of the top contact via opening was found to have a large influence on the quality factor Q of the disk cavity. By implementing a meandering coupling section it was shown that the side-mode suppression ratio can be enhanced. As shown in Chapter 3 the speed of the devices is largely governed by the device parasitics. To increase the speed, it was shown that the pad capacitance could be reduced by increasing the thickness of the cladding. To decrease the series resistance of the bottom contact a process to form a metal alloy may be implemented. Using these fabrication methods it was concluded that by implementing the proposed modifications a significant improvement in device speed can be expected enabling direct modulation at 10 Gb/s and beyond.

To improve the output power of InP microdisk lasers it was found that alignment of the disk with respect to the waveguide defining the coupling critical, but also the alignment and especially size of the top contact, which induces absorption. Therefore a precise control in terms of alignment and feature size control is required.

During the system experiments the laser power emitted by the MDL was coupled off the chip using grating couplers. The coupling losses of the grating couplers used in the experiments were identified to partially limit the measurements of the InP microdisks. Ways to improve the performance of grating couplers were discussed. It was demonstrated that by appropriate design the footprint of the grating couplers can be substantially reduced. Also, the bandwidth was largely enhanced while simultaneously improving coupling efficiency and lowering the Fabry-Perot ripple in the spectrum [62, 156].

9.2 Outlook

Fabrication The main issue identified throughout this work was the manufacturability of electrically contacted InP microdisks. Although an electrical yield in excess of 90% could be achieved, the optical output power was strongly varying over the chip. This means, that the fabrication process presented does not allow to reproducibly produce microdisk devices emitting high output power levels. The origin of varying output powers was found in the alignment accuracy and in the varying polymer bonding layer thickness, that cannot be accurately controlled even when using machine bonding. When moving to molecular bonding using a planarized silicon dioxide layer a better thickness control is expected. Also, silicon dioxide exhibits a three-fold higher thermal conductivity that would effectively help to heat-sink the devices.

To overcome the large alignment inherent to optical contact lithography the use of a stepper or scanner might be a feasible approach. Steppers or scanners allow alignment tolerance that are substantially smaller than the actual critical dimension for the respective technology node they are signed for. E.g. a 90-nm-CMOS stepper is typically capable of performing alignment tolerances better than 20 nm - over an 8 inch wafer. This means that for smaller substrates this alignment tolerance would be even better.

If no stepper or scanner is available also electron beam (e-beam) lithography might be employed. To achieve a good alignment tolerance, however, markers suitable for e-beam recognition are required. The current processing flow only contains silicon and dielectric markers, which have a weak contrast in these tools. This means, that ways to fabricate metallic alignment markers during the fabrication of the silicon photonics layers need to be implemented. Furthermore, these markers would then be buried underneath the dielectric bonding layer and would need to be opened thus requiring an additional mask level for the back-end InP processing.

Speed By analysing the small-signal reflection coefficient S_{11} with a SSEC it could be shown that the performance of InP microdisk modulators is largely covered by the internal parasitics of the device. Small improvements in the operation speed can be achieved through reducing the pad capacitance, e.g., by applying a thicker silicon dioxide cladding. It was also shown that by reducing the diameter of the devices, which governs the capacitance of the active region, the device speed can also be increased.

Moreover, it was found that the resistance of the active III-V epitaxial layer stack has the largest influence on the device speed. Substantial speed improvements are expected by a reduction of this electric component, which may be achieved by improving the doping profile of the tunnel junction or by increasing the conductivity of the barriers through the introduction of a slight background-doping for instance. When implementing the proposed changes a significant speed improvement of InP microdisk lasers is expected suggesting that direct modulation in excess of 10 Gb/s is within reach.

Output power The output power of the lasers investigated in this thesis was too low to enable an on-chip optical link with a sole InP microdisk detector without integrating a TIA. Simulations presented in chapter 3 have shown that the output power of InP microdisks emitted into the waveguide may be as large as 100 μW (-10 dBm). Such power levels are required to enable optical transceiver chips with a meaningful link budget. A power level of about -18 dBm is required at 10 Gb/s at the receiver to detect the signal without errors, leaving about 8 dB link budget, which can then be split between propagation loss, insertion loss of modulators, and coupling losses. This, in combination with a co-integrated TIA would enable on-chip optical links. This in turn means, that if the above-mentioned improvements in the fabrication process can be implemented, InP microdisk lasers have the potential to serve as laser sources for optical transceivers at data rates of 10 Gb/s.

MDL-based optical links It was shown that the InP microdisks can be used as lasers, modulators and detectors. The expected optical output power in the waveguide of about -10 dBm in combination with a photo diode responsivity of 5 A/W make this approach very interesting for short-reach optical communication. Fig. 9.1 shows a schematic of a potential implementation of a transceiver chip using the approach, in which a sole microdisk would either be operated as a laser or as a photodiode; depending on the bias. If the desired data rate is in excess of 10 Gb/s, which is faster than the direct modulation capabilities of the investigated InP-based MDLs, then one device may be operated as a laser under continuous-bias and another device located on the same silicon waveguide may be operated on the same wavelength as a negatively-biased electro-optical modulator as discussed in chapter 7 [157].

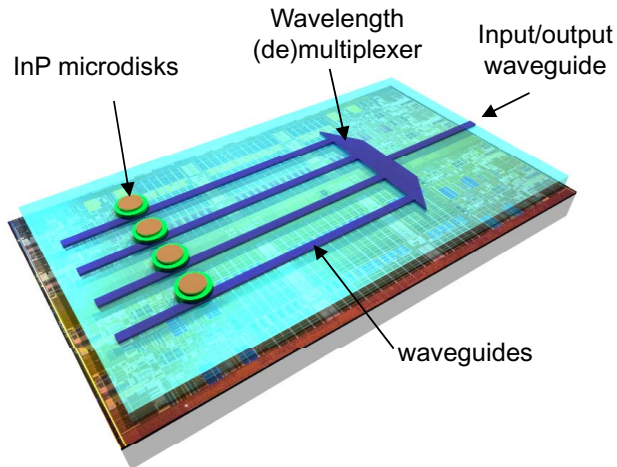


Figure 9.1: Schematic view of a potential implementation of an InP microdisk-based optical transceiver chip.

Towards half-duplex optical links In this work, the concept of using a single device for signal generation and for signal detection under negative bias was demonstrated experimentally with individual components at 10 Gb/s. The presented concept alleviates the need for complicated fabrication methods, such as, e.g., quantum well intermixing [72] by tuning the coupling between a weakly absorbing resonant device and a waveguide. This approach opens a new route towards optical links using multi-purpose devices for signal generation and detection [157].

References

- [1] F.B. Morse. Improvement in the mode of communicating information by signals by the application of electro-magnetism, US Patent No. 1647. 1840.
- [2] Cisco. White Paper: Data Center Services Systems. http://www.cisco.com/en/US/prod/collateral/routers/ps5763/DC_Services_System_WP.pdf, accessed 11 November 2012.
- [3] Mellanox Press Release. Mellanox FDR infiniband selected to deliver petascale performance for europe's fastest supercomputer. http://www.mellanox.com/content/pages.php?pg=press_release_item&rec.id=580, accessed 01 October 2012.
- [4] F.E. Doany, C.W. Baks, D.M. Kutcha, P. Pepeljugowski, L. Schares, R. Budd, F. Libsch, R. Dangel, F. Horst, B.J. Offrein, and J.A. Kash. 160 Gb/s Bidirectional Polymer-Waveguide Board-Level Optical Interconnects Using CMOS-Based Transceivers. *IEEE Transactions on Advances Packaging*, 32(2):345–359, 2009.
- [5] C.L. Schow, F.E. Doany, A.V. Rylyakov, B.G. Lee, C.V. Jahnes, Y.H. Kwark, C.W. Baks, D.M. Kutcha, and J.A. Kash. A 24-Channel, 300 Gb/s, 8.2 pJ/bit, Full-Duplex Fiber-Coupled Optical Transceiver Module Based on a Single "Holey" CMOS IC. *IEEE Journal of Lightwave Technology*, 29(4):542–553, 2011.
- [6] J.T. Rahn, S. Kumar, M. Mitchell, R. Malendevich, H. Sun, K.-T. Wu, P. Mertz, K. Croussore, H. Wang, M. Kato, V. Lal, P. Evans, D. Lambert, H.-S. Tsai, P. Samra, B. Taylor, A. Nilsson, S. Grubb, R. Nagarajan, F. Kish, and D. Welch. 250Gb/s Real-time PIC-based Super-Channel Transmission over a Gridless 6000km Terrestrial Link. *Optical Fiber Communication Conference (OFC 2012), Los Angeles, California*, Post Deadline Paper PDP5D, 2012.
- [7] Y. Vlasov. Silicon Integrated Nanophotonics: Road from Scientific Explorations to Practical Applications. *Conference on Lasers and Electro-Optics (CLEO 2012), San Jose, California*, Plenary Talk: Science and Innovations, 2012.

-
- [8] H. Park, A.W. Fang, S. Kodama, and J.E. Bowers. Hybrid Silicon Evanescent Laser Fabricated With a Silicon Waveguide and III-V Offset Quantum Wells. *Optics Express*, 13(23):9460–9464, 2005.
- [9] J. Van Campenhout, P. Rojo-Romeo, P. Regreny, C. Seassal, D. Van Thourhout, S. Verstuyft, L. Di Cioccio, J.-M. Fedeli, C. Lagahe, and R. Baets. Electrically pumped InP-based microdisk lasers integrated with a nanophotonic silicon-on-insulator waveguide circuit. *Optics Express*, 15(11):6744–6749, 2007.
- [10] J. Piprek. *Optoelectronic Devices: Advanced Simulation and Analysis*. Springer, 2004.
- [11] K.L. Lear, V.M. Hietala, H.Q. Hou, M. Ochiai, J.J. Banas, B.E. Hammons, J.C. Zolper, and S.P. Kilcoyne. Small and large signal modulation of 850 nm oxide-confined vertical-cavity surface-emitting lasers. *Advances in Vertical Cavity Surface Emitting Lasers in Trends in Optics and Photonics Series*, 15:69–74, 1997.
- [12] J. Boucart, C. Starck, F. Gaborit, A. Plais, N. Bouche, E. Derouin, J.C. Remy, J. Bonnet-Gamard, L. Goldstein, C. Fortin, D. Carpentier, P. Salet, F. Brillouet, and J. Jacquet. Metamorphic DBR and Tunnel-Junction Injection: A CW RT Monolithic Long-Wavelength VCSEL. *IEEE Journal of Selected Topics in Quantum Electronics*, 5(3):520–529, 1999.
- [13] P. Rojo Romeo, J. Van Campenhout, P. Regreny, A. Kazmierczak, C. Seassal, X. Letartre, G. Hollinger, D. Van Thourhout, R. Baets, J.-M. Fedeli, and L. Di Cioccio. Heterogeneous integration of electrically driven microdisk based laser sources for optical interconnects and photonic ICs. *Optics Express*, 14(9):3864–3871, 2006.
- [14] A.F.J. Levi. *Applied Quantum Mechanics*. Cambridge University Press, San Francisco, CA, 2003. revised printing.
- [15] R. Kumar, L. Liu, G. Roelkens, G. Morthier, and R. Baets. Simple and accurate measurements to characterize microdisk lasers for all-optical flip-flop operation. *Proc. Ann. Symp. IEEE Photonics Benelux Chapter Belgium*, 2009.

- [16] M.R. Watts, W.A. Zortman, D.C. Trotter, R.W. Young, and A.L. Lentine. Vertical junction silicon microdisk modulators and switches. *Optics Express*, 19(22):21989–22003, 2011.
- [17] C.J. Koester and E. Snitzer. Amplification in a Fiber Laser. *Applied Optics*, 3(10):1182–1186, 1964.
- [18] C.K. Kao and G.A. Hockham. Dielectric-fibre surface waveguides for optical frequencies. *Proceedings of the IEE*, 113:1151–1158, 1966.
- [19] R.-J. Essiambre, G. Kramer, P.J. Winzer, G.J. Foschini, and B. Goebel. Capacity Limit of Optical Fiber Networks. *IEEE Journal of Lightwave Technology*, 28(4):662–701, 2010.
- [20] K. Zuse. Inception of a universal theory of computation with special consideration of the propositional calculus and its application to relay circuits - Ansätze einer Theorie des allgemeinen Rechnens unter besonderer Berücksichtigung des Aussagenkalküls und dessen Anwendung auf Relaisschaltungen. *Unpublished manuscript*, 1943.
- [21] J. Bardeen, W. Brattain, and W. Shockley. The transistor, a semiconductor triode. *Physical Review*, 74:230–231, 1948.
- [22] J. Kilby. Miniaturized electronic circuits, US Patent No. 3138743, 1964.
- [23] R. Noyce. Semiconductor device-and-lead structure, US Patent No. 2981877, 1961.
- [24] G. Moore. Cramming more components onto integrated circuits. *Electronics*, 38(8):114–117, 1965.
- [25] TOP500.ORG. Top500 list - june 2012 (1-100). <http://www.top500.org/list/2012/06/100>, accessed 10 October 2012.
- [26] J. Broughton. Hybrid and Manycore Architectures. [http://www.openfabrics.org/archives/spring2010sonoma/Tuesday/8.30/Jeff Broughton HybridMulticore/OFA-2010-Broughton.ppt](http://www.openfabrics.org/archives/spring2010sonoma/Tuesday/8.30/Jeff%20Broughton%20HybridMulticore/OFA-2010-Broughton.ppt), accessed 01 October 2012.

- [27] J. Kash, F. Doany, D. Kutcha, L. Schares, C. Schow, M. Taubenblatt, B.J. Offrein, and A. Benner. Towards exaflop servers and supercomputers: The roadmap for lower power and higher density optical interconnects. *Proceedings of the 36th European Conference and Exhibition on Optical Communication, ECOC 2010, Torino, Italy*, 1-14, 2010.
- [28] R.C.A Pitwon, K. Hopkins, K. Wang, D.R. Selviah, H. Baghsiahi, B.J. Offrein, R.Dangel, F. Horst, M. Halter, and M Gmuer. Design and implementation of an electro-optical backplane with pluggable in-plane connectors. *SPIE Photonics West: Optoelectronic Interconnects and Component Integration IX, 23 - 28 January 2010, San Francisco, California, US*, 2010.
- [29] E. Anzures, R. Dangel, R. Beyeler, A. Cannon, F. Horst, C. Kiarie, P. Knudsen, N. Meier, M. Moynihan, and B.J.Offrein. Flexible optical interconnects based on silicon-containing polymers. *Proceedings of SPIE: Photonics Packaging, Integration, and Interconnects, 2009, USA*, 2009.
- [30] F.E. Doany, C.L. Schow, B.G. Lee, R.A. Budd, C.W. Baks, C.K. Tsang, J.U. Knickerbocker, R. Dangel, B. Chan, H. Lin, C. Carver, J. Huang, J. Berry, D. Bajkowski, F. Libsch, and J.A. Kash. Terabit/s-Class Optical PCB Links Incorporating 360-Gb/s Bidirectional 850 nm Parallel Optical Transceivers . *IEEE Journal of Light-wave Technology*, 30(4):560–571, 2012.
- [31] P. Dumon, W. Bogaerts, V. Wiaux, J. Wouters, S. Beckx, J. Van Campenhout, D. Taillaert, B. Luyssaert, P. Bienstman, D. Van Thourhout, and R. Baets. Low-loss SOI Photonic Wires and Ring Resonators Fabricated with Deep UV Lithography. *IEEE Photonics Technology Letters*, 16(5):1328–1330, 2004.
- [32] S. McNab, N. Moll, and Y. Vlasov. Ultra-low loss photonic integrated circuit with membrane-type photonic crystal waveguides. *Optics Express*, 11(22):2927–2939, 2003.
- [33] D. Taillaert, W. Bogaerts, P. Bienstman, T.F. Krauss, P. Van Daele, I. Moerman, S. Verstuyft, K. De Mesel, and R. Baets. An Out-of-Plane Grating Coupler for Efficient Butt-Coupling Between Compact

- Planar Waveguides and Single-Mode Fibers. *IEEE Journal of Quantum Electronics*, 38(7):949–955, 2002.
- [34] N. Lindenmann, G. Balthasar, D. Hillerkuss, R. Schmogrow, M. Jordan, J. Leuthold, W. Freude, and C. Koos. Photonic wire bonding: a novel concept for chip-scale interconnects. *Optics Express*, 20(16):17667–17677, 2012.
- [35] D. Huber, R. Bauknecht, C. Bergamaschi, M. Bitter, A. Huber, T. Morf, A. Neiger, M. Rohner, I. Schnyder, V. Schwarz, and H. Jaeckel. InP-InGaAs single HBT technology for photoreceiver OE-ICs at 40 Gb/s and beyond. *IEEE Journal of Lightwave Technology*, 18(7):992–1000, 2000.
- [36] C. Gunn. CMOS Photonics for High-Speed Interconnects. *IEEE Micro*, 26(2):58–66, 2006.
- [37] S. Selvaraja, P. Jaenen, W. Bogaerts, P. Dumon, D. Van Thourhout, and R. Baets. Fabrication of Photonic Wire and Crystal Circuits in Silicon-On-Insulator Using 193nm Optical Lithography. *IEEE Journal of Lightwave Technology*, 27(18):4076–4083, 2009.
- [38] W.M. Green, S. Assefa, A. Rylyakov, C. Schow, F. Horst, and Y. A. Vlasov. CMOS integrated silicon nanophotonics: enabling technology for exascale computational systems. *SEMICON 2010, Chiba, Japan*, 2010.
- [39] J.S. Orcutt, B. Moss, C. Sun, J. Leu, M. Georgas, J. Shainline, E. Zraggen, H. Li, J. Sun, M. Weaver, S. Urosevic, M. Popovic, R.J. Ram, and V. Stojanovic. Open foundry platform for high-performance electronic-photonic integration. *Optics Express*, 20(11):12222–12232, 2012.
- [40] H. Pan, S. Assefa, W.M. Green, D.M. Kutcha, C.L. Schow, A.V. Rylyakov, B.G. Lee, C.W. Baks, S.M. Shank, and Y.A. Vlasov. 40Gbps Optical Receiver Based on Germanium Waveguide Photodetector Hybrid-Integrated with 90nm CMOS Amplifier. *Conference on Lasers and Electro-Optics (CLEO 2012), San Jose, California*, Post Deadline Paper CTh5D, 2012.

-
- [41] S.J.B. Yoo. Wavelength conversion technologies for WDM network applications. *IEEE Journal of Lightwave Technology*, 14(6):995–966, 1996.
- [42] S. Rangarajan, Z. Hu, L. Rau, and D.J. Blumenthal. All-optical contention resolution with wavelength conversion for asynchronous variable-length 40 Gb/s optical packets . *IEEE Photonics Technology Letters*, 16(2):689–691, 2004.
- [43] Q. Xu, V.R. Almeida, and M. Lipson. Micrometer-scale all-optical wavelength converter on silicon. *Optics Letters*, 30:2733–2735, 2005.
- [44] A. C. Turner, M. A. Foster, A. L. Gaeta, and M. Lipson. Ultralow power parametric frequency conversion in a silicon microring resonator. *Optics Express*, 16(7):4881–4887, 2008.
- [45] Y. Liu, E. Tangdionga, Z. Li, H. de Waardt, A. M. J. Koonen, G. D. Khoe, X. Shu, I. Bennion, and H.J.S. Dorren. Error-Free 320-Gb/s All-Optical Wavelength Conversion Using a Single Semiconductor Optical Amplifier. *IEEE Journal of Lightwave Technology*, 25(1):103–108, 2007.
- [46] O. Raz, J. Herrera, N. Calabretta, E. Tangdionga, S. Ananthanasarn, R. Notzel, and H.J.S. Dorren. Non-inverted multiple wavelength converter at 40 Gb/s using 1550 nm quantum dot SOA. *Electronics Letters*, 44(16):988–989, 2008.
- [47] R. Soref and J.P. Lorenzo. All-silicon active and passive guided-wave components for $\lambda = 1.3$ and 1.6 μm . *IEEE Journal of Quantum Electronics*, 22:873–879, 1986.
- [48] Q. Xu, B. Schmidt, S. Pradhan, and M. Lipson. Micrometre-scale silicon electro-optic modulator. *Nature*, 435(7040):325–327, 2005.
- [49] D. Marris-Morrini, X. Le Roux, L. Vivien, E. Cassan, D. Pascal, M. Halbwax, S. Maine, S. Laval, J.-M. Fedeli, and J.F. Damlencourt. Optical modulation by carrier depletion in a silicon PIN diode. *Optics Express*, 14:10838–10843, 2006.
- [50] L. Liu, J. Van Campenhout, G. Roelkens, R.A. Soref, D. Van Thourhout, P. Rojo-Romeo, P. Regreny, C. Seassal, J.-M. Fedeli, and

- R. Baets. Carrier-injection-based electro-optic modulator on silicon-on-insulator with a heterogeneously integrated III-V microdisk cavity. *Optics Letters*, 33(21):2518–2520, 2008.
- [51] L. Liu, R. Kumar, K. Huybrechts, T. Spuesens, G. Roelkens, E.-J. Geluk, T. De Vries, P. Regreny, D. Van Thourhout, R. Baets, and G. Morthier. An ultra-small, low-power, all-optical flip-flop memory on a silicon chip. *Nature Photonics*, 4:182–187, 2010.
- [52] F. Horst. Silicon Integrated Waveguide Devices for Filtering and Wavelength Demultiplexing. *Optical Fiber Communication Conference (OFC 2010), San Diego, USA*, Talk OWJ3, 2010.
- [53] J. Hofrichter, O. Raz, F. Horst, N. Chrysos, C. Minkenber, T. de Vries, H.J.S. Dorren, R. Kumar, L. Liu, and B.J. Offrein. A fast and comprehensive microdisc laser model applied to all-optical wavelength conversion. *Integrated Photonics Research, Silicon and Nano Photonics (IPR), Photonics in Switching (PS), Monterey, USA*, Talk PTuA2, 2010.
- [54] J. Hofrichter, F. Horst, N. Chrysos, C. Minkenber, R. Kumar, L. Liu, G. Morthier, T. de Vries, and B.J. Offrein. Digital all-optical signal processing using microdisc lasers. *Integrated Photonics Research, Silicon and Nano Photonics (IPR), Photonics in Switching (PS), Monterey, USA*, Talk PTuA3, 2010.
- [55] L. Liu, J. Van Campenhout, G. Roelkens, D. Van Thourhout, P. Rojo-Romeo, P. Regreny, C. Seassal, J.-M. Fedeli, and R. Baets. Ultralow-power all-optical wavelength conversion in a silicon-on-insulator waveguide based on a heterogeneously integrated III-V microdisk laser. *Applied Physics Letters*, 93(6):061107, 2008.
- [56] J. Hofrichter, O. Raz, L. Liu, G. Morthier, F. Horst, P. Regreny, T. De Vries, H.J.S. Dorren, and B.J. Offrein. All-optical wavelength conversion using mode switching in an InP microdisc laser. *Electronics Letters*, 47(16):927–929, 2011.
- [57] J. Hofrichter, O. Raz, L. Liu, G. Morthier, F. Horst, P. Regreny, T. De Vries, H.J.S. Dorren, and B.J. Offrein. Dual Wavelength Conversion Using Electrically Pumped Microdisc Lasers. *IEEE Group IV Photonics Conference, London, United Kingdom*, Talk ThB3, 2011.

- [58] O. Raz, L. Liu, R. Kumar, G. Morthier, P. Regreny, and H.J.S. Dorren. A single InP membrane disc cavity for both transmission and detection of 10Gb/s signals in on chip interconnects. *Proceedings of the 36th European Conference and Exhibition on Optical Communication, ECOC 2010, Torino, Italy*, Paper 2.12, 2010.
- [59] J. Hofrichter, T. Morf, A. La Porta, O. Raz, H. Dorren, and B. Offrein. Compact InP-on-SOI Microdisks Used as High-Speed Modulators and Photo Detectors. *Proceedings of the 38th European Conference and Exhibition on Optical Communication, ECOC 2012, Amsterdam, The Netherlands*, P. 2.03, 2012.
- [60] J. Hofrichter, O. Raz, A. La Porta, T. Morf, P. Mechet, G. Morthier, T. De Vries, H.J.S. Dorren, and B.J. Offrein. A low-power high-speed InP microdisk modulator heterogeneously integrated on a SOI waveguide. *Optics Express*, 20(9):9363–9370, 2012.
- [61] J. Hofrichter, A. La Porta, T. Morf, B.J. Offrein, P. Mechet, G. Morthier, T. De Vries, H.J.S. Dorren, and O. Raz. Compact high-speed InP microdisk modulators heterogeneously integrated on a SOI waveguide. *Proceedings of the IEEE Optical Interconnects Conference, 20-23 May 2012, Santa Fe, New Mexico*, Paper MB6, 2012.
- [62] J. Hofrichter, W.M. Green, F. Horst, S. Assefa, M. Yang, B.J. Offrein, and Y. A. Vlasov. Gating Couplers as Optical Probe Pads in a Standard CMOS Process. *IEEE Group IV Photonics Conference (GFP), London, United Kingdom*, Poster P1.24, 2011.
- [63] M. Schroter, G. Wedel, B. Heinemann, C. Jungemann, J. Krause, P. Chevalier, and A. Chantre. Physical and Electrical Performance Limits of High-Speed SiGeC HBTs—Part I: Vertical Scaling. *IEEE Transactions on Electron Devices*, 58(11):3687–3696, 2011.
- [64] M. Schroter, J. Krause, N. Rinaldi, G. Wedel, B. Heinemann, P. Chevalier, and A. Chantre. Physical and Electrical Performance Limits of High-Speed Si GeC HBTs—Part II: Lateral Scaling. *IEEE Transactions on Electron Devices*, 58(11):3697–3706, 2011.
- [65] C.R. Doerr and K. Okamoto. Advances in Silica Planar Lightwave Circuits. *IEEE Journal of Lightwave Technology*, 24(12):4763–4789, 2006.

- [66] E.F. Burmeister, J.P. Mack, H.N. Poulsen, M.L. Masanovic, B. Stamenic, D.J. Blumenthal, and J.E. Bowers. Photonic integrated circuit optical buffer for packet-switched networks. *Optics Express*, 17(8):6629–6635, 2009.
- [67] Infinera White Paper: The Dawn of the Terabit Age. http://www.infinera.com/technology/files/infinera-Dawn_Terabit_Age.pdf, accessed 26 September 2012.
- [68] W.M. Green, M.J. Rooks, L. Sekaric, and Y.A. Vlasov. Ultra-compact, low RF power, 10 Gb/s silicon Mach-Zehnder modulator. *Optics Express*, 15(25):17106–17113, 2007.
- [69] S. Assefa, F. Xia, and Y.A. Vlasov. Reinventing germanium avalanche photodetector for nanophotonic on-chip optical interconnects. *Nature*, 464:80–84, 2010.
- [70] R.E. Camacho-Aguilera, Y. Cai, N. Patel, T. Bessette, M. Romagnoli, L.C. Kimerling, and J. Michel. An electrically pumped germanium laser. *Optics Express*, 20(10):11316–11320, 2012.
- [71] Y.-H. Kuo, H.-W. Chen, and J. E. Bowers. High speed hybrid silicon evanescent electroabsorption modulator. *Optics Express*, 16(13):9936–9941, 2008.
- [72] H. Park, Y.-H. Kuo, A.W. Fang, R. Jones, O. Cohen, M. Paniccia, and J.E. Bowers. A hybrid AlGaInAs-silicon evanescent preamplifier and photodetector. *Optics Express*, 15(21):13539–13546, 2007.
- [73] I. Christiaens, G. Roelkens, K. De Mesel, D. Van Thourhout, and R. Baets. Adhesive wafer bonding with Benzocyclobutene. *IEEE Journal of Lightwave Technology*, 1(11):1–7, 2004.
- [74] G. Roelkens, J. Brouckaert, D. Taillart, P. Dumon, W. Bogaerts, D. Van Thourhout, and R. Baets. Integration of InP/InGaAsP photodetectors on Silicon-on-Insulator waveguide circuits. *Optics Express*, 13(25):10102–10108, 2005.
- [75] IPKISS. <http://www.ipkiss.org>, accessed 21 September 2012.
- [76] S.M. Sze. *Physics of Semiconductor Devices, 2nd Edition*. John Wiley & Sons, New York, 1981.

-
- [77] S. Schmitt-Rink, D.S. Chemla, and D.A.B. Miller. Linear and non-linear optical properties of semiconductor quantum wells. *Advances in Physics*, 38(2):89–188, 1989.
- [78] J. Leuthold, M. Mayer, J. Eckner, G. Guekos, H. Melchior, and C. Zellweger. Material gain of bulk 1.55 μm InGaAsP/InP semiconductor optical amplifiers approximated by a polynomial model. *Journal of Applied Physics*, 87:618–620, 2000.
- [79] S. Keyvaninia, M. Muneeb, S. Stankovic, G. Roelkens, D. Van Thourhout, and J.M. Fedeli. Multiple die-to-wafer adhesive bonding for heterogeneous integration. *Proceedings of the 6th European Conference on Integrated Optics, (ECIO 2012), Barcelona, Spain*, Paper 186, 2012.
- [80] J.H. Den Besten, M.P. Dessens, C.G.P. Herben, X.J.M. Leijtens, F.H. Groen, and M.K. Smit. Low-loss, compact, polarization independent PHASAR demultiplexer fabricated by using a double-etch process. *IEEE Photonics Technology Letters*, 14(1):62–64, 2002.
- [81] J.F. Shackelford and W. Alexander. *CRC Materials Science and Engineering Handbook, Third Edition*. CRC Press, Boca Raton, Florida, 2000.
- [82] P. Garrou, R. Heistand, M. Dibbs, T. Mainal, C. Mohler, T. Stokich, P. Townsend, G. Adema, M. Berry, and I. Turlik. Rapid Thermal Curing of BCB Dielectric. *IEEE Transactions on Components, Hybrids, and Manufacturing Technology*, 16:46–52, 1993.
- [83] A.N. AL-Omari and K.L. Lear. *High-Speed Vertical-Cavity Surface-Emitting Lasers*. VDM Verlag Dr. Mueller, Saarbruecken, Germany, 2009.
- [84] L. Pavesi, L. Dal Negro, C. Mazzoleni, G. Franzo, and F. Priolo. Optical gain in silicon nanocrystals. *Nature*, 408:440–444, 2000.
- [85] A.G. Nassiopoulou, S. Grigoropoulos, and D. Papadimitriou. Electroluminescent devices based on silicon nanopillars. *Applied Physics Letters*, 69:2267–2269, 1996.

- [86] H. Rong, R. Jones, A. Liu, O. Cohen, D. Hak, A. Fang, and M. Paniccia. A continuous-wave Raman silicon laser. *Nature*, 433:725–728, 2005.
- [87] H. Rong, S. Xu, Y.-H. Kuo, V. Sih, O. Cohen, O. Radaay, and M. Paniccia. Low-threshold continuous-wave Raman silicon laser. *Nature Photonics*, 1:232–237, 2007.
- [88] B. Kunert, S. Zinnkann, K. Volz, and W. Stolz. Monolithic integration of Ga(NAsP)/(BGa)P multi-quantum well structures on (001) silicon substrate by MOVPE. *Journal of Crystal Growth*, 310:4776–4779, 2008.
- [89] N. Koukourakis, C. Bueckers, D.A. Funke, N.C. Gerhardt, S. Liebich, S. Chatterjee, C. Lange, M. Zimprich, K. Volz, W. Stolz, B. Kunert, S. W. Koch, and M. R. Hofmann. High room-temperature optical gain in Ga(NAsP)/Si heterostructures. *Applied Physics Letters*, 100:092107, 2012.
- [90] J. Liu, X. Sun, R. Camacho-Aguilera, L.C. Kimerling, and J. Michel. Ge-on-Si laser operating at room temperature. *Optics Letters*, 35.
- [91] A.W. Fang, H. Park, O. Cohen, R. Jones, M.J. Paniccia, and J.E Bowers. Electrically pumped hybrid AlGaInAs evanescent laser. *Optics Express*, 14(20):9203–9210, 2006.
- [92] A.W. Fang, E. Lively, Y.-H. Kuo, D. Liang, and J.E Bowers. A distributed feedback silicon evanescent laser. *Optics Express*, 16(7):4413–4419, 2008.
- [93] A.W. Fang, M.N. Sysak, B.R. Koch, R. Jones, E. Lively, Y.-H. Kuo, D. Liang, O. Radaay, and J.E Bowers. Single-Wavelength Silicon Evanescent Lasers. *IEEE Journal of Selected Topics in Quantum Electronics*, 15(3):535–544, 2009.
- [94] D. Liang and J. Bowers. Electrically-pumped compact hybrid silicon microring lasers for optical interconnects. *Optics Express*, 17(22):20355–20364, 2009.

- [95] G. Roelkens, D. Van Thourhout, R. Baets, R. Notzel, and M.K. Smit. Laser emission and photodetection in an InP/InGaAsP layer integrated on and coupled to a silicon-on-insulator waveguide circuit. *Optics Express*, 14(18):8154–8159, 2006.
- [96] J. Van Campenhout, P. Rojo-Romeo, D. Van Thourhout, C. Seassal, P. Regreny, L. Di Cioccio, J.-M. Fedeli, and R. Baets. Design and Optimization of Electrically Injected InP-Based Microdisk Lasers Integrated on and Coupled to a SOI Waveguide Circuit . *IEEE Journal of Lightwave Technology*, 26(1):52–63, 2008.
- [97] L. Liu, J. Van Campenhout, P. Rojo-Romeo, P. Regreny, C. Seassal, D. Van Thourhout, S. Verstyuyft, L. Di Cioccio, J.-M. Fedeli, C. Lagae, and R. Baets. Compact multiwavelength laser source based on cascaded InP-microdisks coupled to one SOI waveguide. *Optical Fiber Communication Conference (OFC 2008), San Diego, USA*, Talk OWQ3, 2008.
- [98] O. Raz, L. Liu, D. Van Thourhout, P. Rojo-Romeo, J.-M. Fedeli, and H.J.S. Dorren. High speed wavelength conversion in a heterogeneously integrated disk laser over silicon on insulator for network on a chip applications. *Proceedings of the 35th European Conference and Exhibition on Optical Communication, ECOC 2009, Vienna, Austria*, Paper 4.2.3, 2009.
- [99] M.T. Hill, H.J.S. Dorren, T. de Vries, X. Leijtens, J.H. den Besten, B. Smalbrugge, Y.-S. Oei, H. Binsma, G.D. Khoe, and M.K. Smit. Terabit/s-Class Optical PCB Links Incorporating 360-Gb/s Bidirectional 850 nm Parallel Optical Transceivers . *A fast low-power optical memory based on coupled micro-ring lasers*, 432:206–209, 2004.
- [100] J. Van Campenhout. Thin-Film Microlasers for the Integration of Electronic and Photonic Integrated Circuits. *PhD Thesis, Gent University, Belgium, ISBN 978-90-8578-180-6*, 2007.
- [101] L. Djaloshinski and M. Orenstein. Disk and Ring Microcavity Resonators and Their Concentric Coupling. *IEEE Journal of Quantum Electronics*, 35(5):737–744, 1999.

-
- [102] C.L. Tang, A. Schremer, and T. Fujita. Bistability in two-mode semiconductor lasers via gain saturation. *Applied Physics Letters*, 51(18):1392–1394, 1987.
- [103] G. Yuan and S. Yu. Bistability and switching properties of semiconductor ring lasers with external optical injection. *IEEE Journal of Quantum Electronics*, 44(1):41–48, 2008.
- [104] L.F. Shampine, J. Kierzenka, and M.W. Reichelt. Solving Boundary Value Problems for Ordinary Differential Equations in MATLAB with bvp4c. http://www.tem.uoc.gr/~marina/BVP_tutorial.pdf, accessed 03 September 2011.
- [105] W.E. Lamb, Jr. Theory of an optical maser. *Physical Review A*, 134:1429–1450, 1964.
- [106] M.J. Adams and M. Osihski. Longitudinal mode competition in semiconductor lasers: Rate equations revisited. *IEE Proc. Part I: Solid State Electron Devices*, 129(6):271–274, 1982.
- [107] E.J.D. D’Angelo, E. Izaguirre, G.B. Mindlin, G. Huyet, and J.R. Tredicce. Spatiotemporal Dynamics of Lasers in the Presence of an Imperfect O(2) Symmetry. *Physical Review Letters*, 68(25):3702–3705, 1992.
- [108] M. Sargent III. Theory of a multimode quasi-equilibrium semiconductor laser. *Physical Review A*, 48(1):717–726, 1993.
- [109] F. J. Duarte. *Tunable Laser Optics*. Elsevier Academic, New York, 2003.
- [110] M. Bagheri, M.H. Shih, W.K. Marshall, S.J. Choi, J.D. O’Brien, and P.D. Dapkus. High small-signal modulation bandwidth and narrow linewidth microdisk lasers. *Conference on Lasers and Electro-Optics (CLEO 2008)*, San Jose, USA, 1-2, 2008.
- [111] C.H. Henry. Theory of the linewidth of semiconductor lasers. *IEEE Journal of Quantum Electronics*, 18(2):259–264, 1982.

-
- [112] G. Giuliani, A. Scire, M. Sorel, and S. Donati. Linewidth of monolithic semiconductor ring lasers. *Proceedings of Conference on Semiconductor Lasers and Laser Dynamics II, Strasbourg, France*, SPIE Volume 6184, Paper 618429, 2006.
- [113] G. Sialm. *VCSEL Modeling and CMOS Transmitters up to 40 Gb/s for High-Density Optical Links*. Dissertation, No. 17082, Swiss Federal Institute of Technology, Zurich, Switzerland, 2007.
- [114] D.A.B. Miller. Are optical transistors the logical next step? *Nature Photonics*, 4:3–5, 2010.
- [115] Y. Leblebici. Leakage current reduction using subthreshold source-coupled logic. *IEEE Transactions on Circuits and Systems*, 56(5):347–351, 2009.
- [116] Z. Yu and S. Fan. Complete optical isolation created by indirect interband photonic transitions. *Nature Photonics*, 3:91–94, 2009.
- [117] H.L. Lira, Z. Yu, M. Lipson, and S. Fan. Electro-optical silicon isolator. *Conference on Lasers and Electro-Optics (CLEO 2012), San Jose, California, CW1K*, 2012.
- [118] L. Feng, M. Ayache, J. Huang, Y.-L. Xu, M.-H. Lu, Y.-F. Chen, Y. Fainman, and A. Scherer. Nonreciprocal Light Propagation in a Silicon Photonic Circuit. *Science*, 333:729–733, 2011.
- [119] S. Fan, R. Baets, A. Petrov, Z. Yu, J.D. Joannopoulos, W. Freude, A. Melloni, Milos Popovic, M. Vanwolleghem, D. Jalas, M. Eich, M. Krause, H. Renner, E. Brinkmeyer, and C.R. Doerr. Comment on: Nonreciprocal Light Propagation in a Silicon Photonic Circuit. *Science*, 335:38–, 2012.
- [120] J.Y. Lee, X. Luo, and A.W. Poon. Reciprocal transmission and asymmetric modal distribution in waveguide-coupled spiral-shaped microdisk resonators. *Optics Express*, 15(22):14650–14666, 2007.
- [121] T.R. Zaman, X. Guo, and R.J. Ram. Faraday rotation in an InP waveguide. *Applied Physics Letters*, 90:023514, 2007.

-
- [122] K. Kondo, M. Kuno, S. Yamakoshi, and K. Wakao. A tunable wavelength-conversion laser. *IEEE Journal of Quantum Electronics*, 28(5):1343–1347, 1992.
- [123] T. Durhuus, R.J.S. Pedersen, B. Mikkelsen, K. E. Stubkjaer, M. Oberg, and S. Nilsson. Optical wavelength conversion over 18 nm at 2.5 Gb/s by DBR-Laser. *IEEE Photonics Technology Letters*, 5(1):86–88, 1993.
- [124] C.W. Chow, C.S. Wong, and H.K. Tsang. All-optical NRZ to RZ format and wavelength converter by dual wavelength injection locking. *Optics Communications*, 209:329–334, 2002.
- [125] Y. Onishi, N. Nishiyama, C. Caneau, F. Koyama, and C. Zah. All-optical inverter based on long-wavelength vertical cavity surface emitting laser. *IEEE Journal of Selected Topics in Quantum Electronics*, 11:999–1005, 2005.
- [126] C.J. Buczek, R.J. Freiberg, and M.L. Skolnick. Laser injection locking . *Proceedings of the IEEE*, 61(10):1411–1431, 1973.
- [127] O. Raz, L. Liu, R. Kumar, G. Morthier, D. Van Thourhout, P. Regreny, P. Rojo-Romeo, and H.J.S. Dorren. Compact, Low power and low threshold electrically pumped micro disk lasers for 20 Gb/s non return to zero all-optical wavelength conversion. *Optical Fiber Communication Conference (OFC 2010), San Diego, USA*, Paper OMQ5, 2010.
- [128] P.R.A. Binetti, X.J.M. Leijtens, T. de Vries, Y.S. Oei, L. Di Cioccio, J.-M. Fedeli, C. Lagahe, J. Van Campenhout, D. Van Thourhout, P.J. van Veldhoven, R. Notzel, and M.K. Smit. InP/InGaAs photodetector on SOI circuitry. *Proceedings of the IEEE Group IV Photonics Conference, San Francisco, USA, Talk FA7*, pages 214–216, 2009.
- [129] B. Aslan, H.C. Liu, A. Bezinger, P.J. Poole, M. Buchanan, R. Rehm, and H. Schneider. High responsivity, dual-band response and intra-band avalanche multiplication in InGaAs/InP quantum well photodetectors. *Semiconductor Science and Technology*, 19:442–445, 2004.

- [130] J.S. Orcutt, A. Khilo, C.W. Holzwarth, M.A. Popovic, H. Li, J. Sun, T. Bonifield, R. Hollingsworth, F. X. Kartner, H.I. Smith, V. Stojanovic, and R.J. Ram. Nanophotonic integration in state-of-the-art CMOS foundries. *Optics Express*, 19(2):2335–2346, 2011.
- [131] J. Hofrichter, A. La Porta, T. Morf, B.J. Offrein, P. Mechet, G. Morthier, T. De Vries, H.J.S. Dorren, and O. Raz. Inverting and non-inverting operation of InP microdisk modulators. *Electronics Letters*, 48(10):586–588, 2012.
- [132] M.R. Watts, D.C. Trotter, R.W. Young, and A.L. Lentine. Ultralow power silicon microdisk modulators and switches. *Proc. 5th IEEE Group IV Photonics, Sorrento, Italy, Sept. 2008*, pages 4–6, 2008.
- [133] Q. Xu, S. Manipatruni, B. Schmidt, J. Shakya, and M. Lipson. 12.5 Gbit/s carrier-injection-based silicon micro-ring microring silicon modulators. *Optics Express*, 15(2):430–436, 2007.
- [134] A.S. Liu, R. Jones, L. Liao, D. Samara-Rubino, D. Rubin, O. Cohen, R. Nicolaescu, and M. Paniccia. A high-speed silicon optical modulator based on metal-oxide semiconductor capacitor. *Nature*, 427:615–618, 2004.
- [135] J.E. Roth, O. Fidaner, R.K. Schaevitz, Y.-H. Kuo, T.I. Kamins, Jr. J.S. Harris, and D.A.B. Miller. Optical modulator on silicon employing germanium quantum wells. *Optics Express*, 15:5851–5859, 2007.
- [136] J. Liu, M. Beals, A. Pomerene, S. Bernadis, R. Sun, J. Cheng, L.C. Kimerling, and J. Michel. Waveguide-integrated ultralow-energy GeSi electro-absorption modulators. *Nature Photonics*, 2(7):433–437, 2008.
- [137] S.W. Corzine, M.R. Tan, S.-Y. Wang, and G. Ding. Modeling of turn-on delay time jitter in vertical-cavity surface-emitting lasers. *HPL Communications and Optics Research Laboratory*, 95(136), 1995.
- [138] M.N. Sysak, J.O. Anthes, J.E. Bowers, O. Raday, and R. Jones. Integration of hybrid lasers and electroabsorption modulators. *Optics Express*, 16(17):12478–12486, 2008.
- [139] IBM microelectronics specialty foundry
selection guide, downloadable from:.

- <http://public.dhe.ibm.com/common/ssi/ecm/en/tgb03009usen/TGB03009USEN.PDF>, accessed 12 August 2012.
- [140] O. Mitomi, S. Nojima, I. Kotaka, K. Wakita, K. Kawano, and M. Naganuma. Chirping Characteristic and Frequency Response of MQW Optical Intensity Modulator. *IEEE Journal of Lightwave Technology*, 10(1):71–77, 1992.
- [141] G. Agrawal. *Fiber-Optic Communication Systems*. John Wiley & Sons, New York, 1997.
- [142] P. Dong, S. Liao, D. Feng, H. Liang, D. Zheng, R. Shafiha, C.-C. Kung, Q. Qian, G. Li, X. Zheng, A.V. Krishnamoorthy, and M. Ashari. Low Vpp, ultralow-energy, compact, high-speed silicon electro-optic modulator. *Optics Express*, 17(25):22484–22490, 2009.
- [143] P. Dong, S. Liao, H. Liang, W. Qian, X. Wang, R. Shafiha, D. Feng, G. Li, X. Zheng, A.V. Krishnamoorthy, and M. Ashari. High-speed and compact silicon modulator based on a racetrack resonator with 1 V drive voltage. *Optics Letters*, 35(19):3246–3248, 2010.
- [144] T. Spuesens, Y. De Koninck, and D. Van Thourhout. Efficient vertical coupling between a silicon waveguide and an InP-based microdisk. *Proc. 16th European Conference on Integrated Optics, Barcelona, Spain*, Paper 212, 2012.
- [145] A.F. Oskooi, D. Roundy, M. Ibanescu, P. Bermel, J.D. Joannopoulos, and S. G. Johnson. MEEP A flexible free-software package for electromagnetic simulations by the FDTD method. *Computer Physics Communications*, 181:687–702, 2010.
- [146] J.D. Joannopoulos, S.G. Johnson, J.N. Winn, and R.D. Meade. *Photonic Crystals: Molding the Flow of Light (Second Edition)*. Princeton University Press, 2011.
- [147] A.D. Rakic, A.B. Djuricic, J.M. Elazar, and M.L. Majewski. Optical properties of metallic films for vertical-cavity optoelectronic devices. *Applied Optics*, 37(22):5271–5283, 1998.
- [148] A. Webster. Notes on metals in meep, downloadable from: http://falsecolour.com/aw/meep_metals/meep-metals.pdf, accessed 10 June 2012.

- [149] S.H. Kim, M. Yokoyama, N. Taoka, R. Iida, S. Lee, R. Nakane, Y. Urabe, N. Miyata, T. Yasuda, H. Yamada, N. Fukuhara, M. Hata, M. Takenaka, and S. Takagi. Self-aligned metal Source/Drain In_xGa_{1-x}As n-MOSFETs using Ni-InGaAs alloy. *Technical Digest IEEE International Electron Device Meeting, San Francisco (CA), USA*, P. 26.6.1-26.6.4, 2010.
- [150] Y. Kawamura, K. Nokana, and O. Nikami. Low threshold current GaInAs/AlInAs ridge MQW lasers with InP cladding layers. *Electronics Letters*, 24(10):637–638, 1998.
- [151] K. Mukai, Y. Nakata, K. Otsubo, M. Sugawara, N. Yokoyama, and H. Ishikawa. High characteristic temperature of near-1.3- μ m InGaAs/GaAs quantum-dot lasers at room temperature. *Applied Physics Letters*, 76(23):3349–3351, 2000.
- [152] Fujitsu Press Release. World's First 1.3 μ m Wavelength Quantum Dot Laser Capable of Operating in High-Temperature Environments that Exceed 200C. <http://www.fujitsu.com/global/news/pr/archives/month/2011/20110525-01.html>, accessed 08 November 2012.
- [153] S.G. Johnson and J.-D. Joannopoulos. Block-iterative frequency-domain methods for Maxwell's equations in a planewave basis. *Optics Express*, 8(3):173–190, 2001.
- [154] R. Waldhausl, B. Schnabel, P. Dannberg, E.-B. Kley, A. Brauer, and W. Karthe. Efficient Coupling into Polymer Waveguides by Gratings. *Applied Optics*, 36(36):9383–9390, 1997.
- [155] F. Van Laere, T. Claes, J. Schrauwen, S. Scheerlinck, W. Bogaerts, D. Taillaert, L. O'Faolain, D. Van Thourhout, and R. Baets. Compact Focusing Grating Couplers for Silicon-on-Insulator Integrated Circuits. *IEEE Photonics Technology Letters*, 19(23):1919–1921, 2007.
- [156] S. Assefa, S. Shank, W. Green, M. Khater, E. Kiewra, C. Reinholm, S. Kamalpurkar, A. Rylyakov, C. Schow, F. Horst, H. Pan, T. Topuria, P. Rice, D.M. Gill, J. Rosenberg, T. Barwicz, M. Yang, J. Proesel, J. Hofrichter, B. Offrein, X. Gu, W. Haensch, J. Ellis-Monaghan,

-
- and Y. Vlasov. A 90nm CMOS Integrated Nano-Photonics Technology for 25Gbps WDM Optical Communications Applications. *International Electron Devices Meeting (IEDM 2012)*, San Francisco, USA, Post-deadline paper 33.8, 2012.
- [157] J. Hofrichter, T. Morf, A. La Porta, O. Raz, H.J.S Dorren, and B.J. Offrein. A Single InP-on-SOI Microdisk for High-Speed Half-Duplex On-Chip Optical Links. *Optics Express*, 20(25):B365–B370, 2012.

List of Publications

Journal Papers

1. J. Hofrichter, T. Morf, A. La Porta, O. Raz, H.J.S. Dorren, and B.J. Offrein, A Single InP-on-SOI Microdisk for High-Speed Half-Duplex On-Chip Optical Links, *Optics Express*, Vol. 20, No. 25, pp. B365-B370, (2012).
2. J. Hofrichter, A. La Porta, T. Morf, B.J. Offrein, P. Mechet, G. Morthier, T. De Vries, H.J.S. Dorren, and O. Raz, Inverting and non-inverting operation of InP microdisk modulators, *Electronics Letters*, Vol. 48, No. 10, pp. 586-588, (2012).
3. J. Hofrichter, O. Raz, A. La Porta, T. Morf, P. Mechet, G. Morthier, T. De Vries, H.J.S. Dorren, and B.J. Offrein, A low-power high-speed InP microdisk modulator heterogeneously integrated on a SOI waveguide, *Optics Express*, Vol. 20, No. 9, pp. 9363-9370 (2012).
4. J. Hofrichter, O. Raz, L. Liu, G. Morthier, F. Horst, P. Regreny, T. De Vries, H.J.S. Dorren, and B.J. Offrein. All-optical wavelength conversion using mode switching in InP microdisc lasers, *Electronics Letters*, Vol. 47, No. 16, pp. 927-929, (2011).
5. J. Hofrichter, B.N. Szafranek, M. Otto, T.J. Echtermeyer, M. Baus, A. Majerus, V. Geringer, M. Ramsteiner, and H. Kurz, Synthesis of Graphene on Silicon Dioxide by a Solid Carbon Source, *Nano Letters*, 10(1), pp 36-42 (2010).

Conference Proceedings

1. S. Assefa, S. Shank, W. Green, M. Khater, E. Kiewra, C. Reinholm, S. Kamalapurkar, A. Rylyakov, C. Schow, F. Horst, H. Pan, T. Topuria, P. Rice, D.M. Gill, J. Rosenberg, T. Barwicz, M. Yang, J. Proesel, J. Hofrichter, B. Offrein, X. Gu, W. Haensch, J. Ellis-Monaghan, and Y. Vlasov. A 90nm CMOS Integrated Nano-Photonics Technology for 25Gbps WDM Optical Communications Applications, *International Electron Devices Meeting (IEDM 2012)*, San Francisco, USA, post-deadline paper 33.8, (2012).

2. J. Hofrichter, T. Morf, A. La Porta, O. Raz, H. Dorren, and B. Offrein. Compact InP-on-SOI Microdisks Used as High-Speed Modulators and Photo Detectors, *European Conference on Optical Communication (ECOC)*, Amsterdam, The Netherlands, P2.03, (2012).
3. J. Hofrichter, A. La Porta, T. Morf, B.J. Offrein, P. Mechet, G. Morthier, T. De Vries, H.J.S. Dorren, and O. Raz. Compact high-speed InP microdisk modulators heterogeneously integrated on a SOI waveguide. *Proceedings of the IEEE Optical Interconnects Conference*, 20-23 May 2012, Santa Fe, New Mexico, Paper MB6 (2012).
4. J. Hofrichter. InP Microdiscs as versatile devices for light generation, processing and detection, *European Conference on Optical Communication (ECOC)*, Geneva, Switzerland, (2011).
5. J. Hofrichter, O. Raz, L. Liu, G. Morthier, F. Horst, P. Regreny, T. De Vries, H. J. S. Dorren, and B. J. Offrein. Dual Wavelength Conversion Using Electrically Pumped Microdisc Lasers, *IEEE Group IV Photonics Conference*, London (UK), Talk ThB3, (2011).
6. J. Hofrichter, W. M. J. Green, F. Horst, S. Assefa, M. Yang, B. J. Offrein, and Y. A. Vlasov, Gating Couplers as Optical Probe Pads in a Standard CMOS Process. *IEEE Group IV Photonics Conference*, London (UK), Poster P1.24, (2011).
7. J. Hofrichter, F. Horst, B. J. Offrein, O. Raz, T. De Vries, H.J.S Dorren, P. Mechet, and G. Morthier. Microdisc Lasers Coupled to Silicon Waveguides as Versatile On-Chip Optical Components for Light Generation, Conversion and Detection, *Semiconductor Conference Dresden*, Dresden, Germany, (2011).
8. J. Hofrichter, O. Raz, F. Horst, N. Chrysos, C. Minkenberg, T. de Vries, H.J.S. Dorren, R. Kumar, L. Liu, and B.J. Offrein. A fast and comprehensive microdisc laser model applied to all-optical wavelength conversion, *Integrated Photonics Research, Silicon and Nano Photonics (IPR), Photonics in Switching (PS)*, United States, p.PTuA2 (2010).
9. J. Hofrichter, F. Horst, N. Chrysos, C. Minkenberg, R. Kumar, L. Liu, G. Morthier, T. de Vries, and B.J. Offrein. Digital all-optical signal

- processing using microdisc lasers, *Integrated Photonics Research, Silicon and Nano Photonics (IPR), Photonics in Switching (PS)*, United States, p.PTuA3 (2010).
10. G. Morthier, R. Kumar, F. Raineri, R. Raj, J. Hofrichter, N. Chrysos, B.J. Offrein, R. Zhang, J. van der Tol, O. Raz, and H. Dorren. Overview of the EU FP7-project HISTORIC, *Proceedings of SPIE - Silicon Photonics and Photonic Integrated Circuits II (invited)*, 7719, Belgium, paper 771908 (2010).
 11. N. Chrysos, C. Minkenberg, J. Hofrichter, F. Horst, and B.J. Offrein. in *Proc. 11th Int'l Conference on High Performance Switching and Routing (HPSR 2010)*, Richardson, TX, Jun. 14-16, (2010).
 12. J. Bolten, J. Hofrichter, N. Moll, S. Schoenenberger, F. Horst, B.J. Offrein, T. Wahlbrink, and H. Kurz. CMOS compatible cost-efficient fabrication of SOI grating couplers, *Microelectronic Engineering*, Vol. 86, No. 4-6, pp. 1114-1116, (2009).

Patents

1. "Optical Coupling Device", J. Hofrichter, N. Moll, *US Patent No.* 7929815 B1, 19 April 2011.
2. "Optical Coupling Method", J. Hofrichter, N. Moll, *US Patent App.* 2011/0188898 A1, 4 August 2011.
3. "Electromagnetic Wave Isolator And Integrated Optics Device", J. Hofrichter, N. Moll, *WO Patent* WO/2011/045693, 21 April 2011.
4. "Electromagnetic Wave Isolator And Integrated Optics Device", J. Hofrichter, N. Moll, *US Patent App.* 2012/0189246 A1, 26 July 2012.
5. "Integrated Device With Defined Heat Flow", T. Brunswiler, J. Hofrichter, *US Patent App.* 2012/0186793 A1, 26 July 2012.

Acknowledgements

The present work has been completed in collaboration between IBM - Research Zurich and TU Eindhoven University of Technology. Therefore, I owe many thanks to a numerous amount of colleagues.

I would like to take this opportunity to equivalently thank my PhD supervisor Prof. Dr. Harmen J. S. Dorren for the excellent mentoring throughout the entire thesis and my manager Dr. Bert Jan Offrein, who made it possible to carry out the work at IBM Research - Zurich. I thank him cordially for his continuous support throughout all the years. In particular I thank Dr. Oded Raz for his advice and support during the fabrication and measurements at TU Eindhoven and numerous fruitful discussions.

Also, I owe thanks to the remaining members of the TU Eindhoven spectrum cleanroom group: Tjibbe de Vries for his expert advice during the fabrication, Erik-Jan Geluk for the SEM images, Martine van Vlokhoven for the AFM images and Barry Smallbrugge for supporting the fabrication by countless mask cleaning sessions.

It is my pleasure to thank Dr. Thomas Morf and Dr. Antonio La Porta for numerous fruitful discussions and for proof-reading the thesis. The photonics group at IBM - Research Zurich, especially Dr. Folkert Horst, Dr. Thilo Stoeferle, Dr. Gabriele Raino, Stefan Abel and Dr. Paul Seidler are also acknowledged for the countless and insightful discussions during coffee. I would also like to thank Marcel Buerge and the model shop crew for providing me with the grating coupler measurement apparatus as well as Ute Drechsler for her indispensable lithography tricks. Hansruedi Steinauer is acknowledged for assembling the high-speed photoreceiver. Furthermore, I thank Dr. David Webb, Daniele Caimi and Rene Beyeler for their support during the fabrication. In addition, I thank Dr. Armin Knoll and Dr. Philip Paul and Felix Holzner for trouble-shooting whenever I encountered problems with the AFM. I thank Andreas Fuhrer for the FIB-cuts used during the pad characterization.

Particularly, I would like to thank Dr. Roland Germann and Steffen Reidt for their effort in bringing up the cleanroom at IBM Research - Zurich

and especially Steffen for his patience in training me on numerous tools. Moreover, I acknowledge Dr. Thomas Toifl for the support with measurement infrastructure from the Systems Department. I also thank Charlotte Bolliger for her effort in proof-reading my publications, Chris Sciacca and Marcel Begert for their various nice pictures and the media coverage of the work.

In addition, I would like to express my gratitude to Dr. Nikolaj Moll, who introduced me to scientific large-scale computing, to Stephan Paredes and Dr. Ingmar Meijer, who built and granted access to *AquasarLi*, and to Martin Bachmaier from IBM Boeblingen, who installed the Linux operating software on the machine and supported me during the installation of the scientific computation software.

I would also like to acknowledge Prof. Geert Morthier (Gent University / IMEC) for writing the excellent project proposal which resulted in funding of the *HISTORIC* project, which eventually enabled the work carried out in this thesis. I am also very grateful for the outstanding collaboration on bonding with Shahram Keyvaninia and Pauline Mechet (Gent University / IMEC). Pieter Dumon and Jin Guo (Gent University / IMEC) are acknowledged for the continuous support during design phase and DRC of the SOI waveguide structures fabricated at *Epixfab*. Liesbet Van Landshoot is acknowledged for providing the FIB-cuts used for analysing the samples fabricated in the initial fabrication runs. I also thank the committee members for their valuable comments and remarks that helped to improve the quality of this thesis further.

Beyond this, I am indebt to all the numerous people how have been proof-reading the thesis, in particular Martina Hitzbleck, Dr. Cyriel Minkenberg, Dr. Mirja Richter and especially my father for his correction night-shifts. I also cordially thank my parents for their mental and financial support throughout my studies.

Finally, I would like to thank my wife Adeline for her patience and kind assistance in mastering every day's life of a busy PhD student.

Curriculum Vitae

Jens Hofrichter was born in Dresden, Germany and obtained his University admission from the Martin-Andersen-Nexö Gymnasium in 2002. After completing the civil service, he studied electrical engineering at the Dresden University of Technology, Germany from 2003 to 2006. In 2006 he moved to RWTH Aachen, Germany, where he received the Dipl.-Ing. (equivalent to MSc) degree in Electrical Engineering under the supervision of Univ.-Prof. Dr. Heinrich Kurz in 2009. He has been with AMO GmbH Aachen from 2007 to 2009, working on low-noise JFETs and CMOS compatible synthesis methods of graphene.

After completing an internship in 2008 working on grating couplers, he re-joined IBM Research - Zurich in 2009, where he has been working towards his PhD in collaboration with the group of Prof. H.J.S. Doreen, COBRA Research Institute, Eindhoven University of Technology, the Netherlands.

His current research focus is on the simulation, fabrication and measurement of III-V devices heterogeneously integrated on silicon photonics, as well as on coupling schemes for silicon photonics. Jens Hofrichter is a member of IEEE Photonics Society and has authored more than 10 scientific publications in the fields of graphene research, silicon photonics, photonic integration and optical signal processing. Part of the work was highlighted as a feature article in the journal *Electronics Letters* in 2011. In the same year, he was awarded with IBM's First Plateau Invention Achievement Award, and in 2012 he received the IEEE Photonics Society Graduate Student Fellowship.

Awards

IEEE Photonics Society Graduate Student Fellowship 2012
First Plateau Invention Achievement Award (IBM) 2011